THE UNIVERSITY OF CHICAGO

SINGLE DEFECTS IN SEMICONDUCTORS FOR QUANTUM INFORMATION PROCESSING AND SENSING

A DISSERTATION SUBMITTED TO
THE FACULTY OF THE INSTITUTE FOR MOLECULAR ENGINEERING
IN CANDIDACY FOR THE DEGREE OF
DOCTOR OF PHILOSOPHY

BY
DAVID JAMES CHRISTLE

CHICAGO, ILLINOIS
AUGUST 2016

Copyright © 2016 by David James Christle

All Rights Reserved

for Megan

TABLE OF CONTENTS

LIST OF FIGURES

LIST OF TABLES

ACKNOWLEDGMENTS

I have been very fortunate in graduate school to be in the company of numerous high-caliber colleagues and to have continuous opportunities for both scientific and personal growth. Working in David Awschalom's group has been a privilege in this regard – he encourages us to pursue projects we are passionate about, even if they are risky, and cultivates a group atmosphere where students have a high degree of academic freedom and are surrounded by talented peers. I am thankful to have received his unparalleled support both at UC Santa Barbara and the University of Chicago, and to watch over the years as my friends in the group blossom into full-fledged scientists under his tutelage.

I want to thank my family and teachers for giving me the foundation needed to have made it this far. The support I had and extracurriculars I participated in continue to pay out dividends in ways I could not predict, and I see now how lucky I was to have these opportunities.

It was a great pleasure to have worked closely with David Toyli. We met as undergraduates in Paul Crowell's group at the University of Minnesota and I followed his path to the Awschalom group, first as an NNIN REU and then as a graduate student. He took me under his wing and made a strong effort to bring me up to speed and let me get my hands dirty in science fast. His tenacity, emphasis on a careful understanding of the physics, GTL, and eye for impactful science made an impression on me that lasted for years, even after our paths diverged. Bob B. Buckley elevated the lab in too many ways to count – he was a legend and a mentor to everyone around him, always kept a cool head, and worked incredibly hard to get things done. Things would not have been nearly as fun and successful as they were without being next door to Paul Klimov and Abram Falk in the Chicago lab. They both kept a fast pace in lab and I felt like we all learned from each other on multiple aspects of silicon carbide – our mutual appreciations for coffee and lifting were an added bonus. Chris Yale and I were a dynamic duo our first year, continuously solving homework problems in 3416, consuming Subway (The Feast, RIP) and Cactus Cooler, listening to Return of the

Mack, and computing the famous low-order CFG expansion series of Michael Caine. Will "BAF" Koehl was a large source of diverse conversation, from the hyperspectral vision of mantis shrimp to the finer points of Texas brisket. Will was crazy enough to hunt around in silicon carbide, which pushed the lab and especially myself into a new and fruitful research direction; I was glad to be the beneficiary of his constant encouragement of my research when I, too, felt a little crazy. Greg Calusine, who entrusted Will's conversations to me, provided great advice on life, perseverance, Master Fung's, lifting, and experiment over the years. Andrew Yeats, who stole Greg's danish, always amazed me with his resourcefulness and for pushing unique research directions – he has now ascended into the realm of Kevin Mitnick. The CNSI crew of Viva Horowitz, Jayna Jones, Brian Maertz, Mark Nowakowski, and Benji Alemán, for their friendships and being a part of my first lab home at UCSB. Alexander Yee, for doing all the hard work that let me jam out 210,000,000,000 decimal digits of π on a cold week in February to beat out the 1999 world record. Paolo Andrich was one of the nicest people I've encountered, and is well known to be the most enthusiastic European fan of American sport. Charles de las Casas shared my passion for optimization, but held me back when it was just too much. F. Joseph Heremans, who was my REU mentor, taught me lithography, smoothed out the focused ion beam bills I racked up (they said the budget was unlimited), and was awesome to travel with during the Great Cross-Continental Move of 2013. Jasper Vrugt, for sharing his Monte Carlo routines that pushed my self-teaching of statistical analysis to new heights. I thank Kenichi Ohno for watching closely and never losing his cheer. Greg Fuchs and Lee Bassett both liked doing things right and I felt like I took a class from each when I worked through rederiving their mathematical routines over the years.

I had excellent outside collaborators for the work in this thesis: Audrius Alkauskas, Chris van de Walle, Nguyen T. Son, Jawad ul Hassan, Erik Janzén, Takeshi Ohshima, Slava Dobrovitski, Krisztián Szász, Viktor Ivády, and Ádám Gali – thank you for taking a chance on me and all of your hard work. I would also like to acknowledge my committee mem-

bers Andrew Cleland and David Schuster for their feedback on my research and enjoyable chats over the years. I am also happy to have a new scientific perspective watching the group's newest members carry the torch: Chris Anderson, Peter Mintun, Brian Zhou, Kevin Miao, Gary Wolfowicz, Sam Whiteley, Erzsebet Vincent, Alex Bourassa, Berk Diler, Alex Crook, Paul Jerger, Masaya Fukumi, and Agnetta Cleland. I would also like to thank the many staff who have helped me in various ways throughout my time in graduate school: Holly Woo, Lynne Leinenger, Eva Deloa, Daniel Daniels, Bob Hanson, Dianna Morgan, Bismoy Dasgupta, Mary Pat McCullough, Emily Greusel, Brian Thibeault, Don Freeborn, Aidan Hopkins, Adam Abrahamsen, Tony Bosch, Brian Lingg, Peter Duda, Paul Weakliem, Shivakumar Bhaskaran, Jeff Dutter, Mark Sheckherd, Andy Segale, Mike Wrocklage, Luigi Mazzenga, and Mike Deal.

Finally, I want to thank my wife Megan for being a true partner in life and supporting me for all these years – I truly would not have been able to do all this without you. You are a treasure to be with and I cannot wait to see where we end up next!

ABSTRACT

This thesis describes studies on atomic point defects in semiconductors for applications in quantum information. In particular, its focus is on defects whose energy levels reside deep within the bandgap certain semiconductors because these systems can behave like artificial trapped atoms in the solid state, possessing optical addressability, long coherence times, and the ability to be manipulated at microwave frequencies. The most prominent defect in this field of study is the diamond nitrogen-vacancy center, whose functionality is well-known to persist to ambient temperature. The first part of this thesis investigates the persistence of this functionality to temperatures upwards of 600 K. Importantly, these investigations also demonstrate that the diamond nitrogen-vacancy center can be a sensitive thermometer ($\eta \approx 10\,\mathrm{mK/Hz^{-1/2}}$) over a wide range of temperatures with nanoscale spatial resolution.

The latter part of the thesis describes experimental measurements of divacancy defects in silicon carbide, a potential alternative materials host to diamond with established wafer-scale growth and microfabrication capabilities. Single divacancy spins are isolated and coherently controlled for the first time in the 4H polytype of silicon carbide, and the divacancy's coherence is shown to be a remarkably long 1.2 ms at $T = 20\,\mathrm{K}$. The last chapter extends these results by isolating single divacancies in the 3C polytype, experimentally demonstrating a qualitative and quantitative model of their spin and orbital dynamics, and revealing the divacancy's excited state level structure in both the 3C and 4H polytypes using resonant laser techniques. These excited state transitions are shown to posses a structure identical to the diamond nitrogen-vacancy center and a subset are shown to have favorable cycling properties. The location of a clear spin-photon interface has important implications for high-fidelity quantum state readout and photon-based entanglement schemes that use divacancy spins.

CHAPTER 1

INTRODUCTION

1.1 Some historical and theoretical underpinnings for the development of a computing machine based on quantum mechanics

Computing machines based on digital logic have underpinned many of the most significant human achievements of the 20th century. The Colossus computer, developed at Bletchley Park in the early 1940's, was the first programmable electronic digital computer. It used a vast collection of vacuum-tube-based elements that could perform logical operations and counting to perform cryptanalysis on the Lorenz cipher. The United States Army's "Electronic Numerical Integrator And Computer" was independently developed in 1946, and could solve problems of a much more general variety (thermonuclear simulations & artillery table calculations, included) and at vastly greater speeds. Among an innumerable set of examples, drastic miniaturization empowered the creation of the guidance computer of the Apollo missions, the creation of the Internet, shotgun sequencing of the human genome, and the ubiquitous availability of computing power individuals possess today. Richard Feynman hypothesized the vast benefits of miniaturization as early as 1959 in a lecture the annual meeting of the American Physical Society. There, he also suggested that if miniaturization were taken to its extreme, devices would ultimately encounter the vastly different physics at the atomic scale – and that there would be new kinds of devices be based on quantized states of matter, such as spin.

The 1980's saw several seminal works on the theory of what we now call quantum computation – that is, the creation of a model of computing whose fundamental elements are quantized states[20, 78, 54]. It was realized that quantum computers could not only perform the same types of computations as classical Turing complete machines, but that they are a

necessity for the practical simulation of quantum states. Specifically, computing the quantum mechanical probabilities of a system with N elements on a classical computer would require the computation and storage of order N^N probabilities. Even for modest N and the computational power available today, this problem is intractable because of the extreme scaling behavior of required computing resources. Put in more concrete terms, recent estimates[5] place the number of atoms in the universe at about 10^{80}, yet simulating a system of 50 qubits on a classical computer would require the computation and storage of approximately 10^{85} probabilities. Direct simulation of quantum mechanical systems would open up a vast array of possible applications, from studying the physics of superconductivity, to the development of new materials and new small-molecule/protein-based drugs.

Quantum superposition and quantum correlations – hallmarks of what makes quantum mechanics fundamentally different from classical mechanics – were also realized as a significant resource for "parallelizing" certain types of numerical computations. The first quantum algorithms envisioned solved only toy problems, but illustrate very clearly the power of quantum computing. The algorithm developed by Deutsch and Jozsa would decide if a function g, whose inputs are n-bit binary strings ($\{0,1\}^n$), has either a constant output across its entire domain, or has a "balanced" output – 0 on half its domain and 1 on the other half[55]. The algorithm developed by Simon solved another toy problem: an unknown function f maps an n-bit binary input string to a binary output string, and the only known condition of f is that there exists a binary string s such that $f(x) == f(y)$ if and only if x is equal to y or $x \oplus y == s$, where $\oplus$ is the exclusive-OR operation[216]. The problem to be solved is to determine the string s. In both problems, we are given access to an *oracle* that we provide the input to and we receive the output of the function f. In both cases, these problems can be solved efficiently on a quantum computer relative to the best classical algorithms. For the problem given by Deutsch and Jozsa, we need to test $2^{n-1}+1$ inputs – exactly one more test than half of the domain – to decide whether g is constant or balanced on a classical system. For Simon's problem, a classical computer requires *at least* $2^{n/2}$ queries for a prob-

abilistic algorithm to find the special input string s. In contrast, a quantum computer could solve the Deutsch-Jozsa problem with exactly one oracle query, and solve Simon's problem probabilistically with oracle queries bounded below by only n. The important conclusion these algorithms demonstrate is that quantum computers can achieve *exponential* speedups on certain problems versus their classical counterparts.

There are now several examples of quantum algorithms with practical relevance. Traditional symmetric ciphers, used for strong encryption of e-mails, banking transactions, and a plethora of other communications, require a key to be shared between the two parties that want to communicate securely. A major difficulty with these symmetric schemes is that because the two parties presumably do not have a secure channel over which they may communicate, they need to share the key or "password" over some existing channel that may potentially be insecure. Interception of the key during this sharing process would allow an eavesdropper to decrypt all future communications that use the symmetric encryption scheme, which clearly lessens its practical use. In contrast, the "public-key" cryptographic systems on which modern secure communications rely are based on the observation by Diffie and Hellman that secure key exchange over an insecure channel is possible given a mathematical operation that is easy to compute one way, but where the reverse computation is very difficult[59]. The RSA system developed by Rivest, Shamir, and Adleman[202] uses the integer factorization problem for this purpose: it is simple for a classical computer to compute the product $P \times Q = N$, where P and Q are prime numbers kept secret, yet going the other way – the factoring of N, which is shared over the insecure channel and can be readily seen by a potential eavesdropper – is only possible with a sub-exponential running time using the state-of-the-art classical algorithm called the General Number Field Sieve.

Peter Shor realized that a quantum analog of the Fourier transform could be used for solving the integer factorization problem in what is now known as Shor's algorithm[215]. This algorithm relies on two ingredients. The first is that the problem of finding a non-trivial factor of N can be transformed into finding the "period" of the equation $a^x \bmod N$, where a is

a randomly chosen integer, and the period r is defined such that $a^{x+r} \bmod N == a^x \bmod N$. If we can find r easily for an arbitrary a, the factors of N can be computed on a classical computer very quickly. The second is that we can implement a quantum version of this function, apply it to a superposition of many states, and use a quantum version of the Fourier transform to find the period r with high probability. This algorithm can factor arbitrary N using only polynomial time and space resources, and thus its impact on modern cryptographic systems would be substantial.

A second quantum algorithm with practical relevance that deserves mention is Grover's algorithm, which can (among other problems) be used to solve the problem of finding a specific entry in an unstructured list of size M[96]. The only requirement is a function that, in the example of the list, will flip the phase of only the state corresponding to the element we want to find. Given this function, repeated application of the algorithm will "rotate" the quantum state vector to the correct element with a favorable running time. On a classical computer, we would need to check all M entries to guarantee we found the specific entry we sought, but a quantum computer could find the entry with a number of operations that scales as only $\sqrt{M}$, which is a quadratic speedup over the classical algorithm.

Developing new algorithms or new ways to use quantum computers or devices is an active area of research. In particular, because quantum states are fragile, the development of quantum error correction algorithms that are practical within the constraints of experimentally realizable systems is enormously relevant towards a working and scalable quantum computer[80]. Quantum algorithms have also recently been proposed for training and running both supervised and unsupervised machine learning algorithms in high dimension with an exponential speedup over their classical counterparts[147, 195, 148]. Although Shor's algorithm may break widely used cryptographic systems, commercial systems that use quantum mechanical states for communication that is free of eavesdropping are already available[229]. It is clear now that machines that leverage quantum states will absolutely be useful if they can be realized, and only the extent of this usefulness is an outstanding question – the reach

of the impact of known applications and seeing what kinds of applications we have not yet even conceived that end up being useful make this an exciting time to be alive.

1.2 Experimental progress towards the creation of a quantum computer

Quantum algorithms are representations of operations that can be implemented in vastly different physical systems. The field of classical information theory, launched in large part by Shannon[213], abstracted away the notion of algorithms and information from the physical hardware those operations were implemented in, e.g. vacuum tubes, electromechanical relays, gears, or solid state transistors, into a more fundamental theory of what it means to process "information". In the same fashion, quantum algorithms are abstractions that can be run on different physical systems. The smallest building block for a quantum computer is known as a quantum bit, or 'qubit', and a famous work by DiVincenzo[60] in the year 2000 outlined the criteria that are desirable for a candidate experimental system to have in order to be useful for quantum computing and the transmission of quantum information:

1. The system must have a two-level subsystem that can function as a qubit.

2. There must exist a means to initialize the qubit into a known quantum mechanical state.

3. There needs to be a set of what are called "universal quantum gates" between qubits.

4. We must be able to measure the state of the qubit.

5. The qubit should have a long memory time (mostly referred to in this dissertation as a "coherence time").

6. The ability to convert between stationary and "flying" qubits, and the ability to transmit those flying qubits over long distances.

Early experimental efforts focused on liquid state nuclear magnetic resonance (NMR) as a possible platform for quantum information[51]. These systems are ensembles of nuclei that are initialized by placing them into a large magnetic field, which splits their magnetic energies by the nuclear Zeeman effect, and then allowing them to polarize thermally according to Boltzmann statistics. Typical polarizations for these systems are on the order of 1 in 10^5, which is quite low but is enough to detect. This statistical mixture can be manipulated using RF pulses that generate spin rotations. A key fault with a polarization so low is that true entanglement (i.e. a non-separable density matrix) cannot be obtained – the density matrices are nearly the identity matrix, and although the non-identity portion of the density matrix can be put into a Bell state, the density matrix is still separable and thus true entanglement is unachievable[186, 111, 19]. Although some progress has been made showing certain cases where speedup over classical computing can be achieved without entanglement[137], entanglement is a fundamental resource for quantum computers in the sense that it is required to execute arbitrary algorithms. Without easily achievable entanglement and better ways to scale up liquid NMR systems, they appear at this time to be less promising than other approaches for larger scale quantum computing.

Trapped ion systems have made immense strides in both the number of qubits that can be coupled together (up to 14), their unmatched coherence times ($T_2^* \approx 50\,\mathrm{s}$), and the achievement of gate and readout fidelities well above 99% [185, 173, 169, 28, 176, 174, 102]. These atoms have a complicated level structure with many states, but for quantum computing purposes, the "qubits" are generally chosen to be the so-called hyperfine "clock states" – named so because these states are, to first order, insensitive to changes in magnetic field, which in turn makes them have extremely stable transitions that are useful for atomic clocks. Although the hyperfine sublevels are not optically active, they can be mapped to a so-called "optical qubit" for high-fidelity readout, owing to the existence of an extremely good cycling transition. These characteristics make them among the furthest advanced systems for quantum computing, but controllably coupling ions together becomes more difficult as

the number of ions scales. The simpler schemes like relying on the mutual repulsive forces between ions to connect them via motion become too difficult because of the high number of collective modes that arise as N becomes more than a few qubits. The current thoughts for making progress in these systems revolve around either shuttling the ions into particular areas of a chip where they can be manipulated, or by using photon-based entanglement schemes. This is a common problem in multiple quantum computing candidate systems – scaling the number of qubits beyond a handful of qubits becomes very difficult to achieve in practice.

Individual photons also behave like quantum objects and can in principle be used for quantum computing[127]. At their core, single qubit operations can be achieved by wave-plates and the weak interactions between photons and mirrors or other photons mean their coherence times can be exceptionally long [130]. An interesting aspect of linear optics quantum computing is that the beamsplitter plays a central role in causing the photons to interact. As mentioned, photons do not interact with each other, so it seems that making two-qubit gates thus might be impossible, but two photons incident on a beamsplitter will exit the beamsplitter according to bosonic statistics: they both exit through the same path (left or right) and not through separate paths (one left, one right). This is a purely quantum mechanical effect. When counting coincidences on the two detectors, then, a 'dip' is observed, called the Hong-Ou-Mandel effect[109]. Combined with parity checks, this effect can be used to form two-qubit gates that are probabilistic, meaning they only work some fraction of the time[146, 188]. The number of beamsplitters and polarizers needed to obtain a desired success probability of the entire circuit must combat the p^N scaling of N probabilistic gates with success probability p. This scaling in resources needed to make a complex circuit that works with reasonably high probability quite cumbersome, and although the scheme using teleportation in [127] and later extensions get around this issue somewhat, the success of operations using teleportation needs n input bits entangled for an $n/(n+1)$ success probability. A decent number of qubits is required to approach the success probabilities needed

for error correction protocols to become useful, and these n-bit input states now take much longer to prepare than their single-bit constituents. Overall, physically scaling the optical elements and the finite success of gates remains a large barrier to achieving scalable quantum computing using linear optics.

Superconducting qubits (sometimes called a Josephson quantum computer) are at the moment the most promising implementation for a potentially larger scale quantum computer. These systems all rely on the physics of a Josephson junction[120, 7], which is fundamentally composed of a layer of insulating material (typically aluminum oxide) between two superconducting metals (typically aluminum) that is so thin that paired electrons (Cooper pairs) within the superconducting metals can tunnel across the junction. Capacitors and inductors are linear elements, so circuits formed from these elements have energy levels that are equally spaced. This makes it difficult to interact with a definite qubit state because an excitation at a particular frequency will excite the mode of interest but also a host of others. The Josephson junction, by contrast, is a very non-linear inductive element that also has very low dissipation. The nonlinearity means that the $|0\rangle$ and $|1\rangle$ lowest energy states of the harmonic-oscillator-like potential now have a different energy spacing than the $|1\rangle$ and $|2\rangle$ states, and so microwave pulses can be used to select this specific subspace to function as a qubit. While there are several specific superconducting qubit designs based on Josephson junctions[178, 175, 239, 246, 56, 128], the key benefits of these systems is that they are artificial atoms that can be fabricated using conventional cleanroom processing techniques developed over the last half decade for making conventional microprocessors. This means the qubit-to-resonator couplings, anharmonicity, type of qubit, and working frequencies are all tunable, everything is in the solid state, and the geometries are often planar. This also means that the creation of more qubits and resonators is, to zeroth order, as simple as patterning more elements in the lithographic masks used in the fabrication process in the same fashion as a microprocessor. The qubits' working frequencies are usually tuned to occur at microwave frequencies, which are a "sweet spot" between frequencies

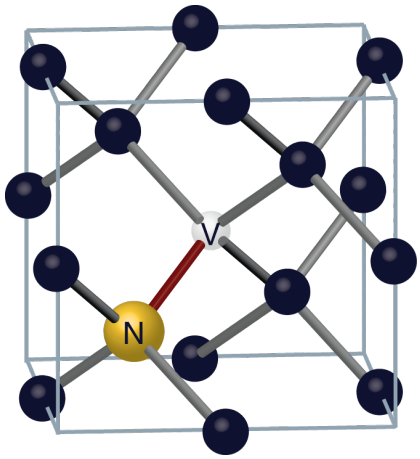

Figure 1.1: Ball and stick model of the nitrogen-vacancy center in diamond. A nitrogen atom (yellow) substitutes for a carbon atom in the lattice, while a vacancy (translucent) is an empty location where a carbon atom would normally be located. The dangling bonds from the carbon and nitrogen atoms, along with an additional electron from elsewhere in the lattice, create molecular orbitals located within the band gap of diamond.

that are low enough to be easy to work with (i.e. impedance matching is not a major problem) and warm enough to suppress unwanted thermal excitation at those frequencies ($h\nu/k_{\mathrm{B}}$ for $\nu = 6\,\mathrm{GHz}$ is about $250\,\mathrm{mK}$, and closed cycle dilution refrigerators can regularly obtain temperatures in the $10 - 50\,\mathrm{mK}$ range). These systems now have coherence times approaching 100 microseconds in a planar geometry[201] and many beautiful experimental demonstrations[164, 45, 212, 58, 8, 182, 206, 16], including error correction at the fault-tolerant limit [198, 15, 123, 50]. There are not any obvious large barriers to near-term progress in these systems (although their coherence times are still relatively inferior), but the tasks ahead are significant. Even with a surface-code-based quantum computer, the number of physical qubits required for realistic integer factorization is on the order of one hundred million, each with its own classical-based control electronics that have non-negligible overheads[81].

This dissertation is centered around using atom-sized point defects in solid state semiconductors for quantum information purposes. The most prominent defect in this area is the nitrogen-vacancy (NV) center in diamond, which is a vacancy and an adjacent substitutional nitrogen atom in the carbon lattice of diamond, illustrated in Fig. 1.1. NV centers are formed

by multielectron states within the deep bandgap of diamond (5.5 eV), and this property keeps them relatively isolated from their surrounding environment. Much attention has been focused on the NV center because it can be initialized and read-out using laser pulses (optical addressability) at room temperature with reasonably high fidelity ($\approx 82\%$)[203], manipulated using standard microwave pulse sequences, and it can use nuclear spins as a memory with room temperature coherence times exceeding 1.0 second[165]. The functionality at room temperature in relatively simple experimental setups is a feature that distinguishes these systems from other leading possible implementations of quantum information processing.

NV centers form in large numbers in nitrogen-rich diamond that has been irradiated with high energy particles and annealed to form NV centers, and although they have been studied in ensembles for various reasons since their discovery in 1965, vast interest in the system for quantum computing applications did not come about until single NV centers were first isolated in a confocal microscope in 1997[69, 97]. Since then, the field has achieved certain important milestones: photon antibunching[34, 24], Rabi oscillations[118], resonant manipulation[233, 18], high-sensitivity magnetic field sensing[234, 166], spin-photon entanglement[35, 235], entanglement of distant NV centers[23], teleportation[187], and loophole-free violation of Bell's inequality[104], among many others. A key barrier towards scaling these systems up to larger than a few qubits is that they do not interact unless placed within $\approx$10 nanometers of each other where the dipole interaction is strong, but this closeness prevents the easy individual addressability of the qubits because it is much smaller than the diffraction limit. A multi-qubit system might be realized by scaling up the photonic entanglement of distant centers work done by Bernien, *et al*[23], but this scheme suffers from a low entanglement probability due in part to the non-ideal spectral properties of NV centers and the engineering challenges of microfabricating diamond to mitigate these non-idealities. A second key point about point-defect qubits is that they are top down: the fundamental properties such as initialization fidelity, readout fidelity, and coherence times are set fundamentally by the electronic structure of the defect itself and the materials host in which it

resides. That means that, unlike superconducting qubits or even quantom dots, a defects properties are mostly given to us by nature and are relatively difficult to change after the fact. It behooves us, then, to seek out new defects in either diamond or a different materials host that is imbued with flexibilities beyond diamond.

Recently, ensembles of divacancy and divacancy-related defects in silicon carbide, a wide bandgap material with many existing commercial applications, demonstrated the ability to be initialized/read-out using light, manipulated using microwaves, and to have coherence times near $50\,\mu$s [247, 129, 72]. These are the first defects other than the NV center to demonstrate similar functionality, they occur in a commercially relevant material that is available at the wafer scale, and they emit in the telecom wavelength range, which has obvious benefit for photon-based entanglement schemes that utilize optical fibers. Easier growth and microfabrication might make these systems more commercially viable, allow them to be integrated conventional electronics more easily, and lastly allow better microfabrication of structures that can dramatically enhance the success probability of photon-based entanglement.

1.3 Thesis overview

The diamond NV center is the prototypical defect in the arena of optically addressable solid state defects for quantum information processing applications. It has been studied intensely for over 50 years and much of the recent rapid progress in studying the silicon carbide divacancy is owed to the vast historical literature of NV centers[149, 197]. Chapter 2 will begin with an overview of deep-level defects as quantum bits, the experimental progress of our understanding of the diamond NV center, and draw some parallels about how our understanding of the neutral divacancy in silicon carbide has progressed in the last few years. Chapter 2 will also discuss the basic layout and operation of experimental apparatus used to observe and manipulate these defects, with particular focus paid to the specifics of observing the divacancy since these details are newer and not widely disseminated.

The first original contributions of this thesis relate to studying the NV center's properties as a function of temperature in Chapter 3. The NV's room temperature functionality is quite unique among systems that display quantum phenomena potentially useful for quantum computing, and this chapter shows that this functionality persists to 600 K before becoming inoperable. This chapter develops a model that both explains the loss of functionality at high temperatures and yields an estimate of one of the unknown energy level spacings in the NV center's level structure. The NV center is a single qubit system where a major hurdle is to scale the up to multi-qubit experiments, but an alternate line of research seeks to apply single NV centers as nanoscale sensors. A major conclusion that Chapter 3 draws and that Chapter 4 builds upon with significantly enhanced detection protocols is that NV centers can function as "quantum-assisted" thermometers, and achieve both high spatial resolution (nanoscale) and high sensitivity to changes in temperature. Studying NV centers for use in thermometry is now a very active research area.

The latter half of the thesis studies divacancy defects in silicon carbide. The diamond nitrogen vacancy center is the prototypical deep-level defect qubit, but finding another defect with analogous functionality but in a different materials host has become a very recent topic of interest. This is in part because a defect's materials host has its own practical limitations as to how well it can be grown (e.g. large wafers, low impurities, low strain, low defects, etc.) and how practical it is to micromachine that substrate material into different optomechanical structures of interest (e.g. photonic crystals, nanobeams, and mechanical resonators). But from a more basic perspective, it is also interesting to look for defects that retain certain functionality like optical addressability but operate at a favorable wavelength like the telecom bands, have different spin coherence behavior, or maybe have somewhat non-analogous functionality that ends up being better for certain applications. Silicon carbide is a materials host with outstanding properties so it is a prime target for this line of research. In the Chapter 2 review of the silicon carbide defect literature that has developed prior to and alongside the work in this thesis, it will become apparent that like the diamond NV,

early experiments were performed on large ensembles of divacancy defects. These earlier experiments showed the divacancy as a promising defect spin qubit, and Chapter 5 focuses on the key step of isolating and controlling *single* divacancy defects, which is a first for the exploration of deep-level defect spins in materials outside of diamond. It will be shown that divacancies are remarkably coherent (better than the best non-isotopically purified diamond), can be isolated in both the 4H and 3C polytypes of silicon carbide (Chapters 5 and 6), have larger ground state spin polarizations than the NV center ($(96 \pm 4)\,\%$) (Chapter 6), and that their excited state structures contain the same cycling transitions and implied selection rules that are used in the diamond NV center for high fidelity initialization, single-shot readout[204], and photon-based entanglement protocols[17, 23], among other things (Chapter 6).

CHAPTER 2

INTRODUCTORY PHYSICS OF SOLID STATE DEFECTS FOR QUANTUM INFORMATION APPLICATIONS

2.1 Defects as quantum bits

2.1.1 Energy level formation within a semiconductor bandgap

Most of the interest in semiconductors stems from their somewhat unique energy level structure and our ability to easily manipulate its chemical potential. The periodic arrangement of atoms in the lattice yields electronic states that in some energy regions, form continuums of levels that are very closely spaced, but in other regions have no levels at all. These energy level continuums are called *bands* and the ranges of energy where no electronic states are allowed to exist are called *bandgaps*. Electrons, being fermions, cannot occupy the same electronic state at the same time, so the electrons in a solid will fill these levels up to a certain energy (at $T = 0$) called the *Fermi energy*. Roughly speaking, the location of this energy within a band or a band gap will determine the conductive behavior of the material. For a metal, the Fermi energy lies within a band, meaning that the electrons near the Fermi level can be promoted to states with slightly higher energy – under an applied field, this freedom allows the electrons to move through the material with ease and in great number, so the conductivity is very high. In a semiconductor without dopants, the Fermi level is located in the middle of the band gap, which means at zero temperature the band below the gap (called the valence band) is completely occupied and the band above the gap (called the conduction band) is not occupied at all. At finite temperature, some probability exists to transition from the valence band to the conduction band using thermal energy. Because the bandgaps of commonly used semiconductors are in the range of one to a few electron volts, this gives a very low *intrinsic* concentration of electrons (holes) in the respective bands – typically in the range of 10^9 electrons or holes per cubic centimeter.

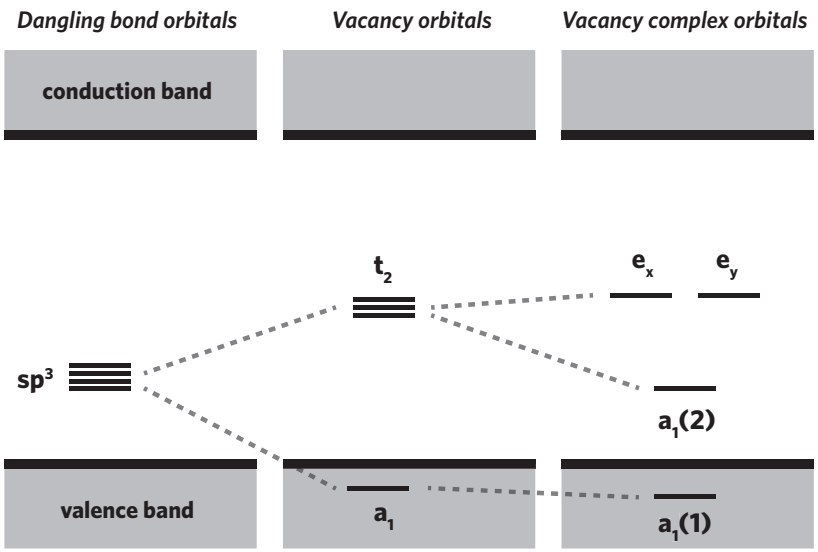

Figure 2.1: Energy level representation of a deep level defect's energy levels in a tetrahedrally coordinated semiconductor. The creation of a vacancy causes the energy levels to shift into t_2 and a_1 symmetry states. The energy levels shift further when put into a complex – for instance, with a nitrogen – to form two e symmetry orbitals and an additional a character orbital. Figure adapted from [247].

Defects within an otherwise perfect crystal will distort the local energy level structure and certain states can form *within* the band gap. Depending on the energetic distance from the band gap edges, these states can be classified as either shallow ($\approx< 100\,\text{meV}$) or deep. Shallow defects create electronic states that behave like free electrons (or holes) but with an altered effective mass, and like the free electron states, these states are delocalized, i.e. their wavefunctions are not concentrated near the defect. Because of their small energy level separation, these states can add electrons (holes) to the conduction (valence) bands, and a dopant is characterized as an *acceptor* or *donor* based on whether it tends to subtract or add electrons to the conduction band. This subtraction or addition greatly modifies the conductivity behavior of the semiconductor because dopants can be added in amounts that vary over many orders of magnitude in a controllable fashion. Areas of a semiconductor that have been "doped" in different ways to give differing electron/hole concentration can be combined to form novel devices like diodes and transistors that underpin much of modern technology.

Deep level defects, of which this thesis is chiefly concerned, possess wavefunctions that are highly localized and do not in general modify a semiconductor's conductivity by an appreciable amount because they are usually low in concentration. Classification as a deep defect means typically that their energy levels be several hundred meV away from the band edges. The relevant energy scale at finite temperature, given by $k_B T$, is only about 25 meV at room temperature, so transitions between the band edges and these states are exponentially suppressed by the ratio of the states' energy difference and this thermal energy scale. Put another way, electrons that occupy levels deep within a bandgap behave somewhat like electrons bound to atoms. The manipulation of trapped atom electronic states, mentioned previously in Chapter 1, has led to some of the most successful demonstrations in the area of quantum information, so the prospect of having trapped-atom-like states in a solid-state host material without the challenges associated with the laser cooling, collective mode crosstalk, and shuttling ions amongst an increasing number of Paul traps is appealing from both simplicity and scalability standpoints.

The formation behavior of the single electron orbital levels of a vacancy and vacancy complex are shown in Fig. 2.1 [247]. The dangling bonds leftover from when an atom is removed and left vacant will split because of the reduced symmetry of the lattice. The levels will split further when the vacancy forms into a vacancy complex with some other nearby impurity or vacancy. With the aim of using defects for quantum computing purposes, an important point is that a vacancy alone will tend to form a spin singlet (where the total spin is zero) instead of a spin triplet (where the total spin is 1), but the formation of a vacancy complex can allow the formation of a spin triplet. Both the nitrogen vacancy center in diamond and the divacancy in the various polytypes of silicon carbide have the orbital level structure of a vacancy complex shown in Fig. 2.1. Diamond and silicon carbide are both considered wide bandgap semiconductors, with the bandgap of diamond being about 5.5 eV and the bandgaps of the most common polytypes of silicon carbide ranging from $2.4-3.2$ eV [155]. This compares to lower bandgap semiconductors like silicon or germanium,

which have bandgaps of 1.1 eV and 0.7 eV, respectively. A wide bandgap host is particularly important for maintaining isolation from the conduction and valence bands – it increases the likelihood of hosting defects that have more than one of their single electron states within the bandgap, and the likelihood of those states being far enough away from the band edges that thermal excitation is suppressed. The NV center and divacancy have the additional property that the splitting between their $a_1(2)$ and e states are also relatively large – 1.945 eV and 1.1 eV respectively – which is necessary for excitation of the electronic states using visible and near-infrared light, again respectively. Optically active defects are sometimes given the name "color centers" for this reason. For quantum computing purposes, the visible and near-infrared wavelengths are experimentally advantageous to work with because of the advent of low loss optical fibers and detector technologies that can achieve high quantum efficiencies at these wavelengths. Because these defects are paramagnetic, their spin states can be manipulated using microwave radiation of only a few GHz in frequency, and as we will soon see, the peculiarities of their orbital and spin dynamics allow their spin states to be polarized and read out by exciting their visible or near-infrared optical transitions and recording the intensity of the red-shifted photoluminescence they subsequently emit.

2.1.2 The negatively charged diamond nitrogen-vacancy center

Historical development

The nitrogen-vacancy (NV) center was first observed by du Preez in Type Ib diamonds that had been irradiated and annealed as a band of visible photoluminescence associated with the photoluminescence of vacancy defects[69]. The more definitive assignment that this defect was the NV center was made after polarization and unaxial stress studies of the defect's zero phonon line (1.945 eV, 637 nm) supported only trigonal or monoclinic symmetry, that its orientation had to be along $\langle 111 \rangle$, that its optical transition has an A-E symmetry characteristic, and that its optical spectra agreed more closely with the

substitutional nitrogen model rather than the model of a nearby interstitial nitrogen[48, 52]. It was established by the electron paramagnetic resonance (EPR) measurements of Loubser and van Wyk that somewhere in the NV's orbital structure is a spin triplet that can be optically polarized[149], and for many years it was believed that the this triplet was a long-lived excited state because the EPR signal was not observed in their experiments without optical illumination. This idea, now known to be incorrect, held for some time. The persistent spectral hole burning measurements of Harley, *et al.* were the first evidence that suggested that the triplet was a metastable state was incorrect. Their measurements showed that side holes well within the inhomogeneous linewidth of the zero phonon line could be burned into the optical spectrum, and that these holes could persist for more than 15 minutes[100]. This is difficult to reconcile with both the ground and excited states being previously assigned as singlets, and the fast 13 ns optical decay observed by Collins, Thomas, and Jorge[49] – transitions between triplet and singlet states can occur, but are typically either only weakly radiative or have very long lifetimes as in phosphorescence. Later, the persistent hole burning measurements of Bloch, *et al.* were taken while microwaves were swept across the 2.88 GHz splitting of the triplet[29]. These measurements showed that the depths of the holes burned were directly modulated by this microwave radiation when it was resonant with the triplet states even as they were shifted with the application of a magnetic field. The first direct evidence for assigning that the $^3A_2$ state was the ground state and the ^3E state was the excited state was made by Reddy, *et al.*'s two laser experiments, shown in Fig. 2.2. There, the antiholes and holes could be explained as transitions between the ground state and lower orbital branch of the excited state in the presence of strain. Although the inferred spin-orbit coupling, λ, and g values were not correct, the overall level structure given was the correct one. Additional measurements using optically detected magnetic resonance and the Raman heterodyne effect all supported the conclusion that $^3A_2$ was the ground state[241, 107, 159, 160], and eventually the very unambiguous observation of electron paramagnetic resonance in the dark was made[197]. All

together, these measurements definitively resolved the confusion over the level ordering by proving that the optically polarizable spin triplet is in fact the NV's $^3A_2$ ground state.

The works of Lenef & Rand[139, 141], Goss, *et al*[92], and Martin[163] were the initial detailed theoretical investigations into the NV's excited state structure. Together they established based on comparison with experiment that the correct model of the NV center is the $n = 6$ electron model, where the center is negatively charged (consistent with the experimental results of Mita[172]) and has an excited state triplet is a ^3E state[140]. This particular state is an orbital doublet, and splits into two different branches as transverse strain is applied to the defect. While the measurements of Reddy and Manson[196] were taken at the center of the inhomogeneously broadened ensemble zero phonon line, Manson and Wei[157] showed that the hole pattern changed based on the particular wavelength of the burn laser. Shifting the burn laser about 150 GHz in frequency lower than the center of the ZPL produced one set of holes, while setting it 600 GHz higher produced another set of holes. Martin interpreted the spectral hole burning data as probing different excited state level branches of NV centers that possessed very large strain. In the high strain limit, the splittings of energy levels within each branch are essentially independent of strain. This observation will become relevant again in the investigations into the excited states of divacancy defects in silicon carbide performed in Chapter 6 of this thesis. Martin also correctly inferred that both the spin-orbit and spin-spin couplings were only a few GHz in magnitude, contrary to previous measurements[196]. The precise excited state level structure was finally revealed in two papers by Tamarat, *et al* and Batalov, *et al* that probed single NV centers with a narrow line laser swept over their zero phonon lines. This technique, when combined with microwaves, can reveal the entire structure directly with resolution better than 200 MHz. These works showed that the level structure is generally in agreement with the model of Martin, quantitatively determined the spin-orbit and spin-spin parameters that govern the excited state Hamiltonian, and demonstrated the existence of a long-lived cycling transition. This detailed understanding of the excited state was necessary for later schemes

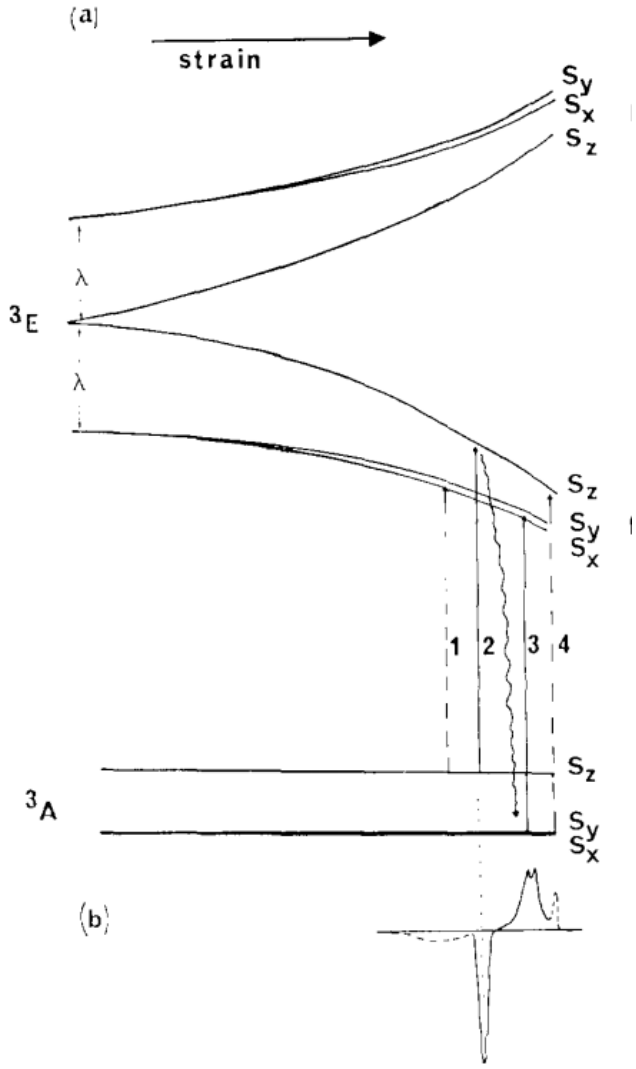

Figure 2.2: **a.** Theoretical diagram of a ^3E excited state spin triplet, orbital doublet, and a $^3A_2$ spin triplet orbital singlet level configuration. **b.** The resulting holes and antiholes seen in a two laser hole burning measurement at cryogenic temperatures. Figure from Ref. [196].

that utilized resonant lasers for initialization and readout of the ground state spin[18, 204], as well as photon-based entanglement of distant NV centers[23]. For a more detailed review of nitrogen-vacancy centers, see the recent comprehensive review by Doherty, *et al.*[63].

Basic initialization and readout

The negatively charged nitrogen vacancy center (NV center) is understood to be composed of six electrons whose total electronic ground state is a spin triplet. Fig. 2.3 shows the single and total electronic states that comprise the NV center. The $a_1(2)$ state is located within the valence band, while the $a_1(2)$ and e_x and e_y states are located within the gap. The filling of electrons shown in Fig. 2.3 is governed by Hund's rules[87]. The $^3A_2$ ground state ("the ground state") is further split based on spin sublevel by the crystal field into an $m_s = 0$ level and two degenerate $m_s = \pm 1$ levels situated 2.87 GHz above the $m_s = 0$ level[101, 149]. This is the main state involved in using both the NV center as a qubit and for nanoscale sensing. It has long coherence times of about $\approx 600\,\mu$s in chemically purified diamond and 1.8 ms in isotoptically purified diamond[227, 12]. Because the excited state has spin-dependent decay pathways, it enables both readout and initialization of the ground state spin. Specifically, the ^3E excited state ("the excited state") couples its $m_s = \pm 1$ spin sublevels much more strongly to the singlet states, and off-resonant laser light preserves the spin when exciting the NV center from the ground state to this excited state[161, 203, 85]. Relaxation to the ground state directly occurs with the emission of a photon, but relaxation through intersystem crossing to the singlets and a final intersystem crossing back to the ground state is typically dark. *This means that the total photoluminescence emitted from the NV center is spin-dependent.* Direct optical decay to the ground state tends to preserve the spin sublevel, but decay through the singlets has an increased probability of flipping the spin from $m_s = \pm 1$ to $m_s = 0$, so the existence of this spin-dependent decay path from the excited state also means that repeated optical pumping of the NV center will preferentially polarize the spin into the $m_s = 0$ spin sublevel in the ground state. This process tends

to saturate and produce a total spin polarization $P = p_{m_s=0}/(p_{m_s=0} + p_{m_s=\pm1}) \approx 82\,\%$ [161, 203, 236].

Experimentally, this readout process can be revealed by the used of time-correlated photon counting techniques[68]. Fig. 2.4 shows the time-resolved photoluminescence intensity from a single NV center prepared in the $m_s = 0$ and $m_s = \pm1$ spin states. The key features to observe are that the $m_s = 0$ state emits more overall photoluminescence than the $m_s = \pm1$ states and that regardless of how the spin is prepared, the photoluminescence equilibrates after a timescale of roughly 600 ns. The standard approach for off-resonant readout of the NV center (and the divacancy in silicon carbide) is to count the number of photons received in a fixed period of time, e.g. ≈ 200 ns. The optimal duration depends on the laser intensity used and is calibrated by maximizing the measurement contrast (i.e. the relative difference in intensity between maxima and minima in a Rabi oscillation) or signal-to-noise. The NV center's maximum off-resonant readout contrast is about 30% and has an initialization polarization of 82%, and this means that room temperature experiments achieve what today would be considered quite low initialization and readout fidelities. In practical terms, however, these two performance metrics are sufficient for magnetic sensitivities better than $500\,\mathrm{nT/Hz^{1/2}}$ [166] and, as we will see in subsequent chapters of this thesis, thermal sensitivities of about $15\,\mathrm{mK/Hz^{1/2}}$. A basic rate equation with five levels, shown with the appropriate transition lifetimes in Fig. 2.5, captures most of the room temperature spin dynamics and photoluminescence intensity of the NV center[161, 236]. Both the ground and excited state triplets can be treated as two levels, $m_s = 0$ and $m_s = \pm1$, and since the decay between the singlets is relatively fast[4], they can be treated as a single level with a singlet decay constant[161, 203]. In Chapter 3, we augment this model to capture the temperature dependence of the photoluminescence intensity and contrast of the NV center we observed at temperatures upwards of 600 K, and in Chapter 6 we will present the experimental data necessary to establish a similar model for divacancies in silicon carbide.

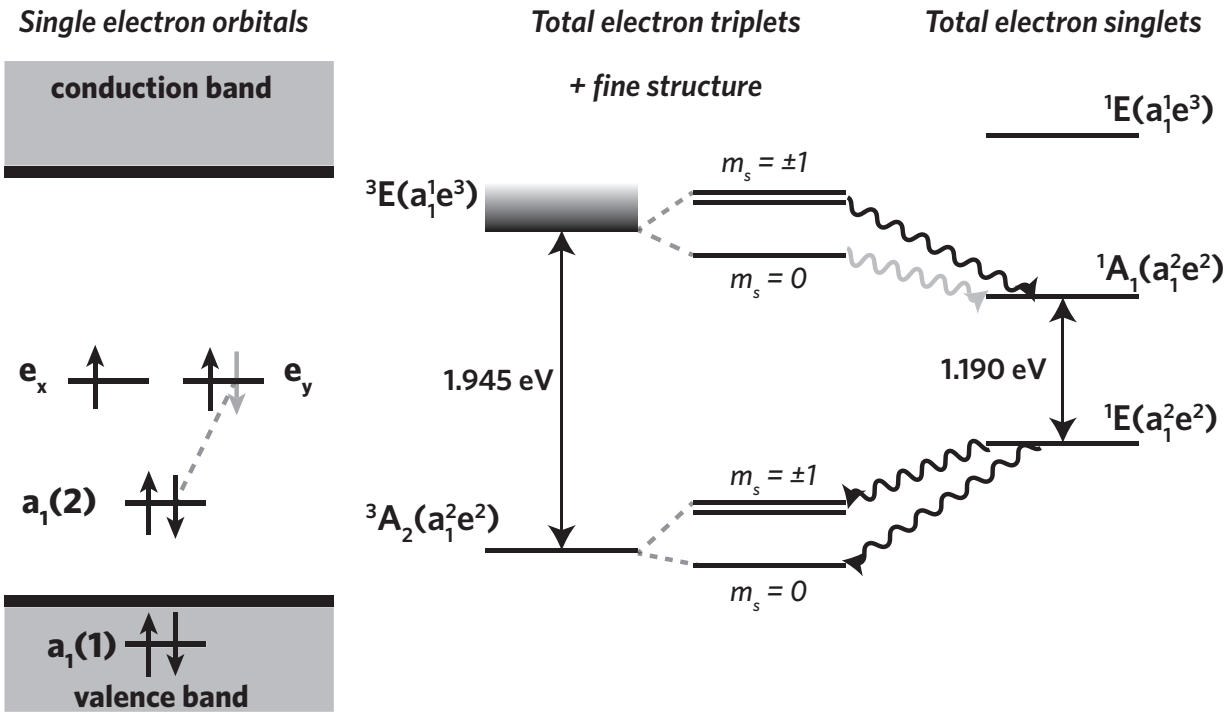

Figure 2.3: Energy level diagram of the negatively charged diamond nitrogen vacancy center. The left shows the single electron orbitals that are composed of linear combinations of the dangling bond states. The black arrows over each state represent the filling of the states with electrons of either spin up or spin down. The dashed line and faint arrow indicates that optical excitation can promote an electron to either the e_x or e_y orbital (both abbreviated as e for the total electron labels). The middle shows the total electron ground state triplet and first excited state, and each triplet's fine structure is also shown. The right shows the total electronic singlet states. The labels of the triplet and singlet states are derived from the character table of the C_{3V} character table, where the superscript denotes the total spin as a triplet or a singlet, and the letter/subscript is from the Mulliken symbol for the irreducible group representation that corresponds to the state. The label terms in parentheses indicate the single electron configurations that comprise the state. The vertical arrows indicate the zero phonon line triplet-to-triplet and singlet-to-singlet optical transitions (637 nm and 1042 nm, respectively), while the gradient above the $^3A_2$ state indicates that absorption can occur for off-resonant, higher energy applied optical excitations. The wavy lines indicate non-radiative intersystem crossing transitions, where the $m_s = 0$ spin sublevel intersystem crossing from the excited state is fainter because this transition is known to be weak. Figure is adapted from [87, 167, 62, 236].

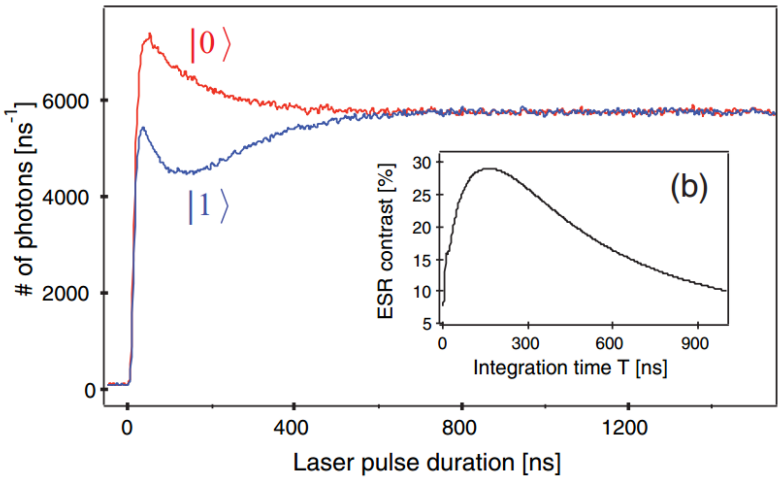

Figure 2.4: Time-correlated readout of the ground state spin of the diamond NV center. The two traces show the photoluminescence intensity when the spin is off-resonantly prepared in the $m_s = 0$ and $m_s = \pm 1$ states. Inset: The readout contrast, defined as the relative integrated intensity difference between the two states, as a function of integration time. Figure from [68].

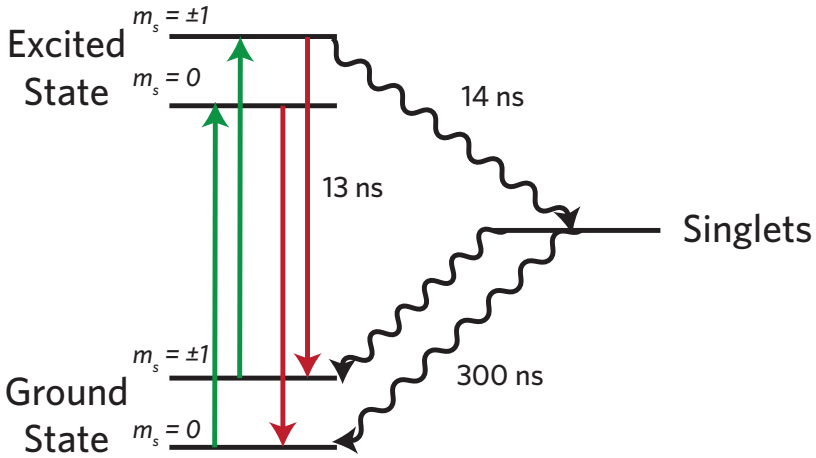

Figure 2.5: Energy level diagram for a five level model of the diamond NV center. The ground and excited triplets are consolidated into two levels each, while the two singlets active in the spin readout and polarization process are consolidated as a single level. The transition lifetimes are approximate and taken from [161, 203, 236].

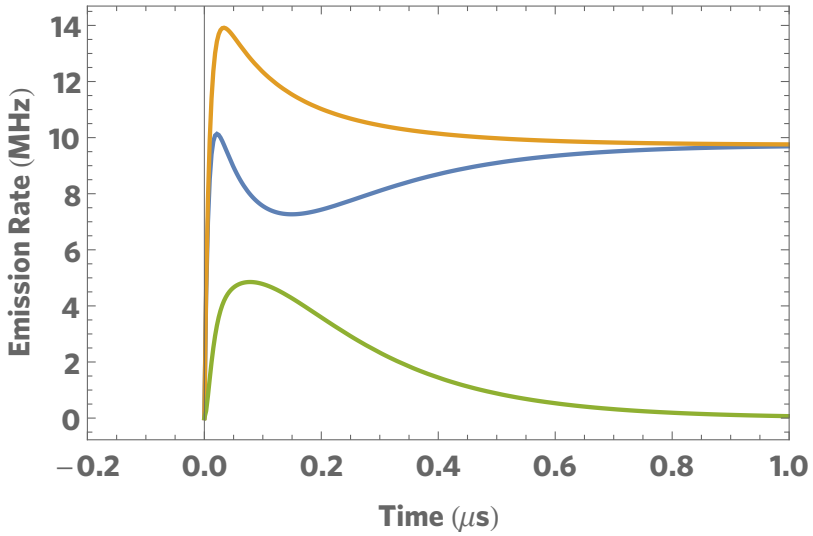

Figure 2.6: Photoluminescence emitted from the NV center predicted from the numerical solution of the five level rate equation model. The orange curve shows the photoluminescence emitted when the spin is prepared in the $m_s = 0$ state and the blue curve shows the corresponding emission when a π-pulse is applied to the ground state spin splitting to prepare the spin into one of the $m_s = \pm 1$ sublevels. The green curve is the difference between these two emission rates and is effectively the main ingredient in the readout contrast. These plots reproduce the experimental data of Fig. 2.4.

Fine structure of the ground and excited states

The ground state spin is the workhorse of the NV center. It is an orbital singlet, spin triplet, and the spin sublevels can be a highly coherent qubit state: as mentioned, depending on the chemical and isotopic purity of the diamond host, the the ground state spin coherence times achievable are in the range of $T_2 = 650 - 2100\,\mu$s[227, 114]. Assuming any magnetic field is predominantly along the NV center's axis, the ground state level structure can be described by the Hamiltonian,

$$H_{\mathrm{NV}} = DS_z^2 + E\left(S_y^2 - S_x^2\right) + g\mu_{\mathrm{B}} B_z S_z + \sum_i \vec{S}\overleftrightarrow{A}_i\vec{I}_i, \tag{2.1}$$

where $D = 2.87\,$GHz is the axial crystal field splitting, $E \approx 100\,$kHz is the transverse crystal field splitting, S_z, S_y, and S_x are the Cartesian components of the spin-1 electronic spin operator (and $\vec{S}$ is a vector of these components), g is the dimensionless magnetic moment

(g-factor), μ_{B} is the Bohr magneton, B_z is the applied magnetic field along the NV's axis, $\overline{A}$ is the particular electron-nuclear hyperfine interaction tensor, and $\vec{I}$ is the vector of nuclear spin operator components. Microwave radiation is used to drive transitions between the eigenstates of this Hamiltonian often within the scope of the rotating wave approximation of a two-level system. The derivation of this approximation is available in standard textbooks on quantum mechanics. Often, a small magnetic field will be applied to the NV center to break the $m_s = \pm 1$ degeneracy and a two-level subspace of the system is used as a qubit. This means that a single frequency of applied microwaves will drive a transition between the two levels, e.g. the $m_s = 0$ and $m_s = -1$ states, while leaving the other level unperturbed. Aside from electronic spin, each NV center possesses a ^{14}N atom as a constituent, with a coupling strength (defined in an $\overline{A}$ term) on the order of a few MHz. Nuclei possess some of the longest coherence times of any quantum system but are generally difficult to interact with directly. The NV center's hyperfine coupling allows the nitrogen nuclear spin to serve as a quantum memory element with ($T_{2,\mathrm{nuc}} = 1.3\,\mathrm{ms}$)[84]. Other experiments have used both strong and weakly couplied ^{13}C nuclei for even longer-lived memories with associated time constants near one second[165, 44, 70].

Excitation with off-resonant light is the main technique for initialization and readout of the spin at room temperature, but as mentioned previously, the signal-to-noise of this approach is very limited. At temperatures of about $T = 8\,\mathrm{K}$, the linewidths of the excited state's fine structure become narrow and a definite structure characteristic of the NV center excited state's ^{3}E symmetry can be revealed. Fig. 2.7 displays the fine structure derived from considerations of group theory and the nature of the quantum mechanical interactions allowed by it[167, 62]. Group theory allows the reduction of the most general spin Hamiltonian into one with relatively few parameters. In the present case, the structure at zero magnetic/electric field can be described by a single axial spin-orbit coupling, λ_z, and three spin-spin couplings D_{es}, Δ_1, and Δ_2. The effect of axial strain $\delta_{||}$ is to shift the levels in energy all equally, but a transverse strain, which has a slight in-plane direction dependence

but is typically simplified as a single term, $\delta_\perp$, will shift the levels in a more complicated way. As $\delta_\perp$ increases, the states split into two distinct orbital branches, and different anticrossings between states will occur at positions governed by the other parameters in the Hamiltonian. This general picture has been understood for some time (c.f. Fig. 2.2)) however only the most recent considerations clarified the precise role of spin-orbit and spin-spin interactions in the final "mixing term" Δ_2. The effect of the first three parameters is to shift or split various levels from one another, but the Δ_2 term is different in that it causes explicit mixing between the E_x/E_y and E_1/E_2 states, which have different spin. A weak Δ_2 term is desirable since it plays a role in minimizing the amount of spin mixing in the excited state. In certain regions of strain that are away from anticrossings, then, the E_x and E_y transitions are composed of $m_s = 0$ spin to a degree well above 99%, and the implication of this is that E_x and E_y are good cycling transitions[18, 233]. These cycling transitions (i.e. transitions that have very small branching ratios into states of different spin) are nowadays the basis for many cutting edge experiments in the NV center[235, 35, 204, 23, 187, 104, 253]. In contrast to off-resonant excitation, these experiments take place using a narrow-line laser that can be tuned to resonance with individual transitions from the fine structure in the ground state to the fine structure in the excited state. The connection between emission/absorption of a photon is much more strongly connected with the spin state in such experiments. While an off-resonant laser pulse will initialize the spin to about 82% polarization, the spin can be polarized to nearly 100% by subsequently applying a resonant laser to a transition of ± 1 spin in both the ground and excited states. Because the NV center's ISC is mostly spin selective to a ± 1 spin, the effect after repeated excitation is that either the spin will flip to $m_s = 0$ because of relaxation through the singlet states, or it will flip because of the small but finite branching ratio into $m_s = 0$. In the same vein, a second laser tuned to the $m_s = 0$ transition will strongly project the spin, and repeated excitation will either emit many photons, distributed geometrically, if the state is projected into $m_s = 0$ or ideally no photons if it is projected into $m_s = \pm 1$. Unlike off-resonant excitation, which gives an approximate readout

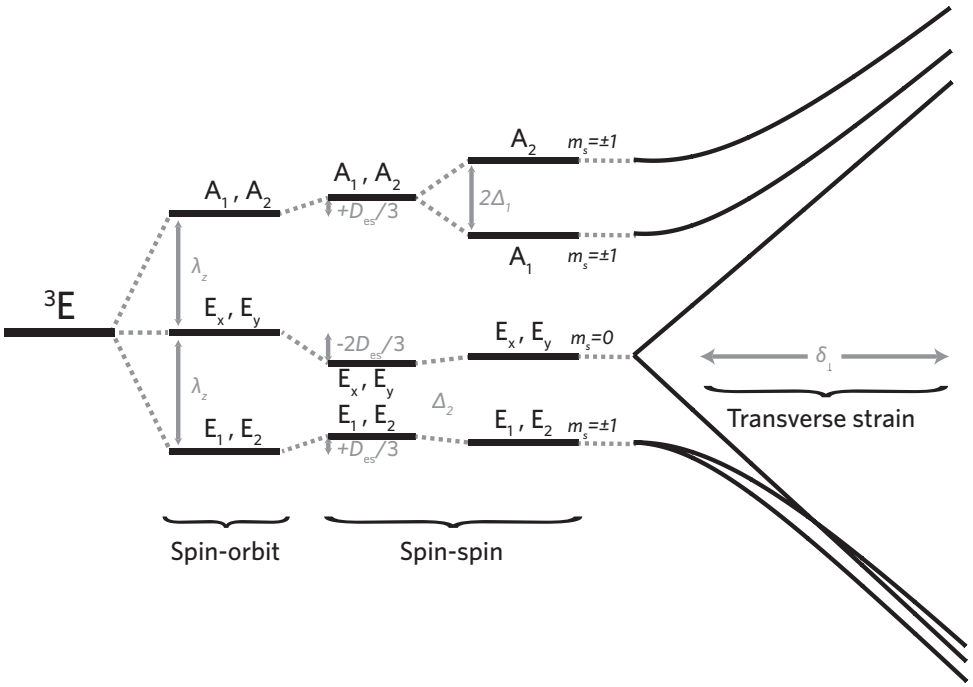

Figure 2.7: An energy level diagram of the NV center's ^{3}E fine structure. The dominant interactions at zero magnetic/electric field are the spin-orbit and spin-spin interactions. We parameterize here the axial spin orbit as λ_z, and the three spin-spin couplings, which split or mix particular states in different manners, as $D_{\rm es}$, Δ_1, and Δ_2. Axial strain (not shown) will shift each of the levels up or down equally, but the effect of transverse strain ($\delta_\perp$) mixes the levels in a more complicated way.

contrast of 30%, the resonant technique will give contrasts easily above 95%. If collection efficiency is improved sufficiently, this contrast can be observed within a single repetition of the readout sequence (a *single shot*) with fidelities in the range of 80-90% or more[204]. Single shot readout is a key requirement of many quantum information protocols like error correction, teleportation, the direct observation of Bell measurement correlations, and even the basic readout of a future quantum computer[21, 143, 104, 60].

This last point consists of two ingredients I will dwell on here because of their importance in Chapter 6. The excitation of the NV and emission of a photon can be interpreted as a single Bernoulli trial that has a very low probability of undergoing a spin flip. Once a spin flip occurs, no further photons are extracted from the transition. The total number of photons emitted before a spin flip occurs can be interpreted as the number of Bernoulli trial failures until a success (a spin flip) occurs, which means that the number of photons emitted will follow a geometric distribution whose probability proportional to the spin flip rate. Next, we know that each photon emitted will have a finite detection probability, and this means that the total number of photons actually *detected*, conditional on n photons emitted (n failures before a success), follows a binomial distribution. This distribution is difficult to derive analytically (in a continuous/low-detection-probability approximation, it ends up being geometric again), but the essential point is that both the spin flip rate must be low (giving a geometric distribution with a large expectation value) and the detection probability must be large enough to give at least a few photons actually detected per shot. For realistic spin flip rates and optical emission lifetimes ($\approx 200\,\text{kHz}$ and $13\,\text{ns}$), this gives an overall detection probability on the order of a percent or so[204]. While the detection efficiency is something that can be improved experimentally, such as through solid immersion lenses, photonic crystals, or higher quantum efficiency single photon detectors, the spin flip rate is related to more intrinsic properties such as spin mixing in the excited state and any less understood physics that would cause the unintended flipping of a spin. Intrinsic properties in a new defect, such as the divacancy or vacancy in silicon carbide, that are

unfavorable enough to preclude this entire route of high fidelity spin initilization/readout & spin-photon entanglement would be a serious blow for its future applications. Thus, these are important quantities to determine relatively quickly to discern how competitive a particular defect qubit is with the state of the art.

2.1.3 The neutral divacancy in silicon carbide

Motivations

The neutral divacancy in silicon carbide has attracted recent interest because it shows promise as an optically active qubit system, similar to the diamond NV, that resides in a favorable materials host, silicon carbide. Silicon carbide exists in over 200 polytypes, which are different atomic arrangements within the lattice of the silicon and carbon atoms, but the most common for electronic and now defect applications are the 4H, 6H, and 3C polytypes. As a material, silicon carbide is mature in both its growth and processing capabilities, and has an established commercial industry in the areas of high-frequency, high-power MOSFETs, diodes, etc. Much of what has been learned of this material for defect applications has been reported only in the last few years while the work in this thesis was being performed. Given this, I will try to summarize the development of the divacancy from the perspective of what properties are known and compare them to the prototypical diamond NV center, which has experienced approximately five decades of research.

From a high-level perspective, the diamond NV center is quite unique in the literature and it is only in the last few years that other defects in any material, like the silicon vacancy in diamond or the divacancy/vacancy in silicon carbide, received attention as a potential alternative system[247, 129, 180, 14]. Silicon carbide is attractive for defect applications because it has excellent micromechanical properties, can be grown at the multi-inch wafer scale (c.f. diamond growth at roughly the few millimeter scale), can be doped both p or n type, and has an established literature of high quality microfabricated structures that could

be used to couple to a spin's mechanical and photonic degrees of freedom[208, 254]. One of the largest drawbacks of the diamond NV center as well as the silicon carbide divacancy and vacancy are that only a few percent of their luminescence is contained in their zero phonon lines. Coupling NV centers to photonic crystals has been an ongoing area of research, and silicon carbide's ease of microfabrication already shows promise for making meaningful contributions to this line of research[76, 77, 138, 226, 144, 38, 190, 151, 36, 191, 152]. Along the same line of thinking, the divacancy's emission is near 1.1 μm in wavelength, which is in a region (near telecom band) favorable for transmission over an optical fiber. Because defects generally have very weak dipolar interactions, photon-based schemes are one of the most promising routes towards entangling distant defects, and the rates of successfully heralded entanglement are very sensitive to photon losses[17, 23]. The attenuation at the NV's ZPL of 637 nm is about 8 dB/km, while at the divacancy's ZPL of about 1100 nm in our SMF-28e+ fiber the attenuation is only about 0.67 dB/km[122]. The limitations of visible wavelength attenuation in fibers have already been felt in recent NV teleportation experiments over a 1.3 km link[104]. Long distance links in a future quantum network will require even longer lengths of optical fiber, so emission in the near infrared appears germane for this future technology.

The ability to dope the substrate has more speculative future applications since diamond doping is more difficult and therefore fewer relevant reports exist in the literature[121, 170]. Deep level defects lie within the bandgap of a semiconductor material, and doping strongly modifies the charge concentration. One interesting prospect is to observe the effect of changes in a defect's behavior in a structure that can electrically modify the local Fermi energy. This may have applications in enhancing nuclear memory coherences, re-programmable arrays of spins, stabilizing a defect's charge state, or in some sort of charge-based initialization/readout scheme. An early project I worked on that failed and thus did not make it into this thesis was to do investigate this charge modulation in such a structure, and Fig. 2.8 shows a scanning electron micrograph of a field effect transistor device I fabricated for these efforts.

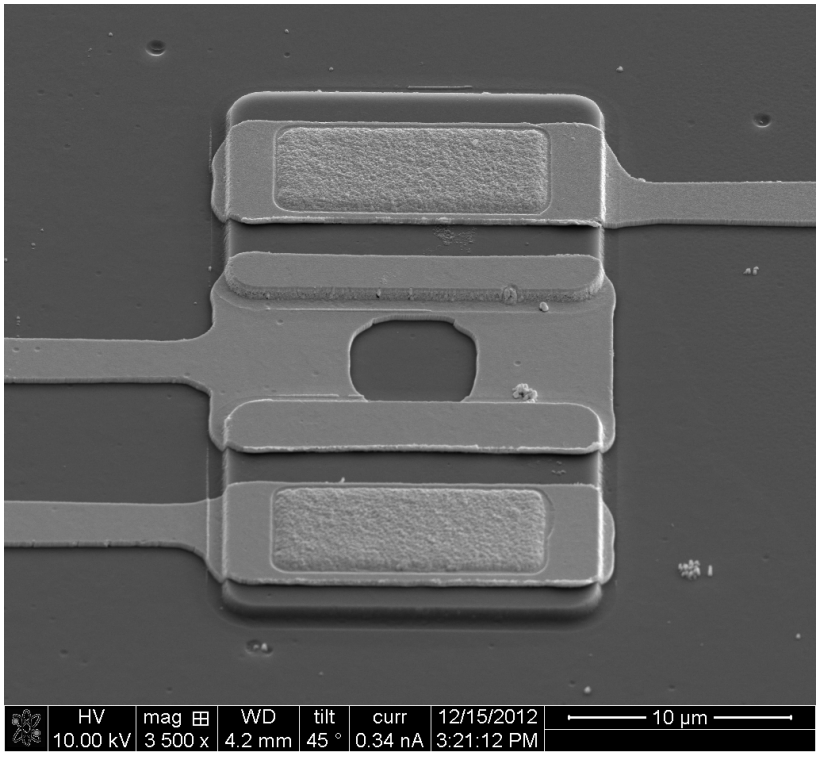

Figure 2.8: Scanning electron micrograph of a lateral *p*-*n*-*p* field effect structure in 4H-SiC. The structure is fabricated by aluminum implantation and high-temperature annealing (1400° C) of an *n*-type silicon carbide substrate, which at high enough doses will cause a thin layer at the surface to become *p*-type. The structure is etched using an SF_6/Ar inductively coupled plasma to form two *p*-type mesas. A layer of SiO2 is deposited using low temperature PECVD and lithographically patterned with a wet etch in hydrofluoric acid. A subsequent mask step is aligned to pattern holes for contacts on the mesas. Nickel is deposited with electron beam evaporation, lifted off, and annealed in a rapid thermal annealer to improve the contact's electrical behavior. A final mask patterns a gate that bridges the *p*-*n*-*p* region. A square-shaped window allows optical measurement of divacancy spins. If the doping concentration is low enough in the gate region, a voltage applied across the gate & back contact (not shown) will deplete/accumulate electrons at the SiO_2/SiC interface and change the local Fermi energy. The key problems with this structure are that the implantation and annealing (1400 ° C) are too damaging to the substrate, and that ion implantation is too crude of a technique to compensate the *n*-type substrate to be near insulating: the thickness of an active layer in a device like this will be less than 1 nm, meaning the probability of finding a defect that has its Fermi level modulated is vanishingly small. I later acquired a custom grown *p*-*i*-*n* epilayer structure from Norstel for this project. The structure has a doping profile precisely controlled during growth with no annealing required, and has a thick *i*-layer that serves as a large enough for probing single defects or ensembles of defects. Ultimately after our lab move to Chicago, I chose instead to look for single defects (Chapter 5) and put this project on indefinite hold. Given that single defects have now been isolated, the type of data that can be collected for this experiment may be much more interesting (e.g. time-domain studies).

The Stuttgart group has already made some unpublished progress studying single silicon vacancies in a *p-i-n* structure and it will be interesting what directions these avenues of research take in the near future.

Defect physics

Because of the different polytypes and different forms of similar but distinct divacancies in those polytypes, I will give only a general overview of divacancies focused mainly on 4H-SiC. I would also like to explicitly point out that for brevity I am omitting discussion of much of the new results in the last few years on assorted other defects in silicon carbide that have been reported somewhat in parallel with results in the divacancy[14, 200, 220, 41, 132, 248].

Originally, divacancies were observed as lines in the infrared photoluminescence spectra of various silicon carbide crystals and correlated to electron paramagnetic resonance and optically detected magnetic resonance experiments that showed they were associated with a spin-1 defect that can be optically polarized to a ground state like the NV center[238, 221–223, 39, 9, 13, 224, 225, 40, 31]. The spin resonance signals revealed coupling to nearby ^{29}Si atoms, and using density functional theory to compare the experimental hyperfine tensors to the observed splittings, and with the added evidence provided by annealing experiments, the defects in question were confirmed to be divacancies in the 4H and 6H polytypes[224, 225].

One important work towards identifying the characteristics of potential analogues to the NV center in other materials is that of Weber, *et al.*[247]. This work was a collaborative effort with our group, and proposed that a good defect for quantum information applications should have:

- A bound state suitable for use as a qubit, meaning it is long-lived, and it has some sort of energy splitting between the levels.
- An optical pumping cycle that polarizes the qubit state. In the NV center, this is a transition from the ground to excited state, and a spin-selective and non-radiative

decay pathway back to $m_s = 0$, as explained earlier in this chapter.

- Luminescence to or from the qubit state that varies by qubit sublevel in some differentiable way, whether by intensity, wavelength, or other property. In both the NV and the divacancy, this criterion is satisfied by the intensity change in photoluminescence that depends on the projection of the ground state spin.

- Optical transitions that do not introduce interference from the electronic states of the host.

- Bound states that are separated from each other by energies large enough to avoid thermal excitation between them.

An additional set of additional criteria were proposed for ensuring that the defect has long coherence:

- A wide band gap, so it can accommodate deep level defects.

- Small spin-orbit coupling, to avoid unwanted spin flips in the defect bound states.

- Availability as high-quality, bulk, or thin-film single crystals, in order to avoid imperfections or paramagnetic impurities that could affect the deep center's spin state.

- Constituent elements with naturally occurring isotopes of zero nuclear spin, so that spin bath effects may be eliminated from the host via isotopic engineering.

That work centered on comparisons between diamond and 4H-SiC and proposed that the nitrogen-vacancy center in 4H-SiC may have these favorable properties just as the nitrogen-vacancy center in diamond retains.

The experimental work from our group reported by Koehl, *et al.* deserves particular mention because its ensemble time-domain studies demonstrated a luminescence-dependent readout of coherent control experiments on each of the four divacancy forms in 4H-SiC and two still-unknown defects, labeled PL5 and PL6, whose functionality persists to room

temperature[129]. These measurements were taken in commercial high-purity-semi-insulating 4H-SiC sold as a standard product by Cree, and demonstrated T_2 coherence times of $39 - 263\,\mu$s, depending on the defect species and experimental conditions. The important contribution was that these defects display similar behavior to diamond NV centers but exist in a more flexible materials host. Certain physical differences such as optically detected magnetic resonance that increased rather than decreased emission in some defect species were also apparent. The earlier theoretical computations by Gali, *et al.* deserve mention for indicating that 4H-SiC divacancy should have a similar electronic structure as the diamond NV[86]. In particular, this work suggested their symmetries are both C_{3v}, they are both spin-1 ground states (demonstrated previously in bulk electronic paramagnetic resonance), the spin density is located near the core of the defect (may be inferred from careful comparison to hyperfine data), and that the optical transition should have a ${}^3A_2 \rightarrow {}^3E$ character (not demonstrated, but now demonstrated in Chapter 6). Important differences were also highlighted: the lowest single particle states may lie in the valence band for the divacancy (still unknown), the symmetry of the divacancy may be slightly distorted to C_{1h} (unclear), the diamond NV has a clear signal at room temperature but this had not been demonstrated in the divacancy (Koehl, *et al.* and Falk, *et al.* showed various divacancies have functionality that persists up to $\approx 200 - 250\,\mathrm{K}$), and that the spin flip process is unknown but bulk electronic paramagnetic resonance experiments (Baranov, *et al.*) and the later results of Koehl, *et al.* imply that somehow the laser can optically polarize the spin (how the process works is revealed in Chapter 6).

More recently, similar measurements reported by Falk, *et al.* in the 6H and 3C polytypes of silicon carbide showed T_2 times of about $70\,\mu$s in the six divacancy-like defects in the 6H polytype, and about $24\,\mu$s for the one divacancy-like resonance in the 3C polytype[72]. The zero field splittings of the spin-1 ground state are all near the $1.3\,\mathrm{GHz}$ splittings observed in the 4H polytype along with similar infrared emission. Later work identified the specific forms of divacancy in 4H and 6H through the use of density functional theory techniques,

and additionally showed that certain divacancy/divacancy-like defects are capable of polarizing nearby nuclei with very high (99%) efficiencies, which is appealing for nuclear memory applications[73, 74].

The collection of defects in silicon carbide that are divacancy or thought to be divacancy-related is now quite large. Seventeen of these photoluminescence resonances have been observed and coherently controlled in ensembles, which is a large increase from just the nitrogen-vacancy center in diamond that is the prototype of the field. But much of the physics is still relatively unknown compared to the diamond nitrogen-vacancy center, especially the physics of the excited state. Importantly, the isolation of single defects was an unachieved remaining milestone for divacancies. Among some other contributions, Chapter 5 and Chapter 6 are chiefly centered around isolating single divacancy spins in silicon carbide for the first time, showing that they have remarkable electronic spin coherence times of $T_2 = (1.2 \pm 0.1)\,\mathrm{ms}$, and directly revealing their excited state fine structures.

2.2 Experimental techniques for controlling single spins

The measurements in this thesis primarily come from several home-built confocal microscopy apparatus that are combined with electronics for the generation/amplification and sequencing of microwave pulses. Laser illumination of defects and the recording of their red-shifted photoluminescence intensity is the overarching purpose of the microscopy apparatus, and the microwaves serve the role of implementing quantum gates to defects within the liquid helium flow cryostat. Fast (ns to $\approx 100\,\mu$s scales) timing electronics sequence different laser sources, microwave bursts, gate the photon counting electronics, and trigger other modules like the time-correlated photon counting card. All of the slower timescale equipment control and timing waveform sequencing was done in LabVIEW for Chapters 3 and 4, but was done all in Python for Chapters 5 and 6. Because the operation wavelengths are different between NV centers (532 nm off-resonant excitation, 637 nm-800 nm emission) and divacancies (975 nm off-resonant excitation, 1037 nm-1350 nm emission, depending on species), the spe-

cific laser sources, optical filters/coatings, modulators, and photon detectors are different. But the essential techniques of confocal microscopy, microwave spin rotations, cryogenics, and photon counting are very similar. The experiments on diamond NV centers in Chapter 3 and 4 occur in air without the use of a cryostat, and a lithographically patterned resistive wire is used for temperature control between about 290 K and 700 K, whereas the divacancy experiments of Chapters 5 and 6 occur in a flow cryostat at temperatures between 8 K and 20 K. The ensemble Hahn echo measurements of Chapters 5 and 6 were taken in a different but similarly constructed confocal microscopy apparatus, the details of which can be found in the PhD thesis of Paul V. Klimov[124]. I will describe the experimental techniques in turn primarily from the aspect of isolating single divacancies since some of these specific details are new within the field.

2.2.1 Cryogenics and sample wiring

The silicon carbide samples are mounted on cold finger within a liquid helium flow cryostat (Janis, ST-500). This cryostat operates by placing a vacuum-jacketed transfer line into a dewar of liquid helium that is allowed to pressurize to a few psi. The dewar pressure is stabilized by either a 10 psi relief valve attached to each dewar by the vendor, or for more repeatable control, an adjustable brass relief valve attached to one of the dewar's exhaust ports. Liquid helium flows through the transfer line into a series of tubes that wind from a copper mass attached directly to the cold finger outward to a radiation shield. This design allows the cold finger to reach the 4.2 K boiling point of liquid helium or below if pumping is used, and mitigates liquid helium's poor latent heat by using helium gas's enthalpy to cool a radiation shield to a few tens of Kelvin before allowing it to escape to atmosphere. Two hermetically sealed SMA connectors are on the exterior of the cryostat, and stainless steel/copper core semirigid microwave coaxial cable is wound around the inside and sunk with Stycast epoxy at descending temperature points in order to minimize conduction of heat to the coldfinger. A custom goniometer with permanent magnets allows the application of

a magnetic field along adjustable polar and azimuthal angles with precise radial positioning using a motorized linear stage (Newport, IMS-100).

The coldfinger is a machined OFHC copper piece with grooves for two semirigid coaxial cable lines and a small trench for a coplanar waveguide used for launching the microwaves to the sample. After machining, the coldfinger is plated with gold to reduce its emissivity. The core of the semirigid coax is soldered to the center pin of this coplanar waveguide. The coplanar waveguide is designed to be $50\,\Omega$ and is fabricated on a Rogers Duroid substrate. The semirigid coax is permanently embedded in the coldfinger using Stycast epoxy, and the CPW is affixed to the coldfinger with solder. The end of the coldfinger is slightly raised by a few hundred microns depending on the predicted sample substrate size and if any additional CPWs are used. An additional CPW that is shorted at its endpoint can be placed on this part of the coldfinger to serve as a microwave antenna. This is used for a fabrication-free method of applying microwaves to the sample, which sits atop the CPW, but has the drawback of generating microwaves relatively far away from the defects in the sample being studied. Specifically, the defects are usually near the surface while the microwave antenna is on the backside of the sample. This distance of a few hundred microns to 1 mm means that the intensity of microwaves felt by the defect in this geometry can be fairly weak and thus obtaining spin rotations faster than a few hundred nanoseconds will generate significant heating and thus motion of the sample. The configuration most often used is to lithographically pattern Ti/Au antennae directly on the sample surface. This is done through electron beam lithography, electron beam deposition, and liftoff. Instead of wirebonding the CPW in the trench to the CPW on the raised surface of the coldfinger, the CPW in the trench is wirebonded directly to one of these on-chip antennae. This means that the microwaves are generated a few microns to a few tens of microns away from the defects being studied, and thus the necessary power incident on the cryostat is significantly lower. The samples are affixed to the coldfinger using Elmer's No-Wrinkle Rubber Cement because it can be cleanly removed, will stay intact through several cooldown cycles, and

causes relatively low background fluorescence. A resistive heater in the cryostat and a PID controller (Lakeshore 332) maintains the cryostat at $T = 8 - 20\,\mathrm{K}$ with a stability of better than $0.01\,\mathrm{K}$ after running a lambda-tuning based PID calibration routine.

The shroud around the coldfinger is custom designed to allow for optical access to the sample. The design constraints are set by the requirements that the neodymium permanent magnet used for Zeeman splitting of the electronic spin resonances needs to physically fit behind the shroud, which means both it and the coldfinger need to be sufficiently long. The microscope objective used is coverslip corrected, which means that abberations induced by a glass window are compensated by an adjustable optical element inside the objective. This coverslip correction goes up to $0.7\,\mathrm{mm}$, which sets an upper limit on the thickness of the window. The sample space of the cryostat is held under vacuum, so for a thin enough window, a deflection can occur that will induce a transmitted wavefront distortion to any light passing through the window. Effectively, the "power" of the window is increased so that it begins to act like an unwanted lens in the optical path. To mitigate this, I computed from deflection theory that a window diameter of $0.75\,\mathrm{in}$ (instead of our usual $1\,\mathrm{in}$) is sufficient to minimize the transmitted wavefront distortion below $\lambda/4$ and have more than a factor of four safety margin against rupture from the vacuum. Windows with thicknesses below $1\,\mathrm{mm}$ and flatnesses of even $\lambda/2$ are not generally commercially stocked. The window used on the cryostat is an infrared fused silica window custom fabricated by Rocky Mountain Instruments to about $0.65\,\mathrm{mm}$ thickness, $1\,\mathrm{in}$ diameter, and a flatness of $\approx \lambda/4$. Additionally, both sides are broadband antireflective coated to minimize reflection between about $1050\,\mathrm{nm}$-$1400\,\mathrm{nm}$, which is done to get an extra few percent of signal from the defects. This is less important in ensemble studies since the luminescence intensities from them there are much larger than a single defect. The shroud is CNC machined as a single piece with a precise window mounting depth that is the same as the window thickness. A groove to allow more epoxy around the edges is additionally machined in this thin metal support, and a gap of diameter $0.75\,\mathrm{in}$ is left for optical access. The window is affixed to the cryostat using Hysol 1C low-outgassing

epoxy and is allowed to cure at ambient temperature to minimize any stress that might occur in an elevated temperature cure and affect the wavefront distortion of the window. A polished face of the shroud mates the shroud to the rest of the cryostat with a standard Buna-N O-ring and Corning vacuum grease, and the placement of the shroud can be slightly adjusted by translating the shroud and fastening screws down in a slightly different location. This last point is important because it is important that the window is aligned flat to the incident laser/objective within about 20 arcseconds to obtain the best image quality and collection efficiency.

2.2.2 Optical microscopy of defects

Our experimental setup is a home-built, near-infrared confocal microscope, and a simplified diagram of it is presented in Fig. 2.9. A 330 mW 975 nm continuous wave diode laser (ThorLabs, PL980P330J) used for exciting the divacancy defects is coupled through a single mode fiber into free space using an aspheric lens. The beam is attenuated and focused using a neutral density filter wheel and focused through a lens into an acousto-optic modulator to obtain a rise time of about $10 - 20$ ns. The diffracted beam is focused into a Corning SMF-28e+ single mode fiber attached to three paddles that allow us to adjust the polarization using the birefringence of the fiber under strain (ThorLabs, FPC561). The combination of the acousto-optic modulator and re-focusing the beam into a single mode fiber provides a DC on/off contrast of about 47 dB. The beam is spectrally filtered using a 975 nm bandpass filter (Edmund Optics, 87-798), expanded and collimated using a lens pair, and linearly polarized using a Glan-Laser polarizer. The excitation is incident on an angled 1064 nm dichroic beamsplitter (Semrock, LPD01-1064RS). This beamsplitter nominally reflects 1064 nm light at a 45° angle of incidence and transmits longer wavelengths, so the beamsplitter is rotated to blue-shift the turn-on wavelength and maximize the reflection of the excitation light. The beam is passed through a half-wave plate affixed to a motorized rotation mount (Standa, 8MR151) that allows fine angular control. A fast steering mirror

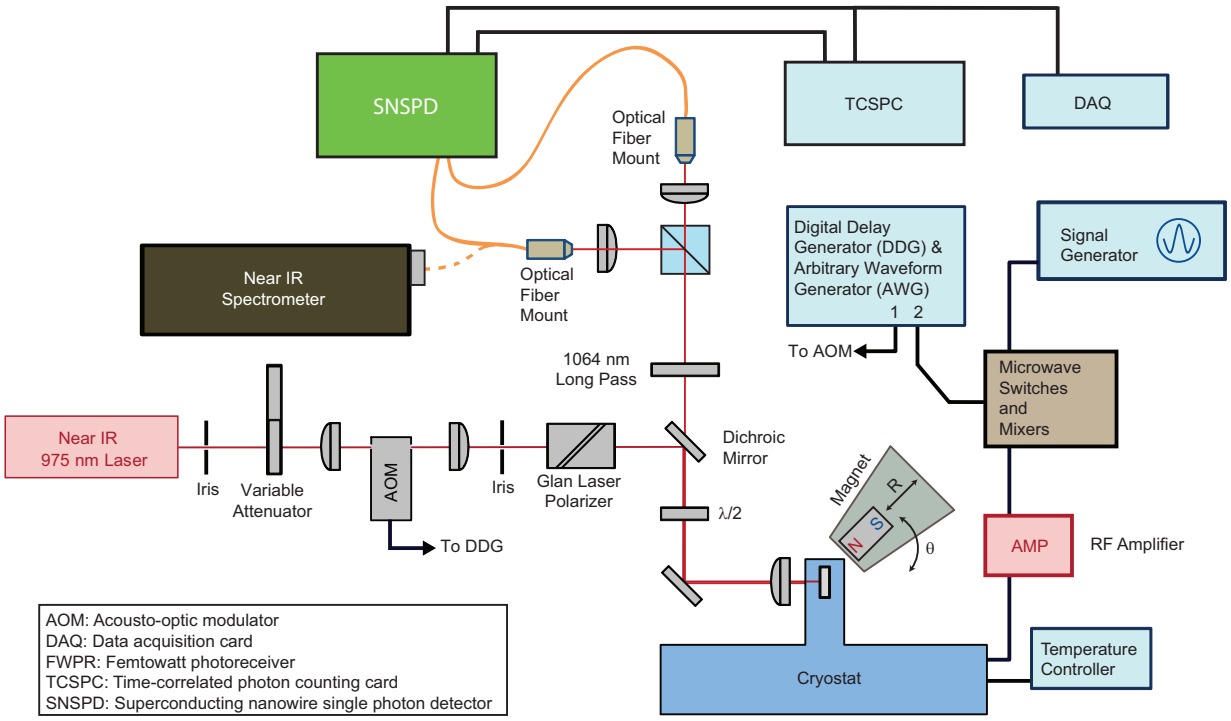

Figure 2.9: Diagram of experimental apparatus.

(Newport, FSM-300) steers the beam before it is passed through an imaging lens pair. A periscope mirror pair affixed to three perpendicular stages (Newport, VP25XL) allows three dimensional movement. The beam overfills a 100x, 0.85 numerical aperture, 1.2 mm working distance, near infrared objective, also mounted to the periscope assembly, that has up to a 0.7 mm coverslip correction (Olympus, LCPLN100XIR). The beam finally passes through the custom 0.65 mm thick, anti-reflection coated, infrared fused silica window (Rocky Mountain Instruments, described in the previous section) of a helium flow cryostat (Janis, ST-500) and is incident on the sample. The photoluminescence (PL) is collected back through the objective and transmitted through the dichroic beamsplitter. Another dichroic beamsplitter (Semrock, LPD01-1064RS) is used as a tunable filter to eliminate PL between about 1.0 μm and 1.1 μm, which was found to materially reduce the unidentified broad background PL in that wavelength range present in initial samples. A 1.0 μm long pass filter (ThorLabs, FELH1000) is used to eliminate any scattered light from the excitation laser. The light is focused into an anti-reflection coated SMF-28e+ single mode fiber. For Hanbury-Brown and

Twiss measurements, the beam can also be split by a near infrared coated, non-polarizing beamsplitter, and focused into two different SMF-28e+ fibers.

Each fiber is connected to a detector port on a commercial superconducting nanowire single photon detector (SNSPD) system. Three such systems were used in this thesis. The first is a NbTiN SNSPD (Single Quantum, EOS) that had about a 28% quantum efficiency, used in all measurements in Chapter 5. Most of the measurements in Chapter 6 were taken using a similar but upgraded system from Single Quantum that has a quantum efficiency above 85%. Some of hyperfine reconstruction measurements in Chapter 6 were taken using a SCONTEL open-cycle SNSPD with an approximately 22% quantum efficiency while the Single Quantum system was being upgraded. These detectors have an adjustable dark count/quantum efficiency tradeoff, and I operated them at a dark count rate of about 100 counts per second in each detector channel (the exact bias is system-dependent). The Single Quantum detectors reside inside a closed cycle cryogenic system, which operates at about 3.1 K. The detectors have a manufacturer-specified timing jitter of about 50 ps. Pulses from the first detector channel are split using a power splitter (MiniCircuits). One path is connected directly to our time correlated photon counting module (PicoHarp, PH300) and the other is passed into a pulse converter (Horiba, TB-01) to convert the short detector pulses into longer TTL pulses that are passed through a switch (MiniCircuits, ZASWA-2-50DR+) and counted by a data acquisition card (National Instruments, X Series). The second detector channel is connected to the other port of the time correlated photon counting module and was only used in this work for anti-bunching measurements. For measurements of PL in the confocal measurement geometry, the second single mode fiber is instead connected to a 62.5 μm core multimode fiber whose output is coupled into an Acton SP-2300i spectrometer. The 0.3 m spectrometer uses a 1.2 μm blaze, 150 g/mm grating to diffract the light onto a Princeton Instruments OMAV InGaAs linear photodiode array. The 1024-pixel photodiode array is cooled to approximately $-95 \circ$ C using liquid nitrogen. The system is calibrated across multiple wavelengths using a Hg(Ar) lamp source, and has a wavelength accuracy of

about $\sigma = 0.2\,\text{nm}$ for the measurements on single defects in Chapters 5 and 6.

2.2.3 Microwave and timing control

The RF signals are generated by a microwave signal generator (National Instruments, PXIe-5652) near 1.3 GHz. After the pulses are formed by the timing electronics, they are passed through an IQ modulator (Polyphase Microwave, AM0350A), a sequence of fixed attenuators (various), a 15.5 dB variable digital attenuator (MiniCircuits, ZX76-15R5-PP+), a 30 W broadband amplifier (MiniCircuits, ZHL-30W-252), and a directional coupler (Narda, 4216-20) before entering the cryostat.

The pulse timing is controlled by a digital delay generator (Stanford Research Systems, DDG-645) for the measurements in Chapter 5, and this device also serves as the master clock for the entire experiment. Most often, this means that one of the output markers triggers a $\approx 1\,\mu$m optical pulse from the acousto-optic modulator that gates the off-resonant laser, a second marker gates a microwave switch connected before the data acquisition card's counter to count the photons emitted only in the first few hundred nanoseconds of the optical pulse, some time on the order of a few hundred nanoseconds is waited, and third marker gates a microwave switch to pass a rectangular microwave pulse through to the amplifier. The effect of the optical pulse is to both read out and initialize the spin state. Because the sequence is repeated continuously, the readout of the previous repetition occurs in the optical pulse of the current repetition. A drawback to the digital delay generator is that each marker can only generator a single rectangular pulse per sequence, and this limits the complexity of the pulse sequences that can be applied in the experiment and the number of devices that can be controlled by it. To rectify this, the Hahn echo measurements in Chapter 5 and all of the measurements in Chapter 6 were done by using an arbitrary waveform generator (Tektronix, AWG5014C). As the name implies, an arbitrary number of rectangular pulses can be synthesized on this device's marker channels, meaning it is easy to sequence, for example, a Hahn echo sequence that requires three microwave pulses ($\pi/2$-π-$\pi/2$) instead

of just one. The analog channels of the arbitrary waveform generator are connected to the I and Q inputs of the IQ modulator, which enables phase control of the microwaves used for spin manipulation. This functionality is used for the Ramsey measurement in Chapter 6 to retain the full spin readout contrast, while the Ramsey measurements in Chapter 5 use the simpler scheme of detuning from resonance the frequency of the microwave pulses used, inducing similar oscillations but at reduced readout contrast. When the arbitrary waveform generator is used, it serves as the master clock for the experiment except in the time-resolved biexponential decay measurements of Chapter 6. There, the arbitrary waveform generator is triggered by the countdown electronics of a pulse picking system based on the Pockels effect (Conoptics 350). These countdown electronics are synchronized to a fast photodiode that records the $\approx 76\,\mathrm{MHz}$ femtosecond pulse train emitted from a Ti:Sapphire laser (Mira 900). The same pairing of a fast photodiode with countdown electronics is also used for the time-resolved biexponential decay measurements in Chapter 3, where an optical parametric oscillator system (Coherent Mira-OPO) is used to convert the infrared pulses emitted from the Ti:Sapphire into visible pulses that can excited NV centers in diamond, and a pulse pattern generator (Agilent) sequences the optical and microwave pulses.

CHAPTER 3

MEASUREMENT AND CONTROL OF SINGLE SPINS IN DIAMOND ABOVE 600K

This chapter and figures are adapted from the publication: "Measurement and control of single nitrogen-vacancy center spins above 600 K*," D. M. Toyli*, D. J. Christle*, A. Alkauskas, B. B. Buckley, C. G. Van de Walle, and D. D. Awschalom, Phys. Rev. X 2, 031001 (2012).*

In this chapter, we study the spin and orbital dynamics of single nitrogen-vacancy (NV) centers in diamond between room temperature and 700 K. We find that the ability to optically address and coherently control single spins above room temperature is limited by nonradiative processes that quench the NV center's fluorescence-based spin readout between 550 and 700 K. Combined with electronic structure calculations, our measurements indicate that the energy difference between the ^{3}E and ^{1}A$_1$ electronic states is approximately 0.8 eV. We also demonstrate that the inhomogeneous spin lifetime (T_2^*) is temperature independent up to at least 625 K, suggesting that single NV centers could be applied as nanoscale thermometers over a broad temperature range.

3.1 Motivations

The negatively-charged nitrogen-vacancy (NV) center spin in diamond stands out among individually addressable qubit systems because it can be initialized, coherently controlled, and read out at room temperature [118]. The defect's robust spin coherence [12] and optical addressability via spin-dependent orbital transitions [97] have enabled applications ranging from quantum information processing [70, 181, 35, 204] to nanoscale magnetic and electric field sensing [166, 11, 65]. While it has been shown that NV center spins can be optically polarized up to at least 500 K [149, 197], little is known about what processes limit the

defect's optical addressability and spin coherence at higher temperatures. Understanding these processes is important to high-temperature field sensing applications and will aid the search for new defect-based spin qubits analogous to the NV center [247, 129] by identifying the aspects of its orbital structure responsible for its high temperature operation.

The NV center's optical spin polarization and optical spin readout result from a spin-selective intersystem crossing (ISC). Although optical transitions between the spin-triplet ground ($^3A_2$) and excited (^3E) states (1.945 eV zero-phonon line [ZPL]) are typically spin conserving, the ^3E state can also relax to the $^3A_2$ state via an indirect pathway that involves a nonradiative, triplet to singlet ISC and subsequent transitions through at least one additional singlet [Fig. 3.1(a)]. The ^3E ISC is much stronger for the $m_s = \pm 1$ ^3E sublevels than for the $m_s = 0$ ^3E sublevel, which facilitates spin readout through the resulting spin-dependent photoluminescence (PL) and initializes the spin into the $m_s = 0$ $^3A_2$ sublevel with high probability ($P_{m_s=0} \sim 0.8$) through repeated optical excitation [161]. Despite the singlet pathway's critical role in preparing and interrogating the spin, open questions remain regarding the number and energies of the singlets involved. Recent experiments have established that it consists of at least two singlets of $^1A_1$ and ^1E symmetry separated by 1.19 eV [205, 4, 158], and have shown that the ^1E state lifetime is strongly temperature dependent below 300 K [4, 203]. The details of the ^3E ISC remain uncertain, however, given computations that suggest the singlet pathway involves three singlets [153] and the lack of direct measurements of the ^3E to singlet transition energy.

Here we report measurements of single NV centers in diamond between 300 K and 700 K. We show that thermally-activated nonradiative processes diminish the spin-selectivity of the ^3E ISC and quench the optical spin readout above 550 K. These measurements indicate the energy barrier for nonradiative relaxation from the ^3E state is ~ 0.5 eV. We perform electronic structure calculations that suggest an orbital structure consistent with a two-singlet decay pathway, our measured energy barrier, and the temperature-dependence of the ^1E state lifetime. Furthermore, we demonstrate that the defect's spin coherence remains

robust even as nonradiative processes quench the optical spin readout. These results suggest nanoscale thermometry applications for single NV centers with sensitivities on the order of $100\,\mathrm{mK}/\sqrt{\mathrm{Hz}}$ between room temperature and 600 K.

3.2 Continuous wave and pulsed magnetic resonance measurements at elevated temperatures

To study single NV centers at elevated temperatures, we constructed devices that combine on-chip heating and thermometry elements, solid immersion lenses (SILs) for enhanced photon collection efficiency [98, 162], and on-chip microwave elements for spin control [Fig. 3.1(b)] [83] (see Appendix A for additional sample details). We studied NV centers in a single-crystal diamond sample ($[\mathrm{N}]^0_\mathrm{S} < 5\,\mathrm{ppb}$) using a home-built confocal microscope. We etched hemispherical SILs around single defects with a focused ion beam, patterned microwave antennas around the NV centers, and patterned a resistive heater on the sample surface. We adhered a commercial resistive temperature detector (RTD) to the diamond and connected the heater and RTD to a temperature controller to achieve stability within $\pm 50\,\mathrm{mK}$ up to 700 K in air.

Continuous-wave (CW) electron spin resonance (ESR) measurements revealed that the NV center's PL intensity (I_PL) and relative I_PL difference between its spin states (ESR contrast) strongly decrease above 550 K. The CW ESR measurements were carried out by applying a swept-frequency AC magnetic field while monitoring I_PL under continuous 532 nm laser excitation. We observed Lorentzian dips in I_PL with normalized amplitude C centered at frequencies corresponding to the ground-state spin resonances [97]. The spin resonance frequencies are determined by the crystal field splitting (D) between the $m_s = \pm 1$ and $m_s = 0$ states, and the Zeeman shift due to an applied magnetic field [150]. We applied a $\sim 45\,\mathrm{G}$ magnetic field along the defect's symmetry axis to separate the $m_s = \pm 1$ states by $\sim 250\,\mathrm{MHz}$. Consistent with measurements performed at lower temperatures [3, 43], we observed shifts in D on the order of $100\,\mathrm{kHz/K}$ due to lattice expansion. In addition to this

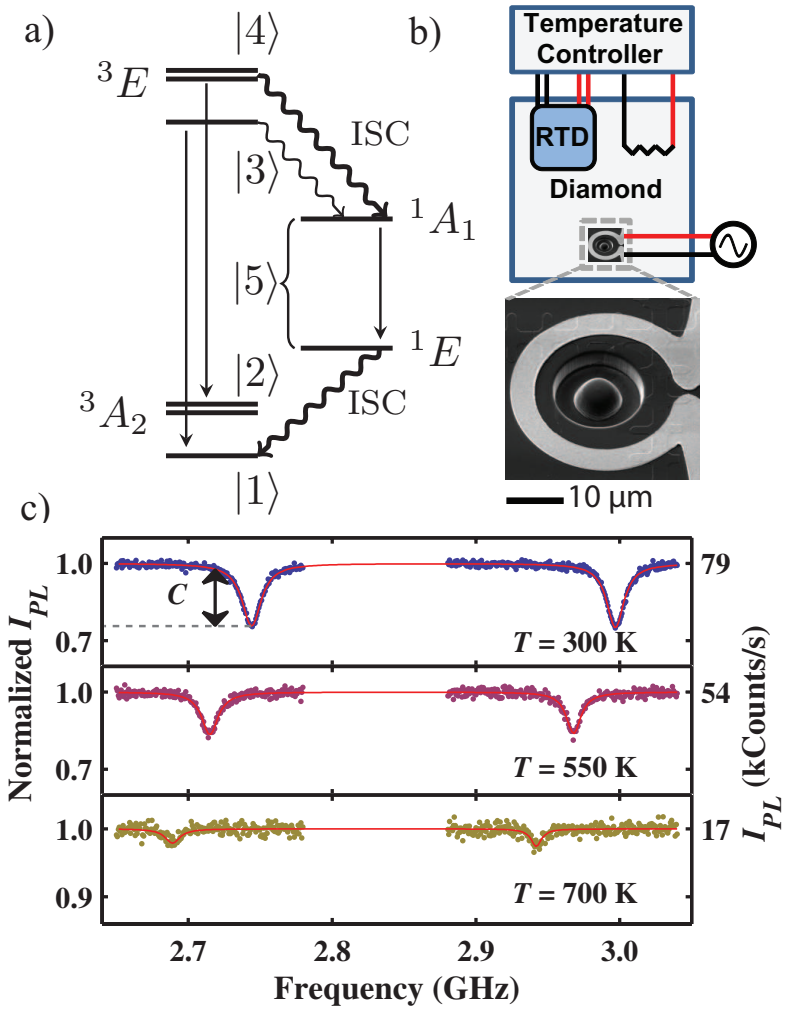

Figure 3.1: **a.** Orbital diagram showing the triplet ($^3A_2$ and ^3E) and singlet ($^1A_1$ and ^1E) electronic states. The straight lines represent optical transitions and the snaked lines represent nonradiative intersystem crossings (ISC). Bra-ket notation denotes the effective levels used to model the photoluminescence intensity (I_{PL}) and electron spin resonance (ESR) contrast. Level $|2\rangle$ ($|4\rangle$) is a grouping of the $^3A_2$ (^3E) $m_s = \pm 1$ sublevels and $|5\rangle$ is an effective singlet level. **b.** Schematic of the sample showing the resistive heater and resistive temperature detector (RTD), the solid immersion lens (SIL), and the antenna. The scanning electron microscope image shows the SIL and the antenna. **c.** I_{PL} of a single NV center versus applied microwave frequency. Lorentzian dips with normalized amplitude C are observed at the spin resonance frequencies ($B \sim 45\,\mathrm{G}$). The left (right) axis shows the normalized (absolute) I_{PL} to illustrate the temperature-dependent decrease in C and I_{PL}. The red lines are two-Lorentzian fits. The crystal field splitting (D) is the average of the resonance frequencies. The measurements were performed at high microwave power to saturate the spin transitions.

shift, both C and the off-resonant I_{PL} showed a pronounced decay above 550 K; by 700 K the Lorentzian dips were barely observable and the off-resonant I_{PL} dropped to $\sim$20% of its room-temperature value [Fig. 3.1(c)].

3.3 Intersystem crossing rates probed by time-correlated photon counting

Thermal quenching of a point defect's I_{PL} often results from thermally activated nonradiative processes that shorten the effective optical lifetime of an emitter [57]. Previous ensemble measurements of the temperature-dependence of the NV center's optical lifetime in bulk diamond [49] and nanodiamonds [189] have shown conflicting results. We therefore have measured the spin-resolved excited-state lifetimes ($\tau_{m_s=0}$ and $\tau_{m_s=\pm1}$) for a single NV center following the method of Ref. [203] to investigate their influence on ESR contrast and I_{PL} above 550 K [Fig. 3.2]. The spin-dependence of the ^3E ISC preferentially shortens $\tau_{m_s=\pm1}$ and thus optical excitation leads to biexponential fluorescence decay, where the decay constants correspond to $\tau_{m_s=0}$ and $\tau_{m_s=\pm1}$ and the relative amplitudes reflect the spin polarization. To probe the lifetimes, we initialized the spin into its $m_s = 0$ state using a 1.4 µs pulse from a 532 nm laser. After waiting 500 ns for the singlets to depopulate, we applied a resonant microwave pulse to rotate the spin into a superposition of $m_s = 0$ and $m_s = -1$. We then applied a 555 nm picosecond laser pulse and measured the resulting PL with a time-correlated photon counting module. We repeated this measurement for varying spin rotation angles and performed global Bayesian inference [136] on the measured decays to infer $\tau_{m_s=0}$, $\tau_{m_s=\pm1}$, and the spin polarizations at each rotation angle (see Appendix A for details on this analysis). Above 550 K, $\tau_{m_s=0}(T)$ showed a sharp reduction, and we found the ground-state spin polarization after optical pumping was temperature independent within our uncertainty up to 650 K (Appendix A).

We find that $\tau_{m_s=0}(T)$ is accurately described by the Mott-Seitz formula for nonradiative

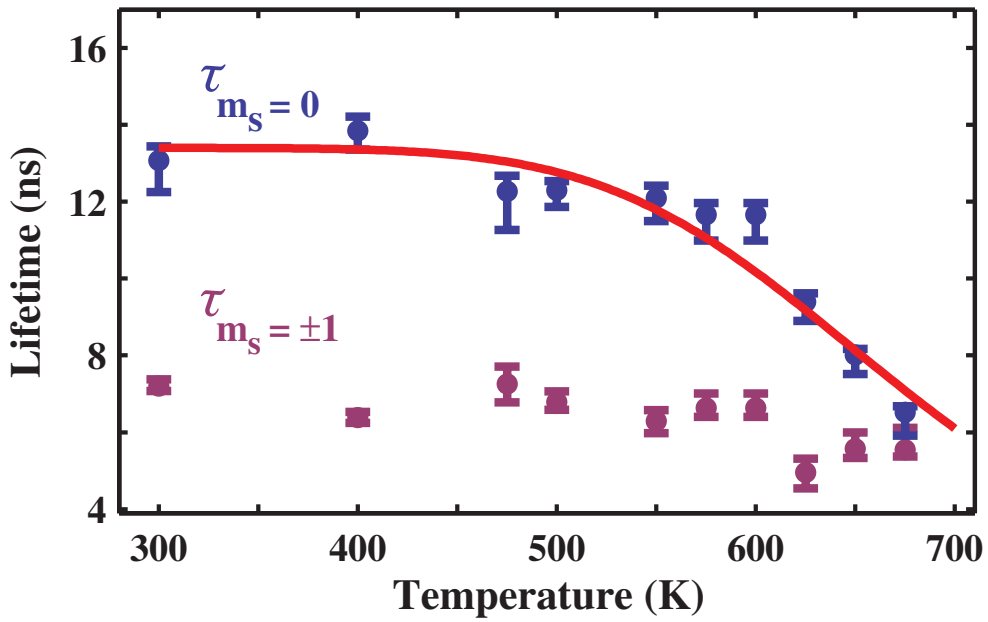

Figure 3.2: Temperature-dependent excited-state lifetimes, $\tau_{m_s=0}(T)$ (blue) and $\tau_{m_s=\pm1}(T)$ (magenta), for a single NV center. The error bars reflect fitting uncertainties (68% intervals). The red line is the Mott-Seitz formula for $\tau_{m_s=0}(T)$ with $\tau_{m_s=0}(300\,\mathrm{K}) = 13.4\,\mathrm{ns}$, $s_{m_s=0} = 3420$, and $\Delta E = 0.48\,\mathrm{eV}$.

relaxation via multiphonon emission [57],

$$\tau_{m_s=0}(T) = \frac{\tau_{m_s=0}(300\,\mathrm{K})}{1 + s_{m_s=0}\exp\left[-\frac{\Delta E}{k_\mathrm{B}T}\right]}, \tag{3.1}$$

where $1/\tau_{m_s=0}(300\,\mathrm{K}) = 1/\tau_\mathrm{rad} + k_{m_s=0}$. Here $1/\tau_\mathrm{rad}$ is the radiative rate, $k_{m_s=0}$ is the room temperature nonradiative transition rate from the ${}^3E$ $m_s = 0$ sublevel to the uppermost singlet state [Fig. 3.1(a)], $s_{m_s=0}$ is the frequency factor, and ΔE is the energy barrier for the nonradiative process. From a fit to $\tau_{m_s=0}(T)$, we find $\tau_{m_s=0}(300\,\mathrm{K}) = (13.4 \pm 0.6)$ ns, $s_{m_s=0} < 1.64 \times 10^4$, and $\Delta E = \left(0.48\,^{+0.15}_{-0.13}\right)$ eV. In general, ΔE is interpreted via a one-dimensional configuration coordinate diagram. These diagrams show the dependence of total energies in different electronic states as a function of a generalized configuration coordinate ΔR. The latter measures the total displacement of all atoms along the path that interpolates between equilibrium geometries in the relevant electronic states. ΔE is then

classically defined as the energy difference between the intersection point of two potential energy curves and the energy minimum of the upper curve. In such a scenario, nonradiative relaxation is a phonon-assisted process over the energy barrier.

3.4 Comparison of experiment with electronic structure calculations

We combine our measurement of ΔE with electronic structure calculations to construct a configuration coordinate diagram for the NV^- center in its $^3A_2$, ^3E, $^1A_1$, and ^1E electronic states. The theoretical methodology employed relies on hybrid density functionals [247, 88]. Additional details regarding the computational methods are provided in Appendix A and Refs. [105, 30, 133, 82, 1, 210, 194, 142]. The calculated ZPL between the triplet states agrees favorably with the experimental value. In Fig. 3.3, we placed the minima of $^3A_2$ and ^3E states according to the experimental ZPL with zero defined by the $^3A_2$ state's equilibrium energy. We also assumed the $^1A_1$ state's equilibrium atomic configuration and vibrational frequencies were equal to those of the $^3A_2$ state given that the $^1A_1$ state's $a_1^2e^2$ electron configuration [167, 62] implies the two states have a similar electron density. Therefore, we estimate the Huang-Rhys factor, the average number of nonequilibrium phonons emitted when the electronic state changes, for the ^3E to $^1A_1$ transition to be ~ 3.2. This confirms our hypothesis that the ISC is accompanied by multiphonon emission, as implied in Eq. (3.1). We interpret ΔE as the energy difference between the intersection point of the ^3E and $^1A_1$ potential energy curves and the energy minimum of the ^3E state. This places the $^1A_1$ state (0.76 ± 0.07) eV below the ^3E state. By fixing ΔE, our analysis avoids difficulties in computing the absolute energies of the singlet states resulting from their multi-determinant electronic wavefunctions [92]. We placed the ^1E state 1.19 eV below the $^1A_1$ state [205, 4, 158] and find that the ^1E singlet is close in energy to the $^3A_2$ triplet. Since the $^3A_2$ state is the ground state, the ^1E state should be higher in energy. Within the uncertainty

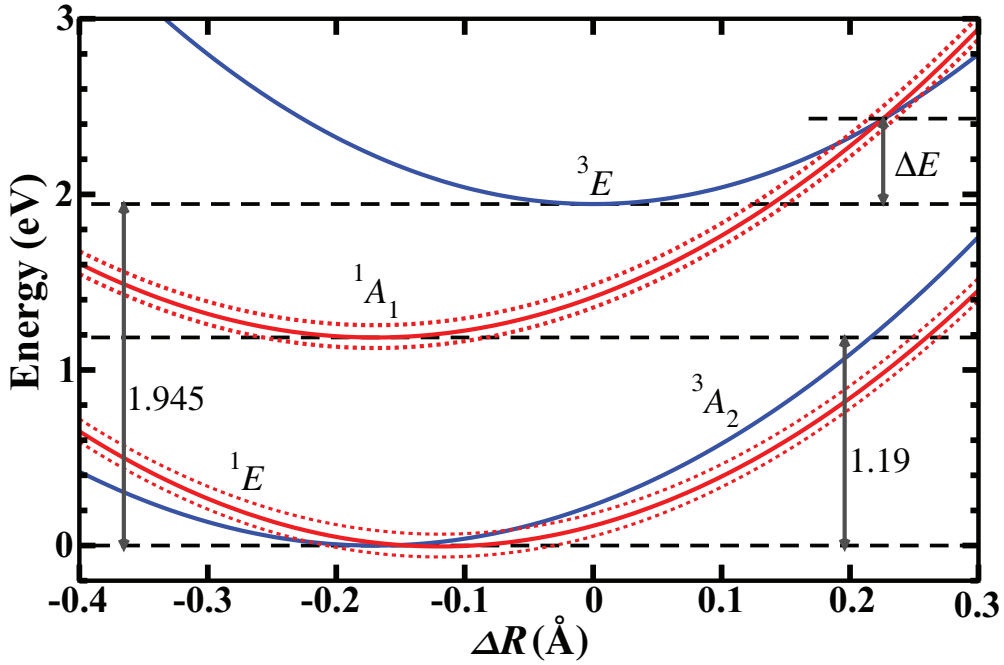

Figure 3.3: Configuration coordinate diagram of the NV^- center. ΔR measures the total displacement of all atoms along the path that interpolates between equilibrium geometries in the $^3A_2$ and ^3E electronic states. All energies are relative to the $^3A_2$ state's equilibrium energy. We placed the $^1A_1$ state based on the assumption that its equilibrium atomic configuration and vibrational frequencies were similar to those of the $^3A_2$ state and using our measurement of ΔE. The ^1E state was placed 1.19 eV below the $^1A_1$ state based on their known energy difference. The uncertainty in the placement of the $^1A_1$ and ^1E states reflects the uncertainty in ΔE (68% interval, dashed red lines). The triplet (1.945 eV) and singlet (1.19 eV) zero phonon lines are also indicated.

in ΔE, the configuration coordinate diagram fulfills this constraint and indicates that only small energy barriers for nonradiative relaxation from the ^1E state are possible in qualitative agreement with energy barriers inferred from the temperature-dependence of the ^1E state lifetime [4, 203]. Our inference of the $^1A_1$ and ^1E energies is likely influenced by our classical interpretation of ΔE, which is based on the consideration of a single effective phonon mode. A more complete analysis considering quantum effects [57] and coupling of the spin to many quasi-localized phonon modes of different symmetry [158] appears desirable for a deeper understanding of the spin-selective orbital transition.

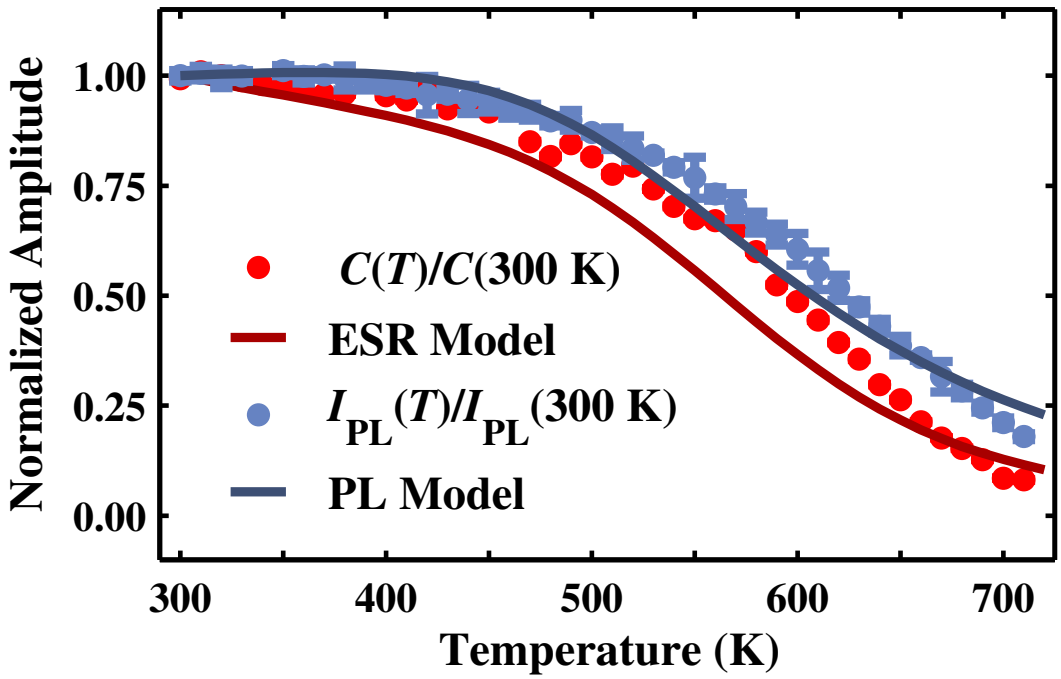

Figure 3.4: Temperature-dependent ESR contrast ($C(T)$, red points) and $I_{\mathrm{PL}}(T)$ (blue points). Both quantities were normalized by their 300 K values ($\sim$0.22 and $\sim$80 kCps, respectively). $C(T)$ was determined from fitting the CW ESR data and I_{PL} was determined from Gaussian fits to confocal microscopy line scans. The solid lines represent predictions for $C(T)/C(300\,\mathrm{K})$ and $I_{\mathrm{PL}}(T)/I_{\mathrm{PL}}(300\,\mathrm{K})$ from a model of the CW ESR experiments depending on $\tau_{m_s=0}(T)$ and $\tau_{m_s=\pm1}(T)$. Fig. 3.2 and Fig. 3.4 present data from the same NV center.

3.5 Dynamical model of intensity and contrast behavior

Having interpreted ΔE, we employ a model of the ESR experiments using the density matrix formalism that includes dissipation to reveal that the observed decreases in C and I_{PL} are predominantly caused by the temperature dependence of $\tau_{m_s=0}$ and $\tau_{m_s=\pm1}$ [193]. The model consists of irreversible transitions between five effective energy levels [Fig. 3.4(a)] under optical pumping with an off-diagonal term to capture the coherent microwave driving. The only temperature-dependent components are $\tau_{m_s=0}$, $\tau_{m_s=\pm1}$, and the known temperature-dependence of the effective singlet lifetime [203]. The model shows agreement with our measurements of $C(T)/C(300\,\mathrm{K})$ and $I_{\mathrm{PL}}(T)/I_{\mathrm{PL}}(300\,\mathrm{K})$ [Fig. 3.4]. It reveals that the small decrease in C below 550 K is due to shortening of the singlet lifetime while the decreases in both C and I_{PL} above 550 K are primarily caused by the thermally-activated nonradiative processes that shorten $\tau_{m_s=0}$ and $\tau_{m_s=\pm1}$.

We established from pulsed ESR measurements that the NV center remains spin coherent even as nonradiative processes diminish the ESR contrast and I_{PL}. The robust coherence of the spin is due to the equal population of the sublevels of the electronic and nuclear spin impurities which decohere the spin at all but cryogenic temperatures [231]. We performed these measurements by polarizing the spin with a 532 nm CW laser pulse, coherently manipulating the spin with resonant microwaves, and reading out the spin state by monitoring the PL [118]. Both Rabi [Fig. 3.5(a)] and Ramsey pulse sequences were employed, demonstrating that the spin can be coherently controlled at temperatures exceeding 600 K and showing I_{PL} and ESR contrast trends consistent with the fluorescence quenching observed in our CW ESR measurements. Moreover, fits to the Ramsey oscillation decay envelope showed T_2^* is independent of temperature up to at least 625 K [Fig. 3.5(b)]. We also performed longitudinal relaxation measurements that demonstrated T_1 at 600 K (340(50) µs) was still much longer than the period of the pulsed ESR measurements, indicating that spin relaxation does not explain the observed decrease in the ESR contrast and I_{PL}.

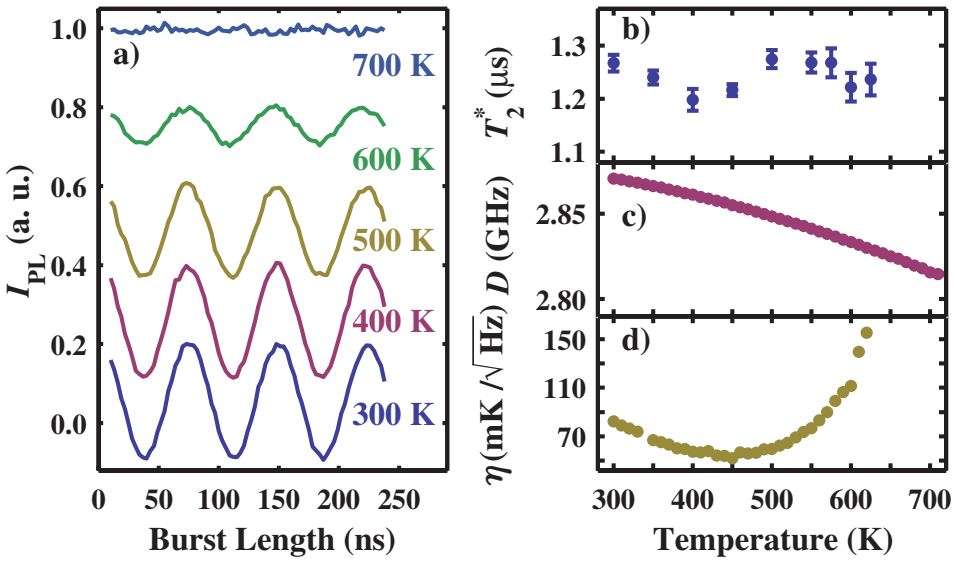

Figure 3.5: **a.** I_{PL} versus the resonant microwave burst length on the $m_s = 0$ to $m_s = -1$ transition (Rabi oscillations). The measurements are offset for clarity. **b.** T_2^* versus temperature inferred from the decay envelope of fits to Ramsey oscillations. These measurements were performed at ~500 G to polarize the NV center's ^{14}N nuclear spin to simplify its hyperfine spectrum. All other measurements were performed at ~ 45 G. **c.** $D\,(T)$ inferred from Lorentzian fits to the CW ESR data. **d.** Single-spin thermal sensitivity (η). η was calculated using Eq. (3.2) with all parameters from the same NV center. Error bars represent 68% intervals.

3.6 Thermometry using a single spin

The persistence of the spin coherence and the strong temperature dependence of D suggest the possibility of using the spin resonances for thermometry at temperatures inaccessible to conventional magnetic resonance thermometers [27]. Based on our CW ESR measurements, we find that $D(T)$ [Fig. 3.5(c)] is accurately described by a third-order polynomial between 300 K and 700 K, with thermal shifts ranging from 80 kHz K^{-1} to 170 kHz K^{-1}. The possibility of nanoscale thermometry is further motivated by diamond's ideal thermal and mechanical properties, the established methods for measuring small NV center Zeeman shifts [166, 11, 2, 211], and the potential for nanometer-scale thermal imaging using NV centers in diamond nanocrystals. We quantify the thermal sensitivity (η) based on our measurements of the temperature-dependent optical and spin properties using an expression analogous to those derived for NV center DC magnetic field sensitivities with a Ramsey pulse sequence [234]:

$$\eta(T) = \frac{1}{2\pi \frac{dD(T)}{dT} S(T) \sqrt{T_2^*}}, \tag{3.2}$$

where $S(T)$ is a parameter that accounts for the finite photon count rate and ESR contrast and $S(300\,\mathrm{K}) \sim 0.02$. Evaluating Eq. (3.2) with measured parameters from a single NV center, we find that η is $\sim$100 mK/$\sqrt{\mathrm{Hz}}$ between room temperature and 600 K [Fig. 3.5(d)]. This sensitivity could be enhanced for defects in isotopically pure diamond which can exhibit T_2^* times greater than 100 µs [116], corresponding to η better than 10 mK/$\sqrt{\mathrm{Hz}}$. These results demonstrate that NV centers offer operating temperatures and thermal sensitivities relevant to studies of thermal gradients in microscale and nanoscale systems such as nanostructured thermoelectrics [219, 214] and living cells [252].

3.7 Conclusions

The results presented here provide fundamental insights on how thermally-driven nonradiative processes can influence the fluorescence properties of defect-based spin qubits. We show

that the NV center's fluorescence-based spin readout is ultimately limited above room temperature by nonradiative processes that diminish the spin-selectivity of its ^3E to $^1A_1$ orbital transition and upset the balance between the defect's radiative and nonradiative relaxation rates. Coupled with the persistence of its spin coherence, these measurements suggest the NV center could find application as a nanoscale thermal sensor over a broad temperature range.

CHAPTER 4

FLUORESCENCE THERMOMETRY ENHANCED BY THE QUANTUM COHERENCE OF SINGLE SPINS IN DIAMOND

This chapter and figures are adapted from the publication: "Fluorescence thermometry enhanced by the quantum coherence of single spins in diamond" D. M. Toyli, C. F. des las Casas, D. J. Christle, V. V. Dobrovitski, and D. D. Awschalom, Proc. Natl. Acad. Sci. USA 110, 8417 (2013).

4.1 Motivations

Thermometry based on thermally driven changes in fluorescence lifetimes or intensities are essential techniques in many environments that preclude electrical probes[94]. Although typical fluorescence thermometers utilize millimeter-scale optical probes [6], the desire to non-invasively monitor intracellular thermal gradients has motivated efforts to develop analogous methods at the nanoscale[33, 115]. This interest has stimulated the development of nanoscale fluorescence thermometers based on quantum dots [245], rare-earth ions [243], and nanogels [93], with recent studies suggesting that intracellular temperature gradients are on the order of 1 K [183]. However, the application of conventional fluorescence thermometry techniques in biological settings is limited by temperature resolutions of ≈ 0.2 K or worse [183, 67, 252], motivating the development of more advanced nanoscale thermometers.

In recent years solid-state electronic spins have gained considerable attention for applications in nanoscale sensing. In particular, the diamond nitrogen-vacancy (NV) center (Fig. 4.1a) has garnered attention for its optical spin initialization and fluorescence-based spin readout [241], the ability to isolate and measure single defects [97], and the ability to manipulate its spin using microwave electron spin resonance techniques [118]. NV center sensing is based on monitoring shifts in the spin resonance frequencies through the defects

fluorescence as a function of external perturbations such as magnetic fields [110, 95, 156, 228], electric fields [66], or temperature [236, 3], with the sensitivity of these techniques scaling as $1/\sqrt{T_C}$, where T_C is the relevant spin coherence time[234]. These coherence times can be enhanced by 2-3 orders of magnitude for perturbations amenable to AC modulation through the use of dynamical decoupling techniques that periodically invert the spin state and the signal being sensed in order to mitigate the effects of low-frequency magnetic noise [53, 207, 179]. These methods have enabled the detection of single electronic spins [95] and nanoscale nuclear spin ensembles external to the diamond [156, 228], with motivations to extend these techniques to biological systems using NV centers in nanodiamonds [168].

Here we demonstrate that the quantum coherence of a single NV center can enhance thermometry. Our technique relies on the use of dynamical decoupling protocols that manipulate the NV center's spin-1 ground state to maintain DC sensitivity to thermally driven shifts in the spin resonance frequencies while suppressing the effects of low frequency magnetic noise. This allows us to exploit the NV centers long spin coherence for thermometry. We achieve spin coherence times for thermal sensing exceeding $80\,\mu$s, resulting in inferred thermal sensitivities of $25\,\mathrm{mKHz}^{-1/2}$. By combining these prolonged coherence times with improved fluorescence detection [10], we estimate that thermal sensitivities better than $10\,\mathrm{mKHz}^{-1/2}$ should be achievable. These sensitivities demonstrate the NV centers potential to markedly improve on the $\approx 0.2\,\mathrm{K}$ temperature resolution offered by competing nanoscale fluorescence thermometry techniques [33, 115, 183, 67, 252]. We execute these measurements in two regimes: in moderate magnetic fields where both spin transitions can be resonantly addressed with separate microwave signals and near zero magnetic field where they can be addressed with a single microwave frequency. Finally, we demonstrate the wide range of operating temperatures for NV center thermometers by performing these measurements at $500\,\mathrm{K}$. Together, these results provide a robust set of protocols for NV center based thermometry.

4.2 Principles of spin-based fluorescence thermometry

Our work focuses on the precise measurement of the NV centers temperature-dependent crystal field splitting (D) between its $m_s = 0$ and $m_s = \pm 1$ sublevels, as seen in the ground-state spin Hamiltonian [150]:

$$H_{\mathrm{NV}} = DS_z^2 + g\mu_{\mathrm{B}}\vec{B}\vec{S} + \vec{S}\overline{A}\vec{I} \tag{4.1}$$

Here $\mathbf{S}$ is the electronic spin operator, $g = 2.00$ is the electron g factor, $_{\mathrm{B}}$ is the Bohr magneton, $\vec{B}$ is the applied magnetic field, $\overline{A}$ is the hyperfine tensor, and $\vec{I}$ is the nitrogen nuclear spin operator ($I = 1$). Additional considerations regarding Eq. (1), such as the influence of strain and electric fields, are discussed in Appendix B. The crystal field splitting, approximately 2.870 GHz at room temperature, exhibits shifts of -74 kHz/K due to thermal expansion [3] and vibronic interactions [63]. Since the D term is second order in S_z, ground-state level shifts due to changes in temperature can be distinguished from Zeeman shifts (Fig. 4.1b). This point has recently been used to perform NV center magnetometry that is insensitive to temperature drift[75]. Here we take the opposite approach to perform thermometry that is robust against the NV center's interactions with its magnetic environment. Our approach is to resonantly manipulate the spin such that at specific times the relative phase of the spin states in the laboratory frame becomes $e^{(-iDt)}$, where t is the spins total free evolution time. As this phase is independent of the magnetic field (up to fluctuations on the timescale of the inter-pulse delay, τ), it is protected from the low-frequency magnetic fluctuations that limit the coherence to the inhomogeneous spin lifetime (T_2^*). Similarly, the phase is independent of the nitrogen nuclear spin state, thus eliminating interference effects observed in conventional DC sensing techniques based on Ramsey measurements (Fig. 4.1c). This relative phase is then converted into a population difference of the spin sublevels and measured through the fluorescence intensity (I_{PL}). The fluorescence is $\approx 30\%$ greater for the $m_s = 0$ state than for the $m_s = \pm 1$ states, and varies linearly with the $m_s = 0$ spin

population, providing a direct measurement of the NV center spin. This measurement sequence is repeated until the desired level of I_{PL} is reached. As a function of t, the I_{PL} signal oscillates between $I_{\mathrm{PL}}(m_s = 0)$ and $I_{\mathrm{PL}}(m_s = \pm 1)$ with a frequency given by $D\Omega_{\mathrm{REF}}$, where Ω_{REF} corresponds to the microwave carrier frequencies used for spin manipulation. Small thermally driven changes in D (as well as the value of D itself) can therefore be measured through large changes in the NV center's fluorescence.

4.3 Fluorescence thermometry in finite magnetic fields

We first demonstrate 'thermal' analogs to conventional Hahn echo and CPMG-N pulse sequences [217] in finite magnetic fields, where both the $m_s = 0$ to $m_s = -1$ and $m_s = 0$ to $m_s = +1$ transitions are resonantly addressed. After optically initializing the spin into the $m_s = 0$ sublevel with a $\approx 2\,\mu$s laser pulse, we apply one of the pulse sequences shown in Figure 2A, referred to here as the thermal echo (TE) and thermal CPMG-N (TCPMG-N). These pulse sequences follow the same general methodology: the spin is first initialized into a superposition of two of its three eigenstates and then undergoes periods of free evolution punctuated by operations of the form $\pi_{+1}\pi_{-1}\pi_{+1}$ or $\pi_{-1}\pi_{+1}\pi_{-1}$, where the subscripts indicate the spin transition being addressed; e.g., π_{-1} acts on the $m_s = 0$ to $m_s = -1$ transition. These operations interchange the spin populations in the $m_s = +1$ and $m_s = -1$ states, thus inverting the NV center spin state. As a result of the inversions, the $m_s = +1$ and $m_s = -1$ states acquire a total phase $e^{(-iDt)}$, which is independent of static magnetic fields and low-frequency magnetic noise. The final microwave pulse converts this phase into a population of the mS = 0 state, which is measured optically. The key difference between the TE and TCPMG-N sequences is that the TCPMG-N sequences invert the spin more frequently ($2N$ times), and thus counteract higher-frequency magnetic noise. Note that the final -1+1-1 operation in the TE sequence compensates for undesired phases acquired during the duration of the π pulses and the interpulse delays (see Appendix B for more details). The TCPMG-N sequences also include two symmetrized -1+1-1 operations per period, compen-

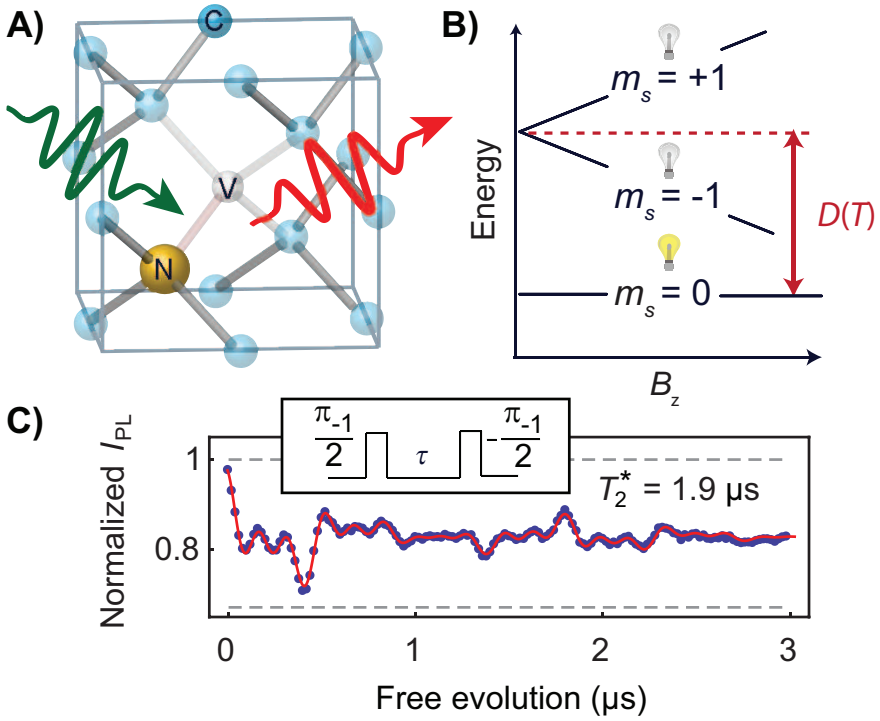

Figure 4.1: **a.** Depiction of a nitrogen vacancy (NV) center in the diamond lattice. The wavy green arrow represents the 532 nm laser used for optical excitation and the wavy red arrow represents the phonon-broadened fluorescence used to measure the spin state. **b.** Fine structure of the NV center ground state as a function of axial magnetic field. The light bulbs represent the relative fluorescence difference for the $m_s = 0$ and $m_s = \pm 1$ states. Temperature changes shift the crystal field splitting (D), whereas magnetic fields (B) split the $m_s = \pm 1$ sublevels. This difference enables dynamical decoupling pulse sequences that move the spin between all three states to selectively measure temperature shifts and mitigate magnetic noise. **c.**, Ramsey measurement performed on the $m_s = 0$ to $m_s = -1$ transition ($B_z = 40$ G). The inset illustrates the pulse sequence. The short inhomogeneous spin lifetime (T_2^*) limits the sensitivity of conventional NV center thermometry. The uncertainties in I_{PL}, estimated from the photon shot noise, are ≈ 0.003. The microwave carrier frequency was detuned from the $m_I = 0$ hyperfine resonance by ≈ 3.5 MHz to induce oscillations in I_{PL}. The fluorescence signal exhibits a beating caused by the three hyperfine resonances and weak coupling to a nearby ^{13}C spin. The gray dashed lines show the fluorescence intensity of $m_s = 0$ and $m_s = -1$ as determined by independent measurements.

sating for these undesired phase accumulations and providing better protection from noise [99]. We apply these pulse sequences to a single NV center in a diamond with natural ^{13}C abundance (1.1%) in a magnetic field ($B_z = 30\,\mathrm{G}$). In these materials the ^{13}C nuclear spins ($I = \frac{1}{2}$) are the primary source of decoherence, limiting T_2^* to a few microseconds. Conventional Hahn echo measurements can extend the coherence to hundreds of microseconds, but are limited by the incoherent precession of the ^{13}C nuclei, which causes the coherence to collapse and revive at the ^{13}C Larmor frequency[44]. Previous studies demonstrated that dynamical decoupling sequences, such as CPMG-N, can counteract the ^{13}C precession to maintain coherence over significantly enhanced timescales[207], and here we demonstrate that this coherence can be accessed for DC thermal sensing. Our focus is on extending the timescale of the first coherence collapse, since our three-level pulse protocols lead to three incommensurate ^{13}C precession frequencies that do not produce the coherence revivals observed in the two-level Hahn echo[199]. Figure 2B shows the Hahn echo coherence, with the width of the gray shaded region corresponding to the spin's T_2^*. The TE sequence achieves a coherence time similar to that of the Hahn echo sequence, approximately four times greater than T_2^* (Fig. 4.2c). The TCPMG (Fig. 4.2d) and TCPMG-2 (Fig. 4.2e) sequences extend the spin coherence even further in time. The coherence time reaches $17.6\,\mu$s for TCPMG-2, corresponding to a 9x improvement in coherence over T_2^* and a 3x improvement in thermal sensitivity (η) as compared to a Ramsey measurement. Using Eq. (4) described in the Methods, which is based on monitoring thermally driven changes in I_{PL} at the free evolution time which mutually optimizes the coherence and accumulated phase, we infer that for these experimental parameters η is (54 ± 1) mK Hz$^{-1/2}$. Combining our observed coherence with higher photon collection efficiencies achieved in scanning diamond magnetometers (34) could improve η to $\approx 15\,\mathrm{mK\ Hz^{-1/2}}$.

Our measurements show good agreement with the results of numerical modeling for the spin dynamics of an NV center in a ^{13}C spin bath subjected to the TE and TCPMG-N sequences (solid green lines in Fig. 4.2b-e; see Appendix B for further details). We note

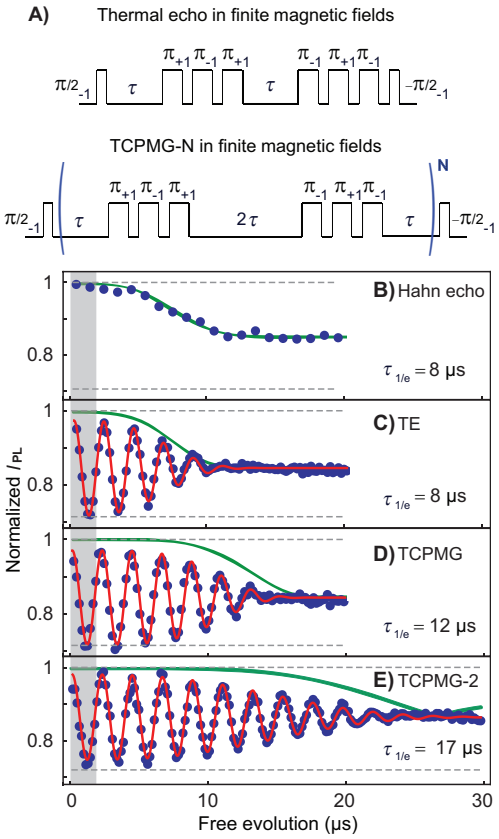

Figure 4.2: **a.** Diagram showing the thermal echo (TE) and thermal CPMG-N (TCPMG-N) pulse sequences in finite magnetic fields. Here a π-pulse has a duration such that it will invert the spin population between the two sublevels that are resonantly addressed. The subscripts indicate the spin transition being addressed. **b.** Hahn echo measurement ($m_s = 0$ to $m_s = -1$ transition) at $B = 30\,\mathrm{G}$ showing I_{PL} as a function of the free evolution time (2τ for the Hahn echo and TE, 4τ for TCPMG and 8τ for TCPMG-2). The measurement demonstrates the coherence collapse caused by the incoherent precession of the ^{13}C spin bath. The width of the shaded gray region represents T_2^*. Panels C, D, and E, show TE, TCPMG, and TCPMG-2 measurements, respectively, performed at 297.00 K (see Appendix B). The uncertainties in I_{PL}, estimated from the photon shot noise, are ≈ 0.005. In order to induce oscillations in I_{PL} to clearly observe the signal envelope, the average microwave carrier frequency (Ω_{REF}) was detuned from D by $\approx 0.5\,\mathrm{MHz}$. The solid red lines are best fits to the data and the $1/e$ decay times ($\tau_{1/e}$) are noted on the plots. The observed coherences are in good agreement with numerical modeling (solid green lines). For the TCPMG-2 sequence the coherence time is 9x greater than T_2^*. For these experimental conditions we infer the thermal sensitivity (η) is $(54 \pm 1)\,\mathrm{mK\,Hz^{-1/2}}$. Enhancements in the photon collection efficiency (see the Methods) could improve η to $\approx 15\,\mathrm{mKHz^{-1/2}}$.

that the difference between the modeling results and the experimental data is larger for the sequences involving more pulses, suggesting that they are caused by pulse imperfections. Interestingly, the simulations for TCPMG-2 (Fig. 4.2e) show a distinct feature near 25 μs, when the coherence collapses and then revives with a 180° shift in phase in the oscillations. We have observed similar behavior on other NV centers in our diamond sample (see Appendix B) and tentatively attribute these features to coupling to the most proximal ^{13}C nuclei[44]. The overall correspondence between the coherence observed in the measurements and in the numerical simulations supports the assertion that the ^{13}C nuclear spins are a primary limiting factor for these measurements. These observations suggest that the ^{13}C dynamics could be further suppressed to produce improved thermal sensitivities not only through the application of higher order TCPMG-N sequences, but also by reducing the magnetic field to lower the ^{13}C precession frequency.

4.4 Fluorescence thermometry near zero magnetic field

Near zero magnetic field, the bandwidth of the resonant microwave pulses exceeds the spectral width of the $m_s = +1$ and $m_s = -1$ resonances, and the thermal echo can be performed with a single microwave source (Fig.4.3a). We consider near-zero magnetic fields ($B_z \approx 0.5\,\mathrm{G}$) to mitigate mixing of the $m_s = \pm 1$ states induced by transverse strain[64]. In this limit the TE sequence has an analogous form to pulse sequences proposed for NV center timekeeping (35), where the pulse that inverts the spin state has a duration such that a spin initially in mS = 0 goes through a superposition of mS = 1 and returns to mS = 0 with an opposite sign.

In this small magnetic field, the TE sequences produce longer coherence times of $\approx 85\,\mu$s (Fig. 4.3b), in good agreement with numerical simulations. This improves the inferred η to $(25 \pm 2)\ \mathrm{mK\,Hz^{-1/2}}$ for these measurements and we estimate that improved fluorescence detection techniques could improve η to $\approx 7\,\mathrm{mK\,Hz^{-1/2}}$. To show the sensitivity of this coherence to temperature shifts, we perform a direct experimental demonstration where we

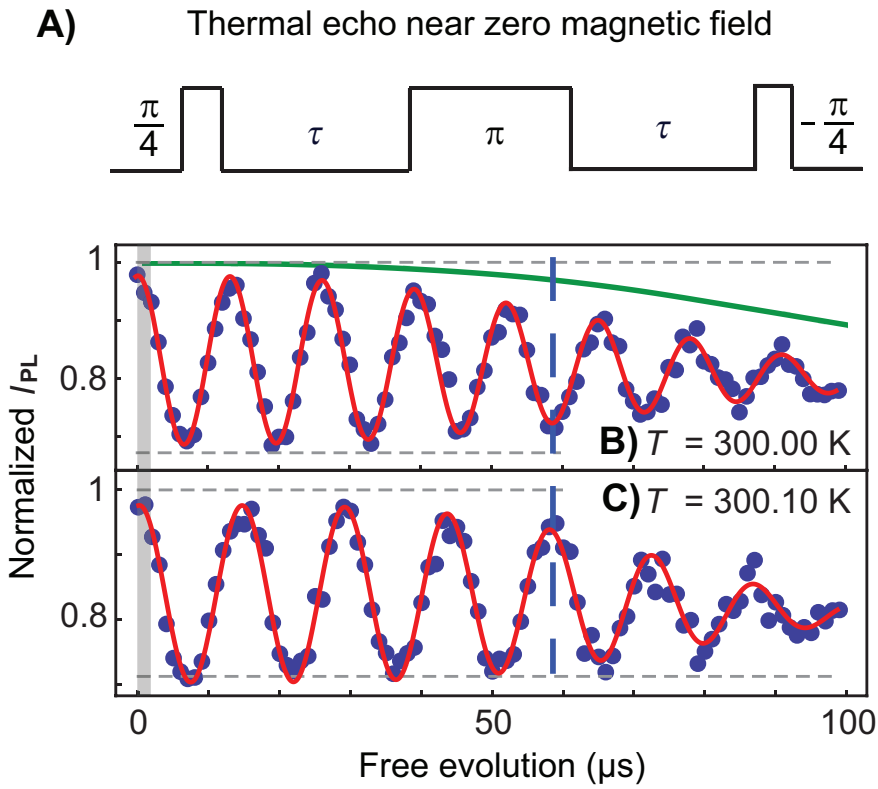

Figure 4.3: **a.** Diagram showing the thermal echo pulse sequence in zero magnetic field when the frequency separation of the $m_s = \pm 1$ sublevels is less than the bandwidth of the microwave pulse used to address the transitions (25 MHz). Here a π-pulse has a duration such that the spin, initialized into $m_s = 0$, goes through a superposition of the $m_s = \pm 1$ states and returns to $m_s = 0$ with an opposite sign. **b.** Thermal echo measurement at 300.00 K. The microwave carrier frequency (Ω_{REF}, 2.87016 GHz) was detuned from D by ≈ 75 kHz in order to induce oscillations in the signal to observe the coherence envelope. The solid green line shows the coherence predicted by the numerical modeling. The width of the shaded gray region represents T_2^*. **c.** The same measurement as in b, but with the sample temperature at 300.10 K. The shift in D results in a pronounced difference in the signal frequency leading to large I_{PL} differences at long times (dashed blue line). For both measurements $\tau_{1/e}$ is $\approx 85\,\mu$s, and the uncertainties in I_{PL}, estimated from the photon shot noise, are ≈ 0.02. For reference, for these data the measurement time per point was 50 seconds. From the observed coherence times we infer η is (25 ± 2) mK Hz$^{-1/2}$ for these experimental conditions; we estimate that enhanced photon collection efficiencies could improve η to ≈ 7 mK Hz$^{-1/2}$. The frequency difference for the oscillations in B and C, inferred from the fits, is (8 ± 2) kHz, in good agreement the expected value ≈ 7.4 kHz (20).

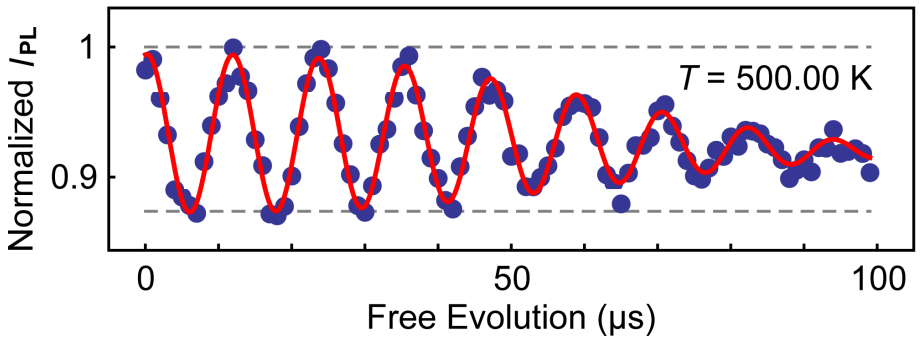

Figure 4.4: A similar measurement to those presented in Fig. 4.3 performed at 500.00 K. Here Ω_{REF}, 2.84818 GHz, has been adjusted to compensate for the large shift in D such that a detuning of $\approx$ 80 kHz is achieved. The uncertainties in I_{PL}, estimated from the photon shot noise, are $\approx$ 0.007. The measurement shows a reduced I_{PL} contrast between the spin states, primarily due to an increased fluorescence background on this sample at elevated temperatures. However, the larger thermal shifts in D (-140 kHz/K at 500 K, Ref. (19)), largely compensate for this reduction to produce an inferred η of (39 ± 6) mK Hz$^{-1/2}$ for this measurement. The projected η for enhanced photon collection efficiencies is $\approx$ 11 mK Hz$^{-1/2}$.

increase the temperature of the diamond substrate by 0.1 K while keeping the microwave carrier frequency (Ω_{REF}) fixed (Fig. 4.3c). The change in the accumulated phase of the $m_s = +1$ and $m_s = -1$ states produces a pronounced change in the I_{PL} signalthe dashed blue line spanning Figure 3B and Figure 3C draws attention to when the two signals have opposite phase. As the 0.1 K shift is clearly resolved, these measurements demonstrate that NV centers could offer a significant improvement in thermal sensitivity relative to alternative nanoscale fluorescence thermometers (3, 4, 8-10). Even longer coherence times approaching $\approx$ 1 ms, achieved through the application of higher order decoupling sequences or the use of isotopically purified diamond to eliminate the ^{13}C spin bath (36), could further improve the thermal sensitivities from those discussed here.

Finally, to demonstrate the versatility of these NV center thermometry techniques, we perform a similar TE measurement at 500 K (Fig. 4.4). This measurement shows a coherence similar to the 300 K thermal echoes as expected from the temperature-independence of the ^{13}C spin bath (19) and the sufficiently long spin-lattice relaxation time ($\approx$ 1 ms) at this temperature (37). The 500 K TE does show a reduced fluorescence contrast, predom-

inantly due to an increased fluorescence background at this temperature. However, this measurement still achieves a comparable η of $(39 \pm 6)\,\mathrm{mK\,Hz^{-1/2}}$ due to the larger shift in D ($-140\,\mathrm{kHz/K}$ at $500\,\mathrm{K}$), while enhanced photon collection efficiencies could provide an η of $\approx 11\,\mathrm{mK\ Hz^{-1/2}}$. The robust temperature dependence of these spin-based thermometry methods suggests they could be applied in a variety of contexts beyond intracellular sensing such as diamond-based scanning thermal microscopy (34, 38).

4.5 Conclusions

These results illustrate the NV centers promise for nanoscale thermometry applications by demonstrating dynamical decoupling techniques that harness the NV centers long spin coherence for thermal measurement. By utilizing this quantum degree of freedom, we achieve thermal sensitivities that approach $10\,\mathrm{mK\,Hz^{-1/2}}$, demonstrating the NV center's potential to improve on existing nanoscale fluorescence thermometry techniques by an order of magnitude. While these results are obtained using single NV centers in high-quality synthetic diamond, the development of diamond nanostructures containing highly coherent NV centers (39, 40) suggests a pathway for fabricating nanodiamonds that achieve similar sensitivities. Such nanostructures could enable high precision thermometry in biological and microfluidic systems with sub-diffraction spatial resolution defined by the size of the nanodiamonds. Furthermore, scanning thermal measurement in fluids will benefit from recent advances in the three-dimensional spatial control and rotational control of optically trapped nanodiamonds containing NV centers (41, 42). These compelling applications suggest the potential impact of nanoscale thermometers that combine the solid-state quantum coherence of NV centers demonstrated here with the biocompatibility, hardness, and high thermal conductivity of diamond.

CHAPTER 5

ISOLATED ELECTRON SPINS IN SILICON CARBIDE WITH MILLISECOND COHERENCE TIMES

This chapter and figures are adapted from the publication: "Isolated electron spins in silicon carbide with millisecond coherence times," D. J. Christle, A. L. Falk, P. Andrich, P. V. Klimov, J. Ul Hassan, N. T. Son, E. Janzén, T. Ohshima, and D. D. Awschalom, Nat. Mater. 14, 160-163 (2015).

5.1 Motivations

The elimination of defects from silicon carbide (SiC) has facilitated its move to the forefront of the optoelectronics and power-electronics industries[208]. Nonetheless, because certain SiC defects have electronic states with sharp optical and spin transitions, they are increasingly recognized as a platform for quantum information and nanoscale sensing[13, 224, 242, 247, 129, 14, 86, 200, 220, 72, 125, 41, 132, 36]. Here, we show that individual electron spins in high-purity monocrystalline 4H-SiC can be isolated and coherently controlled. Bound to neutral divacancy defects[13, 224], these states exhibit exceptionally long ensemble Hahn-echo spin coherence times, exceeding 1 millisecond. Coherent control of single spins in a material amenable to advanced growth and microfabrication techniques is an exciting route to wafer-scale quantum technologies.

The control of isolated electron spins is a promising basis for an array of new technologies, ranging from quantum communication[23] to nanoscale nuclear magnetic resonance[156, 228] and intracellular sensing of magnetic, electric and thermal fields[236, 237, 135]. By exploiting spin-dependent optical transitions, optically detected magnetic resonance (ODMR) has proven to be a powerful technique for achieving single-spin addressability in the solid state[251, 97]. As with the diamond nitrogen-vacancy (NV) center[23, 236, 237, 97], a partic-

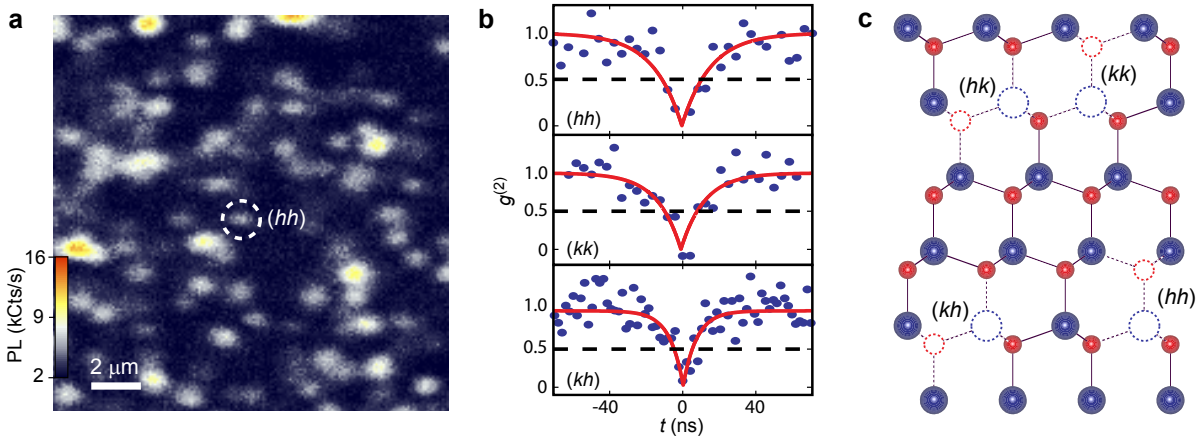

Figure 5.1: **a.** A 16 μm $\times$ 16 μm confocal PL image from a 4H-SiC membrane irradiated at 10^{13} cm^{-2} fluence. Confocal PL is collected at a depth of 20 μm into the membrane, and the sample temperature is held at 20 K. The PL spots are almost all identified as divacancies, but not all spots are isolated single defects. **b.** $g^{(2)}(t)$ measurements for single defects of the (hh) (circled in Fig. 5.1a), (kk), and (kh) divacancy forms. The $g^{(2)}$ curves (blue dots) show strong antibunching, clearly achieving the $g^{(2)}(t=0) < 0.5$ threshold for single optical emitters. The red curves are fits to a simple two-level model (details presented in the Appendix C). **c.** Divacancies in 4H-SiC consist of neighboring Si and C vacancies. Because either the h or k lattice site can be vacant, there are four inequivalent forms of divacancy in 4H-SiC.

ular focus of such research, the neutral divacancy in SiC has a spin-triplet electronic ground state[13, 224] that can be polarized and read out with ODMR[129, 86, 72, 39, 9, 40].

In contrast to NV centers in diamond, which are addressable at visible wavelengths, divacancies in SiC are addressable in the near infrared[224, 9], making their applicability to photonics and communication particularly strong. However, ODMR has previously only been used in SiC to measure spin ensembles, not individual electronic spin states. Here, by showing that neutral divacancies in SiC are both highly coherent and individually addressable, our results open up new avenues for engineering high-performance electronic devices incorporating single-spin sensors and memories.

5.2 Sample preparation for isolating single divacancy spins

Achieving single-center addressability with ODMR requires a nearly defect-free substrate, such that multiple defects do not occupy a diffraction-limited confocal volume. Towards this end, we use hot-wall chemical vapor deposition to grow a 120-micron-thick single-crystal epitaxial film on an n-type 4H-SiC substrate[103]. This growth technique can be used to create commercial quality, multilayer electronic structures at the wafer scale. Our epilayer is optimized to have no basal plane dislocations or polytype inclusions, and in addition, a very low ($5 \times 10^{13}\,\mathrm{cm}^{-3}$) unintentional dopant density. After mechanically separating the epilayer from the substrate, we polish and dice it, and then irradiate the diced samples with 2 MeV electrons at a range of fluences ($5 \times 10^{12}\,\mathrm{cm}^{-2}$ to $1 \times 10^{15}\,\mathrm{cm}^{-2}$) in order to create Si and C vacancies. Finally, we anneal the samples to activate vacancy migration and form divacancies[72, 40].

5.3 Photoluminescence imaging and measurement of second-order coherence of emitted photons

To measure the photoluminescence (PL) from single divacancies, we integrate a high quantum-efficiency superconducting nanowire single photon detector into a home-built confocal microscopy setup that uses a 975 nm continuous-wave excitation laser. With the sample cooled to 20 K, we observe distinct bright spots (3-5 kcounts/s) in a scanning PL image (Fig. 5.1a). We then use Hanbury-Brown Twiss interferometry to measure the second-order intensity correlation function ($g^{(2)}$) of the emission from several of these spots, all of which display photon anti-bunching behavior to varying degrees. The three divacancies presented in the main text of this work exhibit $g^{(2)}(t = 0) < 0.5$, where t is the time delay between successive photons, indicating that they are single quantum emitters (Fig. 5.1b). The characteristic times of the $g^{(2)}(t)$ dips range from 9 to 12 ns, slightly less than the neutral divacancies (14 ± 3 ns) optical lifetimes[72], as expected from an optically pumped emitter.

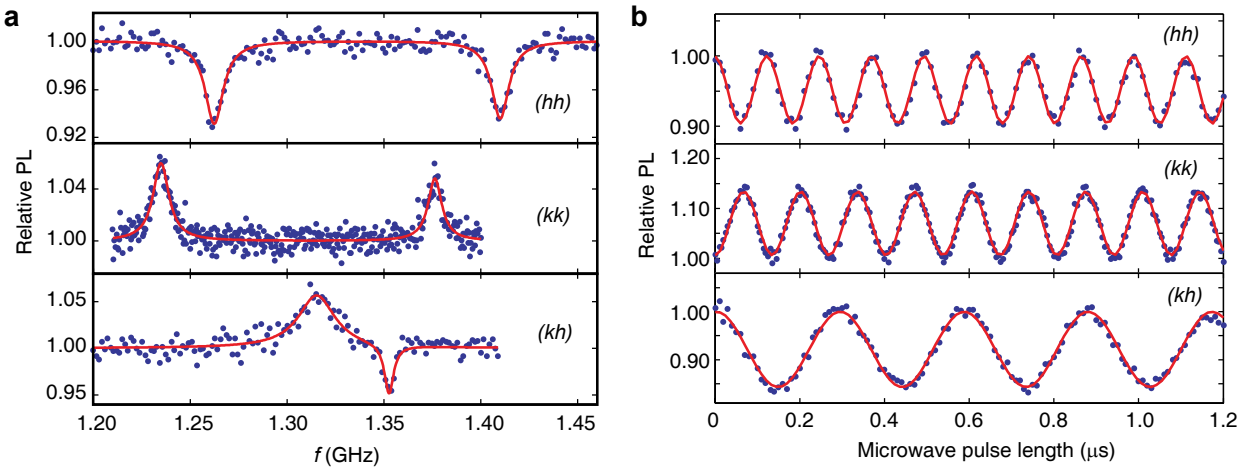

Figure 5.2: **a.** Measurements of continuous-wave ODMR (blue dots) of the single divacancies from Fig. 5.1. The measured (hh) divacancy is circled in Fig. 5.1a. For the measurements on the (hh) and (kk) divacancies, a c-axis oriented magnetic field of $B = 50\,\mathrm{G}$ is applied to lift the $m_s = \pm 1$ degeneracy at $B = 0$. For the (kh) divacancy, no external B is applied. The sample temperature is 20 K. The relative PL is the fractional change in PL arising from microwave irradiation. The background PL is subtracted before computing the relative PL. The three curves are vertically offset, for clarity, and the red curves are fits to Lorentzians. **b.** Rabi oscillations (blue dots) of the three divacancies measured in Fig. 5.2a, demonstrating coherent control of single electron spins in SiC. The fits (red curves) are to single sinusoids.

Because there are two inequivalent lattice sites for C and Si atoms in 4H-SiC, namely the hexagonal (h) and quasi-cubic (k) sites, four inequivalent neutral divacancies can exist. The three we have isolated and identified in the present work are the (hh), (kk), and (kh) divacancy forms (Fig. 5.1c). We have observed the (hk) form in previous ensemble studies of other 4H-SiC wafers[129, 72, 73], but neither ensemble PL spectroscopy (see Appendix C) nor confocal PL measurements show this form in the substrates prepared for this study.

5.4 Coherent control of single divacancy spins

We measure single-spin, continuous-wave ODMR spectra by sweeping the frequency (f) of an applied microwave driving field and measuring the change in PL from individual divacancies (Fig. 5.2a). Spin-selective transitions cause the emitted PL intensity to depend on the divacancys spin-sublevel occupation[129, 86, 72]. Therefore, the PL intensity has a peak or

a dip when f is resonant with a spin transition.

Each inequivalent divacancy is addressable at characteristic spin-resonance frequencies. For the c-axis-oriented (hh) and (kk) divacancies, we measure ODMR with an applied c-axis oriented magnetic field (B) to lift the degeneracy of the $m_s = \pm 1$ spin transitions. For the (kh) defect, we measure ODMR at $B = 0$, because the crystal field already splits the degeneracy between all three spin sublevels of the basal-plane-oriented defects. ODMR on an additional (kk) divacancy that is hyperfine coupled to a nearby ^{29}Si nucleus is shown in Appendix C.

In addition to continuous-wave ODMR measurements, we use pulsed ODMR to quantify the SiC divacancies coherence times and spin visibility, defined as the fractional change in PL when a spin is flipped. We observe coherent Rabi oscillations of the single divacancies by applying variable-length bursts of resonant microwaves between short initialization and readout laser pulses (Fig. 5.2b). These oscillations are the simplest demonstration of coherent control of the spin within a two-level subspace of its spin-1 ground state. From these measurements, we infer that single divacancies have an ODMR visibility of 9 to 15 percent. Although this visibly is roughly half that of NV centers in diamond, resonant excitation techniques may be applied in the future to significantly enhance it (see Chapter 6).

5.5 Observation of long Hahn echo coherence times

Long spin-dephasing timescales are critical to both quantum information and sensing applications of isolated solid-state spins. To measure the inhomogeneous spin dephasing time (T_2^*), we apply Ramsey pulse sequences to the isolated divacancies (Fig. 5.3a). For the (hh) and (kh) forms, the multi-frequency oscillations observed in the Ramsey signal (0.5-1.5 MHz) as a function of free precession time (t_{free}) are due to a weak hyperfine interaction between the divacancy electron spin and a nearby nuclear spin. As a consequence of the better homogeneity of single spins over ensembles, the fitted T_2^* times, which range from 1.1 to 4.4 μs, are significantly longer than those previously measured in ensembles[129]. To measure the

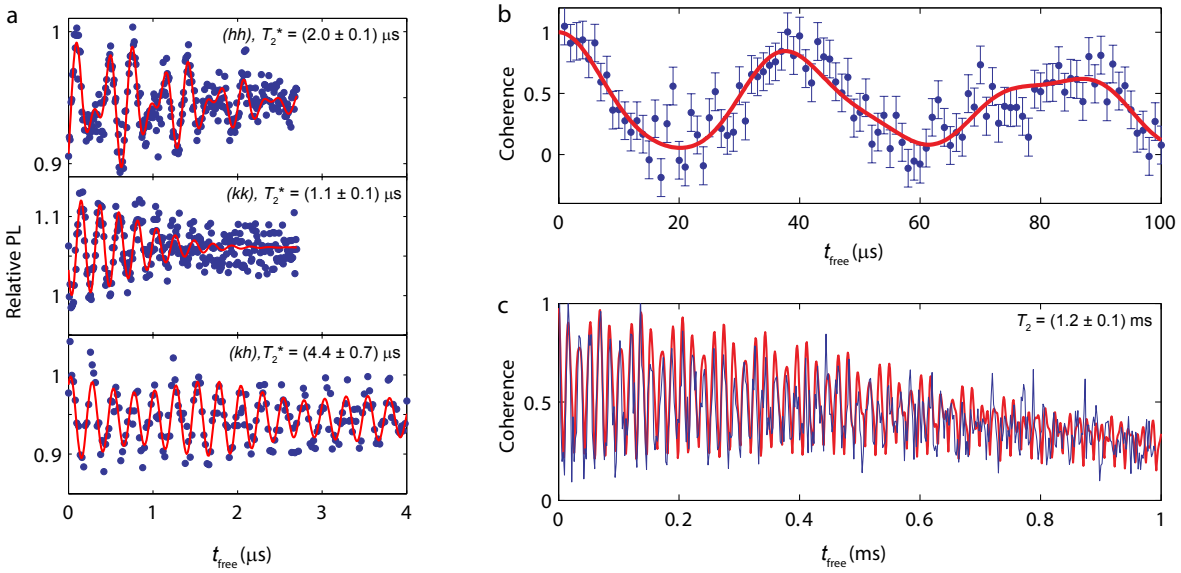

Figure 5.3: **a.** Measurements of Ramsey spin coherence of single divacancies (blue dots) at 20 K, along with a fit to an ESEEM model (red line, see Appendix C). The fits are Gaussian decaying exponentials (with characteristic decay time T_2^*), accounting for dephasing, multiplied by sinusoids. The oscillations are due to the 4 MHz microwave detuning we used for the measurement, and the beating in the (hh) and (kh) measurements indicates weak $(0.5 - 1.5\,\text{MHz})$ hyperfine coupling to nearby nuclei. **b.** A measurement of Hahn-echo spin coherence of a single (kk) divacancy at $B = 116\,\text{G}$ (blue dots). The ESEEM oscillations are due to periodic spin dephasing from the bath of naturally abundant, spin-1/2 ^{29}Si and ^{13}C nuclei, which are precessing at their Larmor frequencies. A single-spin ESEEM model (red curve, see Appendix C) of sinusoids at these frequencies that assumes no decay (since T_2 is much longer than 100 μs) accurately reproduces the data we observe. **c.** A measurement (blue curve) of the Hahn-echo spin coherence of a (kk)-divacancy ensemble at $T = 20\,\text{K}$ and $B = 134.1\,\text{G}$, from the 4H-SiC membrane irradiated at the highest fluence of $10^{15}\,\text{cm}^{-2}$. The fit (red curve) is to an ESEEM model (see Appendix C) based on the Larmor precession of the ^{29}Si and ^{13}C nuclei and a general compressed exponential decoherence function of the form $e^{-(t_{\text{free}}/T_2)^n}$, where T_2 and n are free parameters. The fit yields $T_2 = (1.2 \pm 0.1)\,\text{ms}$ and $n = (2.0 \pm 0.3)$. Interference effects cause the amplitude of the ESEEM oscillations to decay more quickly than the overall coherence.

homogeneous spin coherence time (T_2) of the isolated divacancies, we apply standard Hahn echo sequences to refocus the spin coherence. We observe collapses and revivals of the coherence of a single (kk) divacancy as a function of t_{free} (Fig. 5.3b), an effect known as electron spin echo envelope modulation (ESEEM)[184]. The ESEEM oscillations originate from periodic spin dephasing and rephasing due to the Larmor precession of naturally abundant, spin-1/2 ^{29}Si and ^{13}C nuclei in the sample. The apparent decay of coherence in Fig. 5.3b is actually due to beating between these precessional frequencies – at later free evolution times, the coherence will rephase. However, limitations to the PL collection efficiency of our present apparatus (see Methods for explanation) make it practical only to measure single-spin Hahn-echo signals out to approximately $t_{\text{free}} = 100\,\mu$s, which is shorter than the T_2 time of 4H-SiC divacancies[72]. In order to obtain a lower bound for the average single-spin T_2 time in our samples, we applied the same Hahn-echo sequence to an ensemble of (kk) divacancies. We fit the ensemble coherence data to a general ESEEM/decoherence model (see Appendix C) to find that $T_2 = (1.2 \pm 0.1)\,$ms. This T_2 time is significantly longer than the $360\,\mu$s T_2 time previously reported for divacancies in SiC[72].

Notably, although ^{29}Si is more abundant than ^{13}C, (4.7% vs. 1.1% natural abundance), this T_2 time is twice as long as the highest reported ($600\,\mu$s) T_2 time measured for NV centers in chemically but not isotopically purified diamond[227], where the nuclear bath comprises ^{13}C nuclei only. We do not completely understand the origin of these high T_2 times. However, one factor underlying them may be that the ^{29}Si and ^{13}C nuclei form separate spin baths that do not resonantly interact with each other. We expect isotopic purification and dynamical decoupling sequences to extend T_2 times in SiC even further.

5.6 Conclusions

Incorporating highly coherent single electron spins into high-performance SiC devices should provide many new opportunities for advancing quantum control. The present experiments isolating divacancies and a subsequent complementary work reporting the isolation of sili-

con vacancies in SiC are key advances towards leveraging the atom-like properties of defects within a mature materials platform[248]. In the future, spin-photon entanglement in SiC could offer a promising route towards quantum-repeater networks, facilitated by the divacancy emission near telecom wavelengths. Moreover, spins embedded into SiC transistors could lead to electrically gated spin-spin coupling via charge-state manipulation, while spins within high-Q SiC micromechanical resonators could be a platform for studying spin-phonon interactions. Just as the performance of commercial SiC electronics has been improved by a greater understanding of defect science, future avenues for defect-based quantum technologies may be driven by SiC devices.

CHAPTER 6

RESONANT ADDRESSING OF SINGLE DIVACANCIES IN 3C AND 4H SILICON CARBIDE

This chapter is an early draft of a manuscript in preparation that contains some preliminary results, "Resonant addressing of single divacancies in 3C and 4H silicon carbide," D. J. Christle, P. V. Klimov, C. F. de las Casas, K. Szász, V. Ivády, V. Jokubavicius, W. F. Koehl, T. Ohshima, N. T. Son, E. Janzèn, A. Gali, and D. D. Awschalom, in preparation (2016)

In this chapter, we demonstrate the isolation, identification, and control of single divacancy defects in 3C-SiC, and report a T_2 spin coherence time of approximately $900\,\mu$s at $T = 20\,$K. A model of the 3C-SiC divacancy's intersystem crossing and spin polarization dynamics is presented that agrees with our separate time-resolved and spin-resolved photoluminescence experiments from which we infer a ground state spin polarization efficiency of $95^{+5}_{-8}\%$. We also report the experimental determination of the optical fine structure of the divacancy in 3C-SiC and the (hh) and (kk) forms of divacancy in 4H-SiC via manipulation with a narrow-line resonant laser. We show resonant manipulation can achieve at least 94% readout contrast in the 4H polytype, and further that each defect species studied appears to have an optical fine structure similar to the nitrogen vacancy center in diamond with low linewidths and a good optical cycling transition for high-fidelity initialization and readout. Our work demonstrates that divacancies in SiC possess the major ingredients of long coherence times, high polarization, and favorable optical transitions that are necessary for photon-based entanglement over long distances via optical fiber.

6.1 Motivations

Silicon carbide (SiC) has generated recent interest because it is host to a family of divacancy-related point defects whose spins can be coherently controlled with long coherence times, with certain defects having functionality that persists to room temperature. Silicon carbide is an excellent host material for defect physics because it can be grown commercially at the wafer scale and has an already established literature describing a number of high quality MEMS microstructures and high-Q photonic crystals that have been microfabricated in it. It occurs in over 200 different structural configurations, called polytypes, and the three most common are called the 3C, 4H, and 6H polytypes. Each of these possesses divacancies or defects with very similar spin and photophysics, and within a relatively short period of time, these defects have already demonstrated promise for nanoscale sensing and quantum information applications[129, 72, 73, 125, 126].

Because divacancies emit near the telecom wavelengths, one of the primary motivations for studying them is for spin-photon coupling applications. Whether the materials quality and low-temperature physics will support both a narrow linewidth optical fine structure and a long-lived cycling transition are open questions. These ingredients have been absolutely key in spin-photon entanglement, high-fidelity readout, and teleportation between distant spins achived in the nitrogen vacancy center defect in diamond[235, 35, 204, 23, 187], so rapidly identifying whether new defects like the divacancy possess a clear spin-photon interface is of prime importance. From a more basic standpoint, questions about the physics that drive these defects' optical polarization and readout mechanisms also remain unanswered, even though these processes play a pivotal role in almost every application.

The present work centers on studying divacancies in the common polytype most-studied for defect spin applications, 4H-SiC, and a defect in the least-studied common polytype and most similar to diamond, 3C-SiC. The defect in 3C-SiC is called 'Ky5' because its identity has not been definitively established. Reports on this defect are only in ensembles, so our first focus will be on isolating and coherently controlling this defect. We will then conclusively

identify it by comparing experiment to *ab initio* theory, establish a complete working model of its spin & orbital dynamics, and finally resonantly manipulate both 4H-SiC divacancies and 3C-SiC Ky5 defects at the single spin level to reveal their excited state level structures and dynamics.

The 3C-SiC polytype has been the subject of intense research for semiconductor device purposes in part because it can be grown cost-effectively as an epitaxial layer on silicon at the 6-inch scale[177, 26, 209]. Growing an epilayer to form a heterogeneous substrate makes it significantly easier to microfabricate high-quality free-standing layers that can be used in micromechanical or photonic devices, with several examples, including photonic nanobeams with an estimated Purcell factor in the 10^4 range, already present in the literature[138, 226, 144, 38, 190, 151, 36, 191, 152]. The coupling of a quantum mechanical spin to mechanical or optical degrees of freedom have been active areas of research in diamond for some time[76, 77, 154], but transcribing this research to take advantage of the significant MEMS and optomechanics activity in 3C-SiC cannot occur without finding a suitable optically active spin system. The Ky5 defect was originally observed as infrared photoluminescence in electron irradiated 3C-SiC[221] and later revealed in electron paramagnetic resonance spectra to have a spin-1 ground state[31]. Recent research shows that large ensembles of Ky5 defects can be coherently controlled and read out using optically detected magnetic resonance, with T_2 coherence times of about $24\,\mu$s[72].

6.2 Isolation of single spins in 3C-SiC with long coherence times

The 3C-SiC samples we use in this study single domain 3C-SiC crystal, we use a recently developed two-step growth process that first nucleates small domains of single crystal 3C-SiC on an off-oriented 4H-SiC substrate and uses a lateral enlargement process to yield a $\approx 1\,$mm thick 3C-SiC layer[119]. The layer is unintentionally doped n-type, with a nitrogen concentration of $10^{15} - 10^{16}\,\mathrm{cm}^{-3}$, and its surface is perpendicular to the $< 111 >$ direction. The 3C-SiC layer is mechanically separated and mechanically polished on both sides to

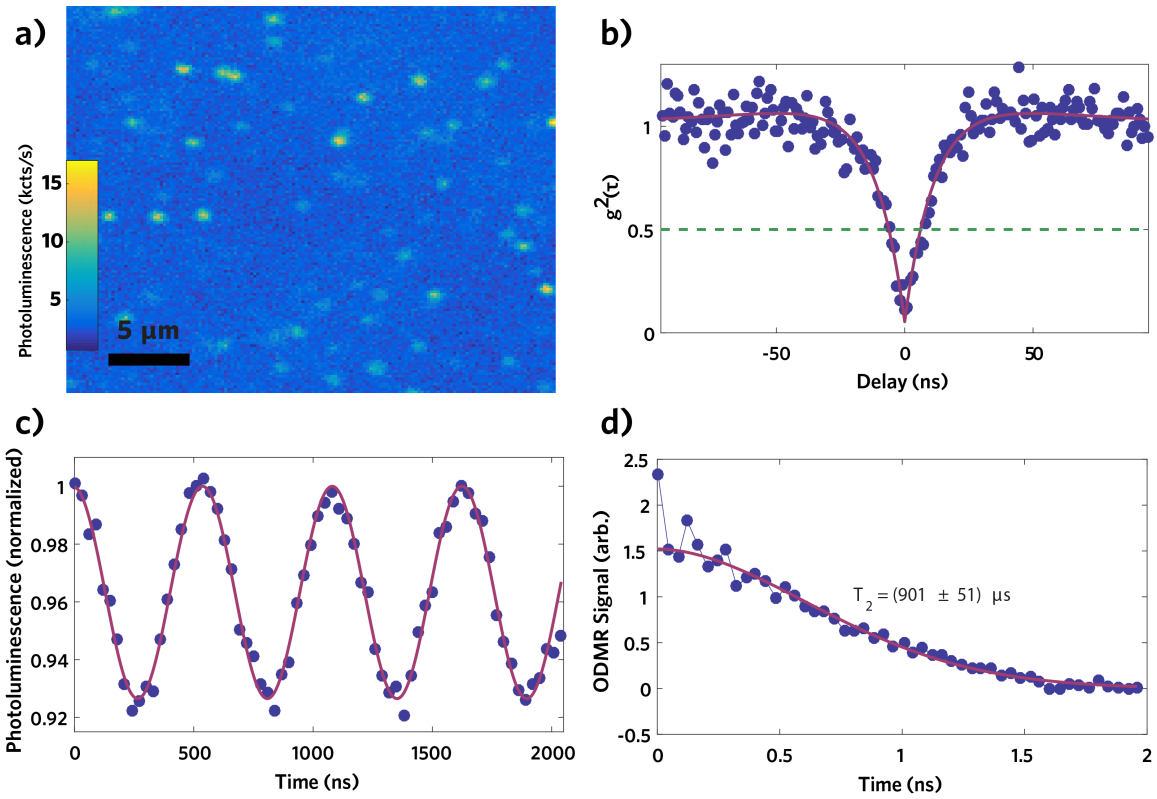

Figure 6.1: (a) A two-dimensional photoluminescence scan showing single defects in 3C-SiC. (b) Photon anti-bunching observed in the photon correlation data on the spot in the center of Fig.6.1a. (c) Rabi oscillations taken on a single divacancy. (d) Hahn echo measurement performed on an ensemble of divacancy defects in a second sample.

leave a 730 μm, light-yellow colored layer, which we then irradiate with 2 MeV electrons at a fluence of $5 \times 10^{12}\,\mathrm{cm}^{-2}$ and anneal at 750° C. We lithographically pattern a Ti/Au loop antenna (10/200 nm thickness) on the surface and cool the sample to $T = 20\,\mathrm{K}$ in a helium flow cryostat that resides within a homebuilt scanning confocal microscopy apparatus. This apparatus uses a 980 nm laser for off-resonant excitation and a set of optical filters to collect the red-shifted photoluminescence above 1064 nm and record it using a two-channel superconducting nanowire detector system with approximately 80% quantum efficiency across the near infrared. A two-dimensional photoluminescence spatial scan is shown in Fig. 6.1a that displays isolated spots of photoluminescence with intensities of $8 - 16\,\mathrm{kcts/s}$. Two channels of our detected are used in a Hanbury-Brown and Twiss configuration while centered

on the circled spot to observe photon antibunching, shown in Fig. 6.1b, unambiguously confirming the luminescence we see originates from a single quantum emitter. The emitters show optically detected magnetic resonance at $D = 1.338\,\mathrm{GHz}$ and photoluminescence at 1106 nm, consistent with previous ensemble observations of the Ky5 defect[221, 31, 72]. Fig. 6.1c shows single spin Rabi oscillations that demonstrate the defect can be off-resonantly initialized, manipulated with microwaves, and read out with approximately 7.5% contrast. Using a Ramsey interferometry experiment, we also measured the inhomogeneous spin coherence time to be $T_2^* = 1.8\,\mu\mathrm{s}$. These results are similar to the $9 - 15\%$ contrasts and $1 - 4\,\mu\mathrm{s}$ T_2^* times obtained using the same techniques on neutral divacancies in 4H-SiC[46] and are encouraging for DC-based sensing schemes based on measuring resonance level shifts in defects[166, 236, 237]. Dynamical decoupling can extend the effective coherence time of defects by periodically applying pulses to rephase the spin coherence. Because we expect the coherence time to be long, we prepare a separate 3C-SiC sample identically to the first but with a higher irradiation fluence of $1 \times 10^{15}\,\mathrm{cm}^{-2}$ to produce a much higher defect density. The larger defect density produces significantly higher signal levels, which allows us to measure coherences are much longer delays than are practical on a single defect. Applying a Hahn echo sequence to an ensemble of defects in this sample (Fig. 6.1d) revealed $T_2 = 0.9\,\mathrm{ms}$ at $T = 20\,\mathrm{K}$ and $B = 300\,\mathrm{G}$. This coherence time is longer than the longest reported coherence times of 0.6 ms in non-isotopically purified diamond NV center ensembles[227] and almost as high as the 1.2 ms Hahn echo coherence time reported for neutral divacancies in non-isotopically purified 4H-SiC[46].

6.3 Identification of the Ky5 defect as the neutral divacancy in 3C-SiC

Density functional theory is a powerful first-principles computational technique that can accurately predict a defect's hyperfine tensors that define its coupling to nearby nuclei[230].

The T_2^* times we observe are long enough to obtain high resolution of spin resonances caused by hyperfine coupling to nearby ^{13}C and ^{29}Si nuclei and thus provide a route to definitive identification. To calculate the hyperfine tensors, we employ density functional theory simulation of the neutral divacancy in 3C-SiC implemented in VASP[133, 134]. Experimentally, we isolate a Ky5 defect coupled to a nearest-neighbor ^{13}C and another coupled to a second nearest-neighbor ^{29}Si and perform both continuous wave and pulsed electron spin resonance measurements on each. Strong coupling of a nuclear spin splits the two spin-1 magnetic resonances into two doublets, with each doublet representing the same electronic spin transition but either a spin up or spin down nuclear spin transition. Because the ground state zero-field magnetic splitting is about 1.3 GHz but the hyperfine couplings are only on the order of $10 - 100$ MHz, the doublet splittings will not change significantly when the applied magnetic field, B, is small. The strongest changes in the spin resonance splittings will occur at a level anticrossing when the hyperfine couplings are on the order of the electronic spin splittings, but our microwave amplifier has a minimum required frequency of 700 MHz. We therefore restrict our measurements to the range $B = 10 - 250$ G and take several of them at large angles ($30 - 80°$) to the defect axis. We apply a Bayesian approach to tomographically reconstruct the corresponding hyperfine tensors parameterized in terms of the principal components $A_x x \approx A_y y$ and $A_z z$, and the angle θ from the tensor's principal axis. Our theoretical computations and tomographic reconstructions are presented in Table 6.1. The agreement is excellent for both measured tensors, though our analysis indicates our technique's uncertainty is still a few MHz, so the ^{13}C data inferred from a single spin are the most compelling. We extract the We also find accurate agreement of both ^{29}Si tensors with the electron spin echo envelope modulation (ESEEM) frequencies we observe in the ensemble Hahn echo measurement described previously. Furthermore, we predict the 3C-SiC neutral divacancy's ground state zero field splitting to be $D = 1.345$ GHz, in good agreement with our experimental value $D = 1.336$ GHz. The preponderance of our results conclusively identify the Ky5 defect as the neutral divacancy in 3C-SiC.

Atoms	A_{xx}	A_{yy}	A_{zz}	θ	A_z
^{13}C (th)	51.3	52.0	122.2	72.6	61.0
^{13}C (exp)	(49.5 ± 4.3)	(49.5 ± 4.3)	(108.5 ± 3.6)	(72.3 ± 4.3)	(57.6 ± 1.3)
$^{29}\mathrm{Si}_{6\mathrm{x}}$ (th)	9.1	9.9	7.7	68.5	8.9
$^{29}\mathrm{Si}_{6\mathrm{x}}$ (exp)	(8.7 ± 1.0)	(8.7 ± 1.0)	(9.6 ± 1.0)	(47 ± 34)	(9.1 ± 0.2)
$^{29}\mathrm{Si}_{3\mathrm{x}}$ (th)	11.4	11.4	11.8	50.1	11.6
$^{29}\mathrm{Si}_{3\mathrm{x}}$ (exp)	...	...	...	...	(12.4 ± 0.3)

Table 6.1: Theoretical and experimental reconstructions of ^{13}C and ^{29}Si hyperfine tensors. The coupling strengths are given in units of MHz and the angles are given in degrees. The uncertainties on the experimental values are 95% probability intervals. The $^{29}\mathrm{Si}_{3\mathrm{x}}$ tensor was not measured in the single spin measurements, but the projection A_z in the table is estimated from a short-duration ensemble ESEEM measurement. The ensemble ESEEM measurement gave $A_z = (9.1 \pm 0.6)\,\mathrm{MHz}$ for the $^{29}\mathrm{Si}_{6\mathrm{x}}$ line, in agreement with the value in the table based on the single spin measurements.

6.4 Dynamical model of the 3C-SiC divacancy optical cycle

The special optical cycle that initializes and reads out the divacancy's spin state is a defining quality that makes them appealing for quantum information applications[247], yet these dynamical processes have not been rigorously characterized yet in divacancies in any silicon carbide polytype[72, 37]. We aim here to establish a consistent model of the 3C-SiC divacancy's effective orbital structure and spin-dependent transition rates by using time-correlated photon counting techniques on single defects. The same molecular model studied in previous *ab initio* computations of the 4H neutral divacancy can be adopted in the 3C polytype. In this picture, the six dangling bonds from neighboring Si and C atoms are split by C_{3v} symmetry considerations two non-degenerate a_1 states, a pair of degenerate e states at a higher energy, and another pair of degenerate e states at even higher energy[89, 86]. These single-particle states are filled with six electrons according to Hund's rules, which gives a total electronic ground state triplet $^3A_2$ ($a_1^2 a_1^2 e^2$) and a triplet excited state ^3E ($a_1^2 a_1^1 e^3$), where a triplet-to-triplet optical transition between these states is allowed and the model agrees with experimental observations that the ground state is a spin triplet[86, 13, 31, 224, 72].

A level diagram of the five-level model we propose that is consistent with our measure-

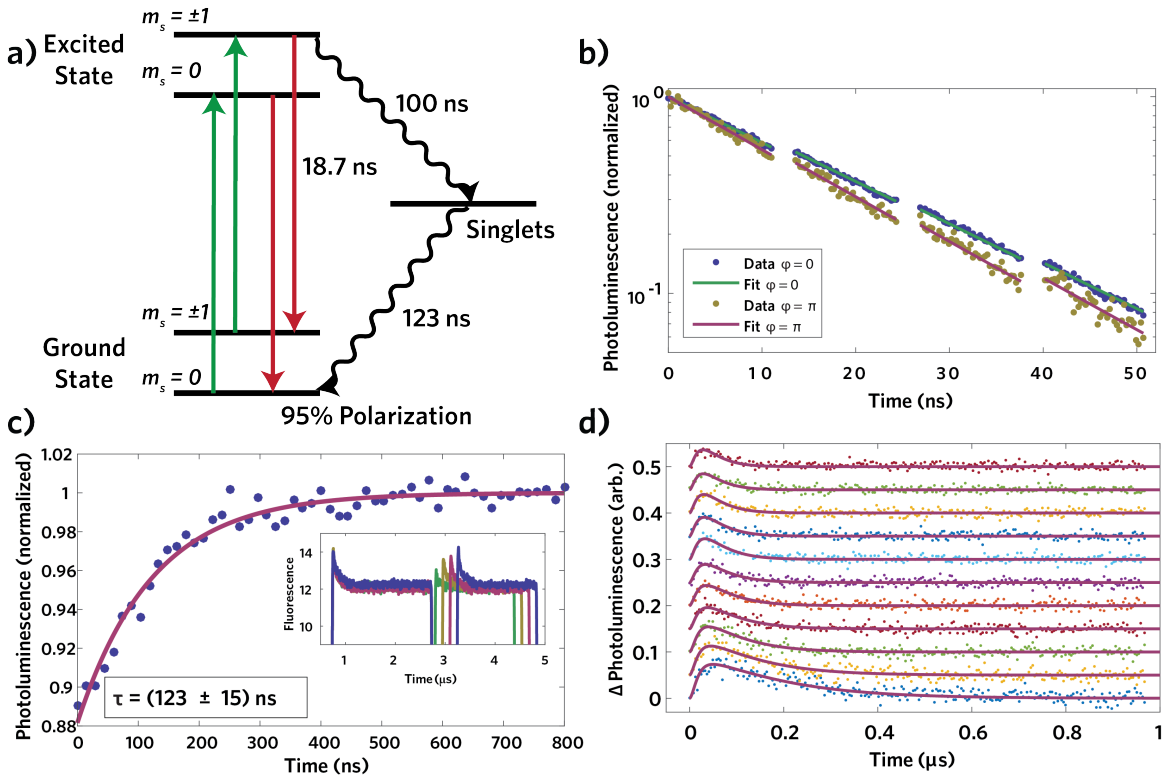

Figure 6.2: (a) Five level model with a triplet GS, triplet ES, and 5th effective level that represents the proposed spin singlet states. The lifetimes of each allowed transition are shown, along with the estimated ground state spin polarization. (b) Recovery time measured in the delay sweep of two optical pulses experiment, showing a time constant of (123 ± 15) ns. Inset: Selected normalized TCSPC datasets at various delays, showing the recovery in amplitude of the second optical pulse as the delay increases. (c) Normalized log plot of the spin-resolved biexponential lifetime experiment, showing the case where no microwaves are applied and the case when a microwave π-pulse is applied to one of the ± 1 transitions in the ground state. The small gaps are small pulses that appear from the imperfect extinction of our electro optic modulator. These extra pulses are incorporated into the model but the pulse onset is removed to avoid having to convolute the theoretical curve with the exact pulse shape. (d) Power-dependent differential photoluminescence recorded between a divacancy prepared in the $m_s = 0$ state versus the $m_s = \pm 1$ state. Solid lines are the output of the global fit of the photoluminescence dynamics.

ments and assumptions is shown in Fig. 6.2a. In it we approximate the ground and excited state each with just two levels, $m_s = 0$ and $m_s = \pm 1$, while relaxation through any singlet states is represented by a single effective level. The dynamics are governed by first-order rate equations between levels, and we assume only the $m_s = \pm 1$ excited state level couples to the singlet level and that it relaxes to $m_s = 0$ in the ground state. The purpose of the model is to accurately reproduce the divacancy's spin and orbital dynamics, and the following experiments occur in regimes that probe only specific rates of the system.

To probe the triplet-triplet optical transition, we start by applying a small $B = 7\,\mathrm{G}$ magnetic field to a single divacancy at $T = 20\,\mathrm{K}$ that splits its $m_s = \pm 1$ spin sublevel degeneracy and allows us to address only a single spin transition. We use an experimental pulse sequence that applies a $1\,\mu\mathrm{s}$ 980 nm CW optical pulse to polarize the ground state, waits a delay of $1\,\mu\mathrm{s}$ for any orbital relaxation to occur, applies a microwave pulse to the $m_s = 0 \leftrightarrow -1$ transition, and finally applies a short $\approx 1\,\mathrm{ps}$ optical pulse from a mode-locked Ti:Sapphire laser tuned to emit near 920 nm[203]. The luminescence follows a biexponential decay, and the amplitudes of the exponentials follow the rotation of the spin state. Fig. 6.2b shows the data for comparison of the case where no microwaves are applied and when a π-pulse is applied, as well as fits inferred from a global Bayesian analysis performed on both datasets[236]. We interpret the longer lifetime of $\tau_0 = (18.65 \pm 0.33)\,\mathrm{ns}$ as the purely optical decay from the excited state back to the ground state, and the shorter lifetime, $\tau_{\pm 1} = (15.74 \pm 0.34)\,\mathrm{ns}$, as the result of a mixture of optical decay and non-radiative phonon-assisted intersystem crossing to the two $a_1^2 a_1^2 e^2$ singlets also predicted from the molecular model. Like the NV center in diamond, a transverse spin-orbit interaction likely links the ^3E state to states of different electronic and spin configurations[158, 167, 62] and is the spin-selective transition primarily responsible for the divacancy's special polarization and readout cycle. Our analysis infers an intersystem crossing rate of $(9.9 \pm 1.8)\,\mathrm{MHz}$ from the excited state, and a ground state spin polarization of $p_{m_s=0}/(p_{m_s=0} + p_{m_s=\pm 1}) = 95^{+5}_{-8}\,\%$. The off-resonant polarization inferred appears to be significantly higher than the 82% observed in diamond NV

centers, but the intersystem crossing rate is about 7x slower and this is a likely explanation of why the off-resonant readout contrasts observed in 4H and now 3C divacancies are less than the NV center[203, 46]. To probe the relaxation rate of the singlet states, we perform a second experiment, shown in Fig. 6.2c, that time resolves the divacancy photoluminescence subject to two 1.6 μs optical pulses separated by a delay t. The initial optical pulse produces an emission intensity that has a sharp maximum followed by an equilibration to a lower level on the order of a few hundred nanoseconds. The second optical pulse displays a reduced intensity for short delays, and we fit a single exponential to the first 20 ns of integrated photoluminescence versus delay to extract a recovery time of $\tau = (123 \pm 15)$ ns[161, 203]. While this recovery time is the sum of optical decay from the excited state and relaxation from the singlets, the optical decay measured in the previous experiment is much faster and therefore we can directly assign τ as the approximate relaxation rate from the singlets.

As a final check, we perform a third set of experiments, shown in Fig. 6.2d, that measure the full time-dependence of the photoluminescence emitted at the beginning of a CW optical pulse. The shape of the emitted photoluminescence curve depends on all of the systems rates as well as the excitation power used to drive the system. We apply two 2 μs long, 980 nm optical pulses separated by a 1.8 μs delay with either no microwaves applied or a π-pulse applied in the middle of the delay. This sequence gives ample time for the entire polarization cycle to occur and relax to the orbital ground state before the application of microwaves. The time-resolved photoluminescence of the second pulse is recorded for both sequences at eleven linearly spaced laser intensities between $150 - 1760\,\mu$W. These excitation strengths are chosen to cover a range about the excitation intensity that saturates the divacancy's emission (≈ 1.5 mW). The ± 1 data are subtracted from the 0 data at each power to give the differential photoluminescence between the two preparations versus power. The prediction derived from numerically simulating the five level model is globally fit to the complete set of data, with the relative laser pumping strengths constrained by the actual laser intensities independently measured by a power meter, and the orbital rates fixed to

the rates determined in our experiments. Fig. 6.2d shows the differential PL and the time-evolutions output from the global fit. The agreement is good, and we additionally find that while the shape of the differential photoluminescence is not particularly complicated, enough information is apparently present in these data to recover each of the rates of our five-level model simultaneously to reasonable accuracy without the prior information from the previous two experiments. Our model gives the first coherent understanding of the divacancy's polarization and readout cycle, which will serve as a point of comparison to divacancies and other point defects in each SiC polytype, and as foundation for more advanced experiments and future applications.

6.5 Resonant excitation of divacancies in 4H- and 3C-SiC

Given that divacancies in both the 4H and 3C polytypes of silicon carbide have now been isolated, we are now in a position to investigate and compare the fine structures of their excited states. The neutral divacancy molecular model predicts a ^3E excited state orbital doublet whose electronic structure has been derived previously from group theoretical considerations of the spin-orbit and spin-spin interactions as well as the effect of strain[167, 62]. Fig. 6.3a shows the effect on the excited state sublevels of the axial spin-orbit (λ_z) and spin-spin (D_{es}, Δ_1, Δ_2) interactions, along with the dominant spin compositions each sublevel at low transverse strain. At low strain, the E_x and E_y states retain a mostly $m_s = 0$ character, while the remaining states are a mixture of $m_s = \pm 1$ character. The effect of D_{es} and Δ_1 is to split certain sublevels as shown, but the effect of Δ_2 is to mix the E_1 / E_2 states with the E_x / E_y states, which is why this term is sometimes called the mixing term. Optical transitions from the ground state to excited state, shown schematically, are allowed when an excited state sublevel contains a non-negligible fraction of spin character in common with the originating level in the ground state. Here we use a combination of off-resonant laser excitation, a tunable narrow line laser, and microwave driving to reveal the structure of C_{3v}-symmetry divacancies in both 4H- and 3C-SiC via photoluminescence excitation (PLE)

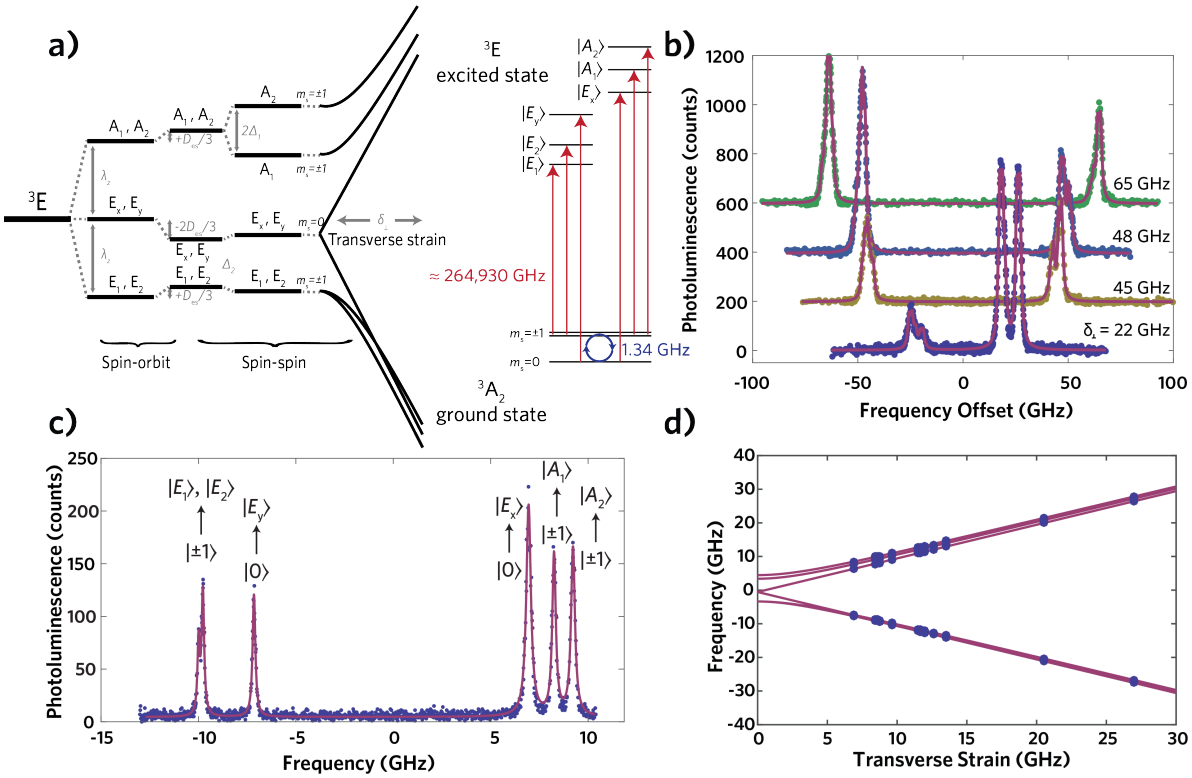

Figure 6.3: (a) Level diagram of the ^{3}E excited state, showing the effect of spin-orbit coupling, the spin-spin interaction, and transverse strain. The second diagram shows the laser excitation of transitions from the ground state to the strain-split excited state levels. (b) Photoluminescence excitation measurements taken without microwaves on single 3C-SiC divacancy defects at T = 8 K at different levels of strain $\delta_\perp$, showing rough agreement with the expected ^{3}E behaviour as a function of transverse strain. (c) Photoluminescence excitation measurements taken with the application of ground state microwaves on a single 4H-SiC (hh) divacancy at T = 8 K. The transitions are labelled according to their approximate state labels at zero strain. (d) Individual resonances recorded on separate (kk) divacancies at different strains at $T = 8$ K. The solid lines are a fit of the Hamiltonian to the observed resonances used to determine each Hamiltonian parameter, showing precise agreement with the model.

measurements[233, 18]. We prepare a sample of 4H-SiC from the same wafer used in previous single defect studies[46]. This material was grown as an epilayer on a 4H-SiC substrate using hot wall chemical vapor deposition and mechanically separated to produce a 120 μm layer of low-impurity single crystal 4H-SiC, and has a very low unintentional dopant density of $5 \times 10^{13}/\mathrm{cm}^{-3}$. Fig. 6.3c shows the photoluminescence recorded as we scan the laser frequency across the zero phonon line of a single 4H-SiC (kk) divacancy (265.26 THz) at $T = 8\,\mathrm{K}$ in a weak magnetic field of a few Gauss. In this measurement, we reset the spin state with an off-resonant laser pulse, give sufficient time for the singlets to relax, and count only photons emitted during a subsequent resonant laser pulse. It reveals two sharp peaks, corresponding to transitions from the $m_s = 0$ spin sublevel in the ground state to the two E_x and E_y states in the excited state. Because of the divacancy's strong polarization into the $m_s = 0$ state under off-resonant excitation, only the $m_s = 0 \leftrightarrow 0$ transitions are seen. The levels are split by a transverse strain, $\delta_\perp$, whose magnitude is about half the splitting between the states labeled E_x and E_y. The strain for each divacancy is random and is likely dependent on both the growth and any post-processing done to the sample, and the specific level structure and spin-mixing for a given strain can be determined by diagonalization of the Hamiltonian. A second trace in Fig. 6.3c shows the same result of the same measurement except one of the ± 1 transitions in the ground state is driven by continuous microwaves. The microwaves maintain a time-averaged population in a ground state spin sublevel with $m_s = \pm 1$ character, which allows us to observe the other four $m_s = \pm 1$ spin conserving transitions. We measure a set of both (hh) and (kk) divacancies with and without microwaves, and use a Bayesian analysis to infer the Hamiltonian's spin-orbit and spin-spin parameters from the observed peaks with errors quoted at the 95% probability level. For the (hh) divacancy, we determine $\lambda_z = (6.10 \pm 0.04)\,\mathrm{GHz}$, $D_{\mathrm{es}} = (0.85 \pm 0.01)\,\mathrm{GHz}$, $\Delta_1 = (0.59 \pm 0.01)\,\mathrm{GHz}$, and $\Delta_2 = (0.02^{+0.03}_{-0.02})\,\mathrm{GHz}$. For the same measurements across the zero phonon line of a set of (kk) divacancies near 264.93 THz and through the same analysis find $\lambda_z = (3.58 \pm 0.12)\,\mathrm{GHz}$, $D_{\mathrm{es}} = (0.87 \pm 0.04)\,\mathrm{GHz}$, $\Delta_1 = (0.55 \pm 0.04)\,\mathrm{GHz}$, and $\Delta_2 = (0.04^{+0.06}_{-0.04})\,\mathrm{GHz}$. The data

and fits displayed in Fig. 6.3d show excellent agreement, and the analysis demonstrates we can accurately infer all parameters in the Hamiltonian even without finding a defect at a particularly low value of transverse strain.

The excited state level structure of the divacancy in our 3C-SiC sample is more difficult to reveal. Fig. 6.3b shows several PLE measurements taken on different 3C-SiC divacancies at $T = 8\,\mathrm{K}$ across their zero phonon lines near 270.92 THz. The resonances observed are split into distinct orbital branches with strain and an apparent $\lambda_z \approx 13 - 17\,\mathrm{GHz}$, but we cannot label the transitions reliably, owing to the roughly 2 GHz linewidths seen in this sample. The modulation of the peak amplitudes by microwave driving in the ground state is also difficult to interpret clearly in our measurements. One technique used to reduce the optical linewidths of emitters in diamond is to omit the off-resonant laser used for repolarization of the spin and use resonant light only[117, 82]. The off-resonant laser has a shorter wavelength and is much more intense, which may allow it to cause spectral diffusion by redistributing nearby charges in the crystal, which would manifest in our measurement as an inhomogeneous broadening of the linewidth. In our sample, this technique gives only a modest reduction in linewidth to approximately 1.6 GHz, suggesting possible spectral diffusion is still faster than our per-point integration time (200 ms), and the observed PLE resonances again change only modestly with microwave driving. Early resonant excitation experiments in diamond also suffered from large linewidths ($\approx 30\,\mathrm{GHz}$) in type-Ib diamond, where the nitrogen impurity concentration is in the range of a few parts per million[117, 232]. Our 3C-SiC sample has an approximate nitrogen concentration of about $0.1 - 0.5\,\mathrm{ppm}$, so the similarity of divacancy physics between polytypes, the clarity of the results in the 4H polytype, and comparison to early reports in diamond suggest the minimization of nitrogen and other impurities are a promising approach for observing narrow linewidths in 3C-SiC divacancies.

Our narrowest linewidth of $(94 \pm 4)\,\mathrm{MHz}$ was observed on a (hh) divacancy at $T = 8\,\mathrm{K}$, and the typical linewidths measured on both (hh) and (kk) divacancies at the same temperature were in the range of 100-200 MHz. These are significantly lower than those we

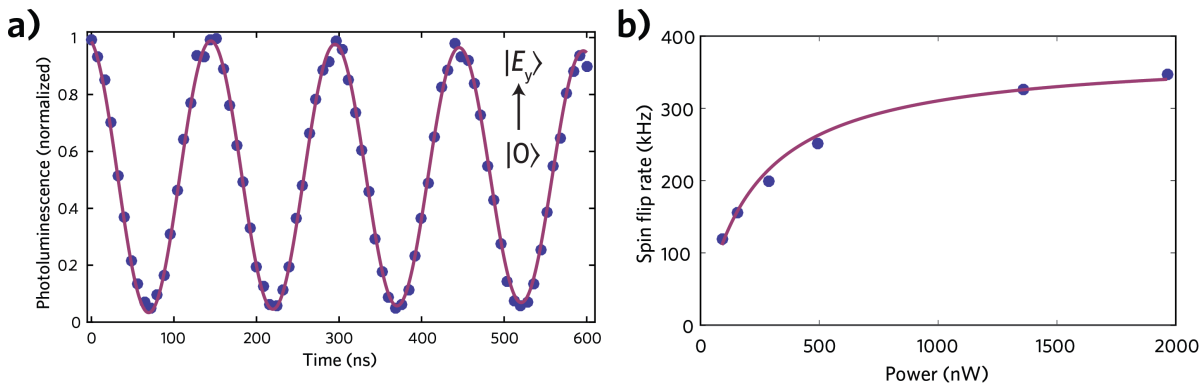

Figure 6.4: Single spin Rabi oscillations recorded using resonant readout on a (hh) divacancy at T = 8 K with a transverse strain of about 27 GHz. The measurement gives a background-corrected readout contrast of 94%, consistent with our expectation of high spin polarization and low spin mixing. (b) The estimated spin flip rate (inverse resonant photoluminescence decay rate) as a function of resonant laser power measured on a (kk) divacancy with a transverse strain of about 6.75 GHz.

observed in 3C-SiC, consistent with the lower estimated impurity levels ($\approx$ 1 ppb) in this sample, and within range of the 36-150 MHz linewidths reported in several state-of-the-art experimental demonstrations in diamond[235, 35, 22]. Towards the goal of achieving the theoretical 10 MHz lifetime-limited linewidth, future studies should focus on the connection between impurity levels and transition linewidth, as well as investigating the effect of more advanced annealing protocols[47]. We also generally do not observe obvious spectral jumps of a resonance between sweeps or ionization of the defects (e.g. the disappearance of a resonance between or during a sweep) in our experiments. This implies both a low ionization probability at experimentally relevant excitation strengths, which may materially improve the per-pulse-sequence success probability in future applications. Lastly, we demonstrate readout of the divacancy's spin using an $m_s = 0$ cycling transition and that these transitions can possess low rates of spin mixing. Fig. 6.4a shows a measurement of Rabi oscillations on an (hh) divacancy with a contrast of about 94%. This measurement proceeds similar to the measurement in Fig. 6.1c, where an off-resonant laser pulse initializes the spin and it is subsequently rotated using microwaves, but here the final readout step occurs by recording photons emitted when we apply a resonant laser tuned to the (hh) divacancy's E_x transition.

We established that off resonant light will polarize 3C divacancy to roughly 95%, so we expect a similarly high polarization here. Because of high spin polarization and because we select a defect with a strain that is away from an anticrossing ($\approx 27\,\mathrm{GHz}$), the contrast of the oscillations we record is substantially higher than readout using off-resonant laser light. Fig. 6.4b quantifies the spin-flip rate of the E_y transition as a function of power on a (kk) divacancy. This divacancy's strain is about 6.75 GHz, and was again chosen because this value should give a low degree of spin mixing in the excited state based on the Hamiltonian parameters inferred from our level structure measurements. A low rate of spin-flips allows more photons from a cycling transition to be emitted before mixing causes the spin to flip and the photon emission ceases. As the laser power is increased, the optical transitions spin-flip rate saturates at about 360 kHz, implying the number of photons emitted is within a factor of two of values used for high-fidelity readout of NV center spins in a single shot[204].

6.6 Conclusions

These experiments ultimately show the fundamental physics of neutral divacancies appears promising for applications that benefit from a qubit with long coherence times and a clear spin-photon interface in a favorable materials platform. We extended previous single-divacancy studies in 4H-SiC to the important 3C polytype, confirmed the 3C-SiC divacancy's identity by comparison with our first-principles calculations, and quantitatively explained the divacancy's orbital and spin dynamics that are responsible for its special optical addressability. Our resonant laser experiments significantly advanced the understanding of the divacancy's excited state fine structure in both polytypes and set lower bounds on figures of merit for long-distance entanglement competitive with the state-of-the-art for deep-level defects.

APPENDIX A

MEASUREMENT AND CONTROL OF SINGLE SPINS IN DIAMOND ABOVE 600 K – DETAILS

A.1 Methods and supplementary data

A.1.1 Sample fabrication

The sample used in this work was a 4 mm x 4 mm x 0.5 mm (100) Electronic Grade CVD diamond from Element Six. The sample was irradiated with $2 \times 10^{14}/\text{cm}^2$, 2 MeV electrons and annealed at 800° C in forming gas to increase the nitrogen-vacancy (NV) center density. The solid immersion lenses were etched using a Ga^+ focused ion beam system (FEI Helios 600) at an accelerating voltage of 30 kV and an etch current of 2.8 nA. To reduce charging, the sample was coated with 10 nm of sputtered Au/Pd. The alignment of the etch was done in two stages using a metallic alignment grid for rough alignment and four dots etched using the Ga^+ beam for finer alignment and further compensation of drift from charging effects during the milling of the final lens structure. To reduce fluorescent background from the Ga^+ ion implantation and other surface damage that occurs during the milling process, we use an Ar/Cl_2 inductively-coupled plasma etch to remove approximately 80 nm from the surface. The Ti/Pt thin film ring antennas and resistive heaters were patterned to be relatively thick (10 nm Ti, 400 nm Pt) so that the devices would operate well in air at elevated temperatures [79]. The area of the diamond where the resistive temperature detector (Omega Engineering, RTD-3-F3105-72-G-B) was bonded with ceramic adhesive (Cotronics, Durabond 950) was first roughened with an oxygen plasma to promote adhesion. The samples were mounted with ceramic adhesive on 2 mm of glass to thermally isolate the diamond and this stack was packaged in a brass holder with coplanar waveguide transmission lines similar to one that has been previously reported [83]. The temperature of the sample was controlled with a PID feedback loop using a Lakeshore 340 temperature controller. At room temperature

the feedback loop was able to stabilize the temperature of the sample to within ±10 mK as measured with the RTD and the Lakeshore temperature controller. This technology could be used for applications requiring a stabilized NV center spin resonance near room temperature [106]. At 700 K, the highest temperature measured, the temperature stability of the sample was measured using the Lakeshore controller to be within ±50 mK. As a control check we also independently calibrated our thermometry by heating the sample with the controller feedback loop and separately measuring the sample temperature with an infrared microscope (Quantum Focus Instruments). Simultaneous temperature measurements with the infrared microscope and the RTD agreed to within ±7 K between 300 K and 600 K.

All measurements discussed in the main text were taken on single NV centers. The data shown in Fig. 3.1, Fig. 3.2, and Fig. 3.5(b,c,d) was taken on an NV center (NV1) in a solid immersion lens while the data in Fig. 3.5a was taken on another NV center (NV2) in bulk diamond. The two NV centers showed nearly identical electron spin resonance (ESR) contrast temperature dependencies [Fig. A.1]. NV2 and NV1 showed similar spin-dependent excited-state lifetime temperature dependencies up to 625 K, although the lower photon collection efficiency on NV2 precluded spin-resolved lifetime measurements on this NV center at temperatures above 625 K.

A.1.2 Experimental setup

The confocal microscope setup used for this work was similar to the microscope used for angle-resolved magneto-photoluminescence studies described in Ref. [71]. Here we will describe additional experimental details relevant to the work described in the main text.

A 0.7 NA microscope objective (Mitutoyo Plan Apo) with a 6.5 mm working distance was used in order to provide clearance for the RTD on the sample surface. The overall timing of the pulsed measurements was controlled by both a pulse pattern generator (Agilent, 81110A) and a digital delay generator (Stanford Research Systems, DG645). Pulsed microwaves for ESR measurements were generated with a signal generator, I/Q modulator,

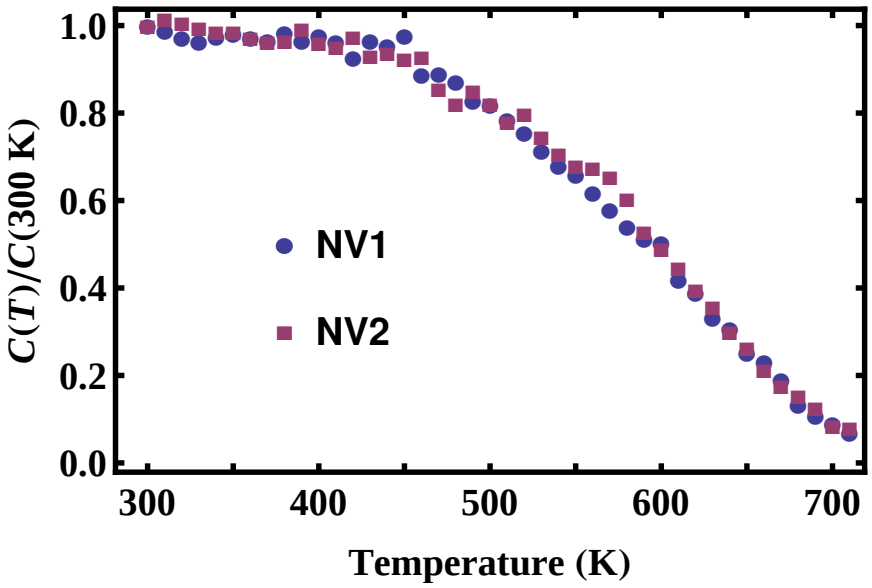

Figure A.1: Electron spin resonance contrast ($C(T)$) determined from continuous-wave ESR measurements normalized by $C(300\,\mathrm{K})$ for two different NV centers.

and arbitrary waveform generator from National Instruments (PXIe-5673E) in series with a microwave amplifier (Amplifier Research, 5S1G4). An acousto-optic modulator (AOM) from Isomet (1250C) was used to modulate the 532 nm CW laser (Oxxius, 532S-150-COL-OE) for pulsed ESR measurements. The voltage output from the AOM driver (Isomet, 525C-2) was optimized with a microwave switch, attenuators, and amplifier to provide an optical extinction of ~ 50 dB in a single pass configuration. Photon counting was performed with a silicon avalanche photodiode (Perkin Elmer, SPCM-AQRH-15-FC). For all measurements discussed in the main text the NV center's fluorescence was collected between the wavelengths of 630 nm and 800 nm. It has been shown previously that the NV center's phonon sideband does not significantly broaden over the range of temperatures measured in this work [189].

Measurements of the optical lifetime were carried out using a mode-locked Ti:Sapphire laser (Coherent Mira 900) pumped by a 7 W 532 nm Verdi G7 laser. The infrared output of approximately 1 W is fed into an optical parametric oscillator (Coherent Mira-OPO) tuned to output at 555 nm. We use a 20 m long multimode fiber (OZ Optics, QMMJ-33-UVVIS-

10/125-3A-20) to increase the pulse length to $\sim$5 ps. An electro-optic modulator (Conoptics 350) and pulse-picking electronics were used to reduce the 76 MHz repetition rate of the 555 nm pulse train. A time-correlated photon counting module (PicoHarp 300) measured the arrival time of photons into the avalanche photodiode relative to the pulse-picked 555 nm light pulses.

A.1.3 NV center optical lifetime fits

We applied a Bayesian approach to infer the spin-resolved fluorescence lifetime parameters and their associated intervals for the uncertainties shown in the main text. The difficulty of fitting sums of exponentials to experimental data is a known problem and originates from the high correlation between amplitude and lifetime parameters that tends to confound them [32, 108]. Our approach forgoes the use of asymptotic approximations in favor of calculating the actual joint posterior density to more accurately infer the parameters and their associated errors.

Before we analyze the data, we remove approximately 2.5 ns of histogram data after the initial onset of fluorescence to eliminate fast-decaying background photoluminescence detected in the sample. Because of the finite extinction of our electro-optical modulator, very small $\sim$2 ns fluorescence bursts with a 76 MHz spacing appear our raw data. Of these, we removed the first two and truncated the dataset by removing points including and after the third unwanted pulse. At each temperature, we found about six spin rotation angles were needed for good resolution of the separate lifetimes. At the driving strength used for these measurements, we could perform a π rotation in 80 ns.

For our analysis, we assume that for each microwave burst length, the fluorescence decay follows biexponential decay with a constant offset subject to random error,

$$f_{ij}\left(t_k\right) = A_j \exp\left(-t_k/\tau_{m_s=0,i}\right) + B_j \exp\left(-t_k\left(1+k_i\right)/\tau_{m_s=0,i}\right) + C_j + \epsilon, \tag{A.1}$$

where ϵ is normally distributed with mean 0 and variance $\eta^2\sigma^2_{\text{Poisson}}$. Here σ_{Poisson} is the square root of the noiseless value of $f_{ij}(t_k)$ and η is a dimensionless scaling parameter strictly above unity that accounts for other random noise in the experiment. This value is inferred from analysis of experimental data to be very close to unity, serving as a measure of goodness of fit that indicates our measurements are nearly shot-noise limited, and that any systematic effects from unextinguished pulses are within the random error of the measurement. For each microwave burst length, A_j, B_j, and C_j are free parameters while parameters $\tau_{m_s=0,i}$ and k_i are shared between burst lengths at a given temperature. $\tau_{m_s=\pm1,i}$ is related to $\tau_{m_s=0,i}$ through the rate relation,

$$\frac{1}{\tau_{m_s=\pm1,i}} = \frac{1}{\tau_{m_s=0,i}} + k_i, \tag{A.2}$$

where k_i is the difference in excited state intersystem crossing rates between the two spin states. All parameters in the analysis use non-informative and proper (bounded) prior distributions and all posterior distributions were found to be relatively insensitive to the particular form of the prior.

Because the lifetimes are shared globally between data sets at the same temperature, the posterior density typically exceeds 30 dimensions, making the use of standard numerical integration techniques infeasible. To compute marginal posterior densities for the lifetimes plotted in the main text, we employ the DREAM_{ZS} algorithm written in MATLAB [244, 136], a Markov Chain Monte Carlo (MCMC) approach that uses adaptive proposal distribution tuning, sampling from the past, and snooker update on parallel chains to rapidly explore high-dimensional posterior distributions. In MCMC, each of the N chains executes a random walk through the parameter space following a modified Metropolis-Hastings rule to control whether a proposed d-dimensional move is accepted or rejected. Because the algorithm maintains detailed balance at each step, the target distribution after a burn-in period is the desired posterior distribution. We find good results using the recommended settings along with $N = 8$ parallel chains. Convergence to the target distribution was assessed both graphically and with the Gelman-Rubin statistic, $\hat{R} < 1.05$ [91]. The point estimates for the

lifetimes and other parameters are computed from the respective sample empirical means, and the highest posterior density intervals are computed using the method of Chen and Shao [42].

To infer the parameters in the Mott-Seitz equation for non-radiative decay, we apply a similar technique of bounding the base lifetime, frequency factor, and energy barrier and computing the respective marginal posterior densities. As an approximation, we assume the likelihoods for the $m_s = 0$ lifetime at each temperature are approximately normal, setting the variance parameter equal to the empirical variance and the location parameter equal to the empirical mean of the samples generated from the individual marginal distributions via MCMC. This avoids the 337-dimensional exact approach, which we found intractable even with DREAM_{ZS}. The base lifetime and energy barriers use uniform uninformative priors while the frequency factor is bounded by its theoretical maximum ($\sim$74 meV) using a $\propto 1/s$ density to express great uncertainty in the scale of this value; there exists some sensitivity (within the quoted error) of the posterior on the choice of this prior since we were unable to measure above 675 K. The analysis also allows for a linear systematic temperature offset up to a maximum of 10 K at 700 K, although this correction is essentially negligible. We compute the marginal densities for the Mott-Seitz parameters and quote summary statistics in the main text as previously described.

A.1.4 Rate equation modeling

A simplified model of the NV center with five energy levels is used to model the optically detected ESR signal observed in experiment [161]. We augment the classical rate equation model of Ref. [161] with the off-diagonal terms from the density matrix that give rise to coherent driving in the orbital ground state with dissipation. We numerically integrate this expression, a master equation of the Lindblad form, to simulate the time evolution of the system under both optical and microwave excitation that correspond to experimental conditions [131, 145, 192]. We use the optical decay rates measured in our experiment and

Transition Rate	Value
k_{42}, k_{31}	75 MHz [161]
k_{32}, k_{41}	1.5 MHz [161]
k_{51}	$1/\left((1+1/1.6)\,371\times(1-e^{-16.6\,\mathrm{meV}/(k_BT)})\right)$ GHz [203]
k_{52}	$1/\left((1+1.6)\,371\times(1-e^{-16.6\,\mathrm{meV}/(k_BT)})\right)$ GHz [203]
k_{45}	$60+2.552\times10^5\times e^{-0.48\,\mathrm{eV}/k_BT}$ MHz
k_{35}	$2.552\times10^5\times e^{-0.48\,\mathrm{eV}/k_BT}$ MHz
k_{pump}	0.3×75 MHz

Table A.1: A summary of the numerical values used for the rate-equation components of the density matrix formalism.

the non-spin-conserving optical transition rates from Ref. [161], and assume that they are temperature-independent. To capture the temperature dependence of the transition rates, we use the best fit equation versus temperature for the singlet rates from Ref. [203] and the Mott-Seitz equation plotted in the main text added to the room temperature intersystem crossing rates equally for the excited spin states. The s parameter in the Mott-Seitz equation was obtained using least squares while fixing the energy and 300 K lifetime at the respective means of their marginal distributions. The ESR contrast is computed by comparing the steady-state luminescence when microwaves are applied continuously versus the luminescence without microwaves, corresponding to the highly-detuned case we use for normalization. To compute the theoretical dependence of the photoluminescence on temperature, we compute the value of the steady-state luminescence under constant optical pumping with no applied microwaves. Both the theoretical contrast and photoluminescence values are normalized to unity at room temperature and plotted with experimental data to generate the figures in the main text. The model also predicts relatively robust spin preparation into the $m_s = 0$ sublevel in the ground state after repeated optical cycling, which is consistent with the polarizations inferred in our analysis shown in Fig. A.2 to within the statistical uncertainty. We summarize the rates used in Table A.1.

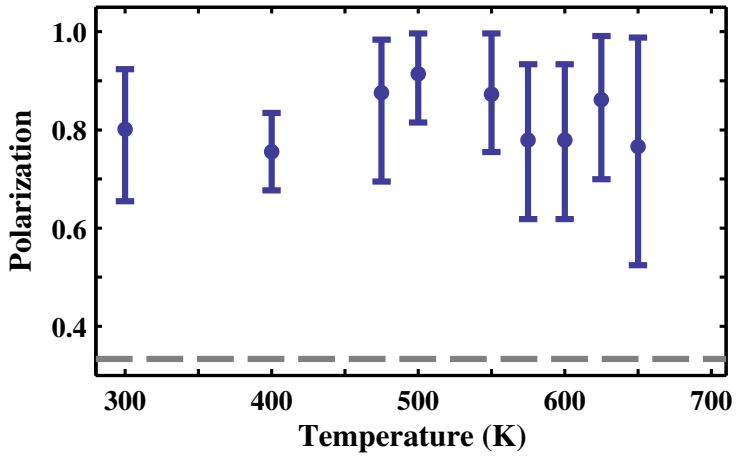

Figure A.2: Plot of maximum spin polarization in the $m_s = 0$ spin state inferred from fits to the data with no microwaves applied (95% intervals). The data are consistent with robust spin preparation up to at least $\sim 650\,\mathrm{K}$. The dashed line indicates the polarization for an unpolarized spin.

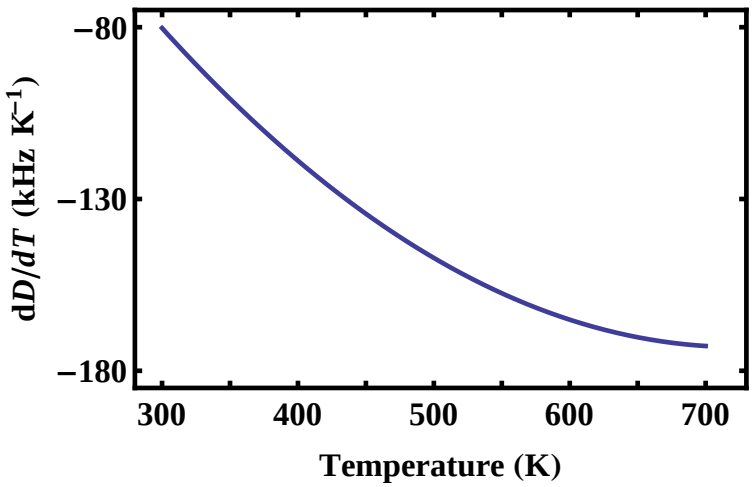

Figure A.3: The derivative of the third-order polynomial fit to $D(T)$ with respect to T, $dD(T)/dT$, for NV1.

A.1.5 Temperature dependence of the NV center spin resonance between 300 K and 700 K

As is mentioned in the main text, we find that the temperature dependence of the NV centers crystal field splitting (D) can be accurately described by a third order polynomial, $D(T) = a_0 + a_1 T + a_2 T^2 + a_3 T^3$, between 300 K and 700 K. A best fit to this expression yields $a_0 = (2.8697 \pm 0.0009)$ GHz, $a_1 = (9.7 \pm 0.6) \times 10^{-6}$ GHz/K, $a_2 = (-3.7 \pm 0.1) \times 10^{-7}$ GHz/K^2, and $a_3 = (1.7 \pm 0.1) \times 10^{-10}$ GHz/K^3, with a reduced χ^2 value of 1.3. The nonlinear temperature-dependence of $\frac{dD(T)}{dT}$ is beneficial for high-temperature thermometry applications, as the level shifts become larger at higher temperatures [Fig. A.3]. As has been discussed in previous works, these thermal shifts in D are larger than expected from estimates based on macroscopic thermal expansion [3, 43].

A.1.6 Single spin longitudinal relaxation measurements

As noted in the main text, single NV center T_1 times were too long at elevated temperatures to contribute to the quenching of PL intensity and ESR contrast observed above 550 K. T_1 measurements were performed for the $m_s = 0$ spin state by initializing the spin with a 2 μs laser pulse with a variable measurement period. Spin-state readout was performed by collecting the photoluminescence of the first 350 ns of the subsequent initialization laser pulse. Longitudinal relaxation measurements at 500 K and 600 K showed the NV1's T_1 times to be (600 ± 100) μs and (340 ± 50) μs, respectively [Fig. A.4]. For comparison the Rabi and Ramsey measurements, which showed ESR contrasts consistent with the CW ESR experiments, were performed with a measurement period of ~ 5 μs.

A.1.7 Ramsey measurements

The T_2^* values in the main text were inferred from fits to the decay of Ramsey oscillation measurements. The Ramsey measurements were carried out by first optically initializing

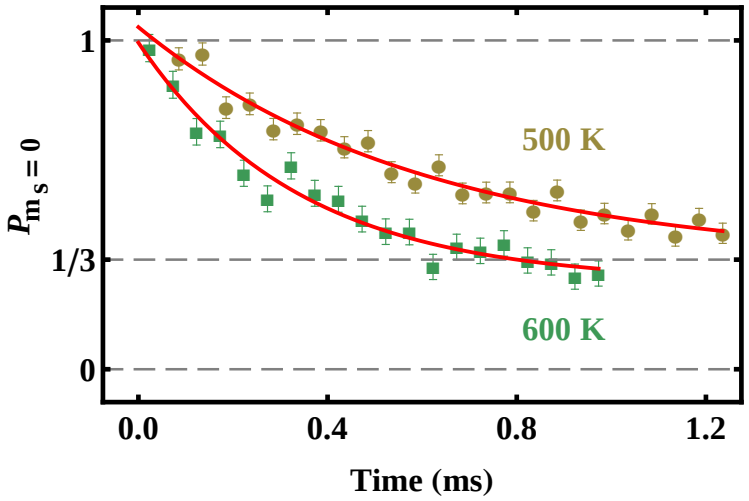

Figure A.4: Longitudinal relaxation measurements performed on NV1 ($m_s = 0$ spin state) at 500 K (gold) and 600 K (green). $P_{m_s=0}$ was calibrated from the photoluminescence intensity after optical initialization ($P_{m_s=0} = 1$) and after optical initialization and a microwave π pulse resonant with the $m_s = 0$ to $m_s = -1$ spin transition ($P_{m_s=0} = 0$). The error bars reflect uncertainties from the photon counting statistics (68% intervals). The solid red lines are exponential fits to the data which yield T_1 times of $(600 \pm 100)\,\mu$s and $(340 \pm 50)\,\mu$s at 500 K and 600 K, respectively.

the spin using a $2\,\mu$s 532 nm laser pulse. After waiting $\sim$500 ns for the singlet pathway to depopulate, we rotated the spin into a superposition of its $m_s = 0$ and $m_s = -1$ spin states with a $\pi/2$ pulse and allowed the spin to evolve for a variable time τ_R. A second $\pi/2$ pulse was used to convert the phase of the spin acquired during free evolution into a population difference and the spin was then read out by collecting its fluorescence for the first ~ 350 ns of the following laser pulse. The primary NV center studied in this work showed a hyperfine coupling of $\sim$ 2.5 MHz to a nearby ^{13}C ($I = \frac{1}{2}$) in addition to its hyperfine coupling its ^{14}N nuclear spin ($I = 1$). To simplify the hyperfine spectrum to allow for more accurate fits to T_2^* we performed the Ramsey measurements at 500 G to polarize the nitrogen nuclear spin into its $m_I = +1$ state [113]. This resulted in a hyperfine spectrum with two visible ESR transitions showing a relative polarization consistent with Ref. [218]. For the Ramsey measurements, we detuned the $\pi/2$ pulses by -2 MHz from the lower frequency ESR transition to induce oscillations in the measured PL intensity as a function of τ_R. We

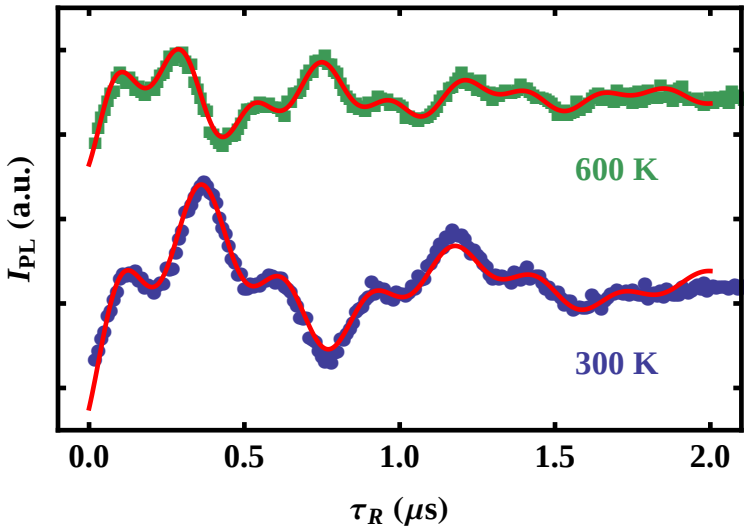

Figure A.5: Ramsey oscillation measurements performed on NV1 at 300 K (blue) and 600 K (green). The measurements were done at 500 G. The $\pi/2$ pulses were detuned from the lower-frequency hyperfine resonance by -2 MHz on the $m_s = 0$ to $m_s = -1$ spin transition. The solid red lines are best fits to the data using Eq. S3. The relative amplitudes of the Ramsey oscillations reflect the relative ESR contrasts of the two measurements.

fit the resulting data [Fig. A.5] with the function

$$y = \exp\left(-\left(\frac{t}{T_2^*}\right)^2\right)\left(A_1\cos\left(\omega_1 t + \phi_1\right) + A_2\cos\left(\omega_2 t + \phi_2\right)\right) + y_0 \tag{A.3}$$

to account for the two visible ESR transitions and to extract T_2^*. The Rabi measurements shown in the main text were carried out with a similar sampling scheme except that resonant microwave pulses of varying duration (burst length) were applied instead of the $\pi/2$ - τ_R - $\pi/2$ portion of the Ramsey pulse sequence.

A.1.8 Single spin thermometry

The expression for the NV center's thermal sensitivity quoted in the main text is analogous to those obtained for NV center DC magnetic field sensitivities using a Ramsey pulse sequence. This method has been detailed extensively elsewhere [249, 234]. The basic principle of these measurements is that Zeeman shifts induce changes in the spin dynamics during the free

evolution component of a Ramsey pulse sequence and these dynamics are converted to a measurable population difference during the subsequent projection and readout of the NV center spin. The key point pertaining to this work is that both the crystal field splitting (D) and an applied magnetic field determine the spin dynamics during the free evolution. Therefore changes in temperature, which lead to changes in D, could be inferred through these measurements. The only difference between Eq. 3.2 of the main text and Eq. 1 of Ref. [234] is that $\frac{dD(T)}{dT}$ has been substituted for $g^*\mu_B/h$. The parameter $S(T)$ quoted in the main text is given by $S\left(T\right) = \left(1 + 2\left(\alpha_0 + \alpha_1\right)/\left(\alpha_0 - \alpha_1\right)^2\right)^{-\frac{1}{2}}$, where $\alpha_0 = \tau_{\mathrm{L}} I_{\mathrm{PL}}\left(T\right)$ and $\alpha_1 = \tau_{\mathrm{L}} I_{\mathrm{PL}}\left(T\right)\left(1 - C_{\mathrm{P}}\left(T\right)\right)$. Here τ_{L} is the fluorescence readout duration and $C_{\mathrm{P}}\left(T\right)$ is the contrast of a pulsed ESR measurement. For consistency, we calculated the sensitivity plotted in the Fig. 3.5d of the main text using experimental values all measured from NV1. We determined $\frac{dD(T)}{dT}$ from the derivative of the polynomial fit to $D(T)$ shown in Fig. A.3. The T_2^* value used was $1.24\,\mu$s, which corresponds to a weighted average of the data in Fig. 3.5b. We determined $C_{\mathrm{P}}\left(T\right)$ from the experimental data points in Fig. 3.4 and we took the $C_{\mathrm{P}}\left(300\,\mathrm{K}\right)$ contrast to be 0.24 (the measured Rabi contrast at the magnetic field at which the T_2^* values were measured). We determined $I_{\mathrm{PL}}(T)$ from the experimental datapoints in Fig. 3.4, with $I_{\mathrm{PL}}\left(300\,\mathrm{K}\right)$ equal to 80 kCps. τ_{L} was taken to be 350 ns for all temperatures. We note that the optimal duration of τ_{L} (for maximum signal to noise) decreases slightly at elevated temperatures due the temperature-dependence of the NV center's ^1E singlet lifetime. These experimental values could also be improved in future experiments through materials engineering [12] or by carefully controlling the spin's magnetic field environment. In particular, T_2^* times 100x longer than those measured in this work have been observed for single NV centers in isotopically pure diamond [116]. Finally, we note that it may be easier to implement thermal sensing with NV centers using methods other than the Ramsey pulse sequence described above. DC magnetometry using single NV centers has been experimentally demonstrated using both field-frequency lock methods [211] and pulsed ESR spectroscopy methods [68]. Both methods have DC magnetic field sensitivities equivalent to

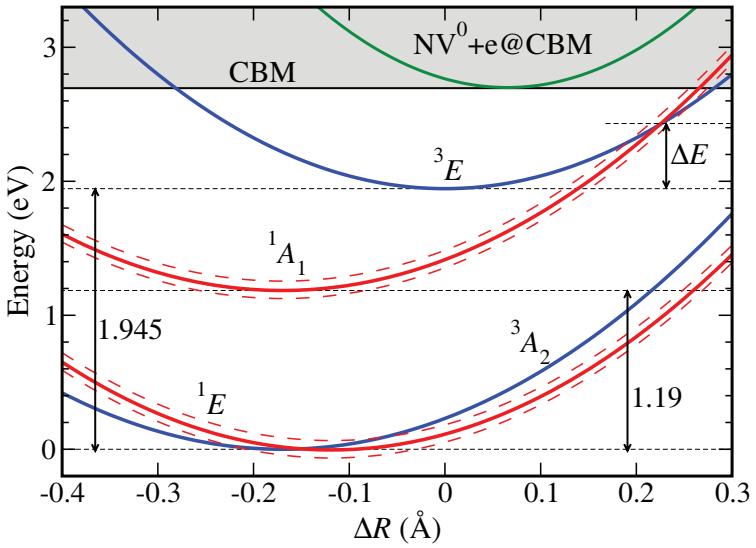

Figure A.6: The configuration coordinate diagram of the NV^- center. ΔR measures the total displacement of all atoms along the path that interpolates between equilibrium geometries of the defect in the $^3A_2$ and ^3E electronic states. All energies are relative to the $^3A_2$ state's equilibrium energy. We placed the $^1A_1$ state based on the assumption that its equilibrium atomic configuration and vibrational frequencies were similar to those of the $^3A_2$ state and using our measurement of ΔE. The ^1E state was placed 1.19 eV below the $^1A_1$ state based on the known energy difference of these two states. The uncertainty in the placement of the $^1A_1$ and ^1E states reflects the uncertainty in ΔE (68% interval). The zero phonon lines between the triplet (1.945 eV) and singlet (1.19 eV) states are indicated. The NV^0 state and conduction band minimum are added for comparison with the other energies as discussed in the text.

those of the Ramsey pulse sequence up to a constant of order unity and could be applied for thermal sensing as well.

A.2 Electronic structure calculations

The configuration coordinate diagram (CCD) presented in Fig. 3.3 depends on the values of Stokes (S) and anti-Stokes (AS) shifts pertaining to the optical transition between triplet states (i.e. relaxation energies in the excited and ground states). While these quantities influence greatly the shape of optical absorption and luminescence bands, it is not straightforward to extract them from measurements, such as those presented in Ref. [52]. Therefore, to determine the values of these shifts, we have utilized electronic structure calculations [88, 247].

The calculations in this work were performed employing the hybrid density functional of Heyd, Scuseria, and Ernzerhnof (HSE06) to describe the NV center's electronic structure [105]. Atomic cores were treated via the projector-augmented-wave (PAW) scheme [30], and the plane wave cutoff for valence wave functions was set to 400 eV. To simulate the NV^- center, we used a cubic supercell nominally containing 216 atoms. The Γ-point was used for the Brillouin zone integration. To simulate the excited state triplet, we used a method outlined in Ref. [88], whereby an electron in the spin-minority channel is promoted to the e state thus leaving a hole in the a_1 state. We employed the code `VASP` [133]. A similar computational methodology was also used in Refs. [88, 247].

The equilibrium geometry of the defect in the $^3A_2$ state has been determined by fully relaxing the geometry. The resulting point symmetry was C_{3v}, and the electron configuration $a_1^2e^2$. In the ^3E state the C_{3v} symmetry is broken, but the energy associated with symmetry breaking is small ($\sim$0.025 eV) [1]. In the main text it is assumed that the C_{3v} symmetry is maintained for equilibrium geometries of all electronic states of the NV^- center. In particular, it implies that the symmetry is maintained along the path that interpolates between equilibrium geometries of the defect in $^3A_2$ and ^3E electronic states [cf. Fig. 3.3]. This reasoning neglects the occurrence of the (dynamic) Jahn-Teller effect in the ^3E (and possibly ^1E) state (see Refs. [1, 82]).

The calculated parameters of the defect depend somewhat sensitively on the adopted lattice constant. The theoretical lattice constant of diamond is 3.539 Å, and is thus slightly underestimated with respect to the experimental value of 3.567 Å [210]. Employing the theoretical lattice constant, we obtain the value of 2.035 eV for the zero phonon line (ZPL) of the optical transition between the triplet ^3E and $^3A_2$ states. The resulting S and AS shifts are 0.291 and 0.245 eV. If the experimental lattice constant is adopted, the ZPL reduces to 1.972 eV (thus in better agreement with the experimental value of 1.945 eV). Similarly, S and AS shifts decrease, to 0.274 and 0.230 eV, respectively. Thus, for a $\leq$1 % change in the lattice constant, the resulting change in S and AS is more than 5%. This is a likely

consequence of the high rigidity of the diamond lattice. We have used the parameters from the second set of calculations to construct the CCD presented in Fig. 3.3. We estimate that the uncertainty 0.02 eV in the values of the S and AS shifts translates into an uncertainity of about 0.1 eV in the resulting position of the $^1A_1$ and ^1E states. This uncertainty should be considered in addition to experimental error bars shown in Fig. 3.3.

A.2.1 Electron density of the $^1A_1$ state

The construction of the configuration coordinate diagram in Fig. 3.3 is based on the assumption that the equilibrium electron density of the $^1A_1$ state is very similar to that of the $^3A_2$ state along the generalized configuration coordinate. In the molecular orbital picture, the wavefunction of the $^3A_2$ state (spin projection $m_\mathrm{s} = +1$) is [62, 167]:

$$\left|{}^3A_2, m_\mathrm{s} = +1\right\rangle = \left|a_1\bar{a}_1 e_x e_y\right\rangle . \tag{A.4}$$

Focusing only on the sub-space spanned by two electrons in e states, we can write an explicit form of this wavefunction:

$$\Phi\left({}^3A_2, m_\mathrm{s} = +1\right) = \frac{1}{\sqrt{2}}\left[e_x(1)e_y(2) - e_y(1)e_x(2)\right]\cdot\alpha(1)\alpha(2), \tag{A.5}$$

where 1 and 2 is a short-hand notation for spatial or spin coordinates of the two electrons. The electron density associated with this wavefunction is

$$\begin{aligned}\rho(1) &= 2\int\sum_{\text{spin}}\Phi(1,2)\Phi^\dagger(1,2)d2 \\ &= \int\left[e_x^2(1)e_y^2(2) - 2e_x(1)e_y(1)e_y(2)e_x(2) + e_y^2(1)e_x^2(2)\right]d2 = e_x^2(1) + e_y^2(1)\end{aligned} \tag{A.6}$$

which is expected for a single Slater determinant. Naturally, the same applies to other values of m_s. Pair densities of the form $e_x(1)e_y(1)$ do not appear in the final expression because

single-particle states e_x and e_y are orthogonal.

The wavefunction of the ${}^1A_1$ state is a sum of two Slater determinants [62, 167]:

$$\left|{}^1A_1\right\rangle = \frac{1}{\sqrt{2}}\left(|a_1\bar{a}_1 e_x\bar{e}_x\rangle + \left|a_1\bar{a}_1 e_y\bar{e}_y\right\rangle\right). \tag{A.7}$$

The explicit form of this wavefunction, focusing on the two electrons in the e states, is then:

$$\Phi\left({}^1A_1\right) = \frac{1}{\sqrt{2}}\left[e_x(1)e_x(2) + e_y(1)e_y(2)\right]\cdot\frac{1}{\sqrt{2}}\left[\alpha(1)\beta(2) - \beta(1)\alpha(2)\right], \tag{A.8}$$

with a symmetric real-space part and an anti-symmetric spin part. The real-space part of the wavefunction has thus a bosonic symmetry, and this causes obvious problems when treating such wavefunctions within density-functional theory based approaches. However, similar to the ${}^3A_2$ state, the electron density associated with e electrons in the ${}^1A_1$ state can be shown to be $e_x^2(1) + e_y^2(1)$:

$$\begin{aligned}\rho(1) &= 2\int\sum_{\text{spin}}\Phi(1,2)\Phi^\dagger(1,2)d2 \\ &= \int\left[e_x^2(1)e_x^2(2) + 2e_x(1)e_y(1)e_x(2)e_y(2) + e_y^2(1)e_{ye}^2(2)\right]d2 = e_x^2(1) + e_y^2(1),\end{aligned} \tag{A.9}$$

Assuming that the single-particle orbitals do not change much in the two electronic states, this implies that electron densities and thus forces on atoms are very similar in the two electronic states as long as the C_{3v} symmetry is maintained. Furthermore, in this consideration the mixing of the ${}^1A_1$ singlet with higher-lying singlets (with the nominal electron configuration e^4) is ignored. Since the latter has a very high energy [194], this assumption seems justified.

The conclusion about very similar electron densities in the singlet and the triplet state seems to be in contrast to knowledge acquired considering Heitler-London-type wavefunctions. These occur, e.g. in studying the hydrogen molecule or coupled quantum dots. In these situations electron densities of the triplet and the singlet wavefunctions are very dif-

ferent due to the appearance of mixed densities of the form $e_x(1)e_y(1)$ [142]. This is due to the fact that single-electron orbitals in the Heitler-London wavefunction are typically not orthogonal.

A similar reasoning applies to the electron density of the ^1E state. In this case the C_{3v} symmetry can be broken, but the energy related to symmetry breaking is small (see above). However, ^1E level can interact with $^1E'$ level (electron configuration a_1e^3), and thus the resulting electron density is slightly different from that of the $^1A_1$ state. There are some indications that the admixing coefficient of the a_1e^3 configuration is about 0.3 [158]. In broad terms, this indicates that the equilibrium geometry of the defect in the ^1E state is (approximately) a weighted average of the geometries in $^3A_2$ and ^3E states. This information was used in placing the total energy curve pertaining to the ^1E state in Fig. 3.3.

In the main text we mention the experimental results of Robledo *et al.* [203] and Acosta *et al.* [4] as indicating that a small energy barrier exists for nonradiative relaxation from the ^1E state. Under the assumption that the ISC is dominated by single-phonon emission, energies of 17 meV [203] and 15 meV [4] have been inferred from the temperature dependence of the ^1E state lifetime. The fact that the equilibrium geometries of the ^1E and $^3A_2$ states are slightly different, as discussed above, makes non-radiative relaxation via multiphonon emission a viable alternative. However if such a process is feasible, the energy barrier inferred from a Mott-Seitz fit to the ^1E state lifetime should not be interpreted as the energy difference between the $^3A_2$ and ^1E states, but as the barrier for thermally-activated nonradiative relaxation, in close analogy to the situation discussed in the main text. The fact that the equilibrium geometry of the ^1E state is a weighted average of the geometries in $^3A_2$ and ^3E states, puts a value of $\sim$0.25 eV (the sum of the anti-Stokes shift and the deduced barrier) as the upper limit for the separation of the two states. Thus, if interpreted in terms of the ISC assisted by multi-phonon emission, the results of Refs. [203] and [4] are consistent with a model in which only two singlet states are invoked.

A.2.2 The influence of other charge states

The ionization of the NV^- center whereby the electron escapes to the conduction band is a process which can become possible at higher temperatures. The formation energy of the NV center in difference charge states has been calculated in Ref. [247]. The $(0/-)$ charge transition levels is situated at ~ 2.8 eV above the VBM. This allows one to estimate the ionization of NV^- defect in its ^3E state to be about 0.7-0.8 eV. To gain insight into the kinetics of this process, we have constructed the configuration coordinate diagram that includes the ^2E state of the NV^0 center [Fig. 3.3]. A sufficiently high ionization energy and a small difference in the equilibrium geometries between the two relevant states (total distortion $\sim$0.07 Å) combine to produce a very high effective barrier for the escape of an electron to the conduction band. Thus, we can safely exclude the relevance of the NV^0 state in thermally-activated non-radiative relaxation.

APPENDIX B

FLUORESCENCE THERMOMETRY ENHANCED BY THE QUANTUM COHERENCE OF SINGLE SPINS - DETAILS

The NV centers were addressed in a confocal microscope with a 0.7 NA microscope objective that allowed sufficient clearance for a resistive temperature detector (RTD) to be adhered to the diamond surface. The NV centers were optically excited with a 532 nm continuous-wave laser. For pulsed spin resonance measurements the timing of the experiment was controlled by an arbitrary waveform generator. The laser was modulated using an acousto-optic modulator; the electrical signal from the AOM driver was optimized with a diode-based filter to provide high optical extinction in a single pass. For the zero field experiments microwaves were supplied by a single signal generator gated with a mixer and switch in series. For the finite field experiments two signal sources, each independently gated with a mixer and a switch, were combined using a power splitter. In all experiments the microwave signals were amplified and delivered to a Ti/Pt short termination to a coplanar waveguide to produce Rabi frequencies of $\approx 25\,\mathrm{MHz}$. For the finite field measurements, magnetic fields were controlled to within 0.1 Gauss using three-axis Helmholtz coils. The temperatures quoted in the main text reflect measurements performed with an RTD adhered to the sample surface. The RTD and a lithographically patterned Ti/Pt resistive heater were connected to a PID feedback loop that stabilized the temperature, as measured by the RTD, to better than $\pm 10\,\mathrm{mK}$. Further details of the temperature control are provided in Ref. [236] The sample was an electronic grade diamond from Element Six with natural 13C abundance (1.1 %) that was irradiated with 2 MeV electrons (1 x 1014 cm2) and annealed in forming gas at 800 C for 2 hours to increase the NV center density.

B.1 Temperature measurement protocols

First, let us consider temperature measurements in an external bias field B, between a few and a few hundred Gauss. In this regime, the NV center spin states (with $m_s = 0$, 1, and +1, below referred to as $|0\rangle$, $|-1\rangle$, and $|+1\rangle$, respectively) are well-separated, and the NV center electron spin resonance (ESR) spectrum contains well-isolated lines corresponding to different ESR transitions, $|0\rangle \rightarrow |-1\rangle$ and $|0\rangle \rightarrow |+1\rangle$. We compare the performance of three protocols: the regular Hahn echo on the $|0\rangle \rightarrow |-1\rangle$transition, the thermal echo (TE), and the thermal CPMG (TCPMG). The general measurement scheme is the same for all of the protocols. We start with the NV center spin polarized in the state $|0\rangle$. We apply a preparation pulse (/2) at the frequency of the $|0\rangle \rightarrow |-1\rangle$ transition, which prepares a superposition $(1/\sqrt{2})[|0\rangle + |-1\rangle]$. The system then evolves under a given protocol. In the end, the phase between $|0\rangle$ and $|-1\rangle$ states is read out by applying another $(\pi/2)_-$ pulse, followed by the optical measurement of the probability for the NV center spin to be in the state $|0\rangle$.

A single period of the TE protocol has the structure

$$\tau - \pi_+\pi_-\pi_+ - \tau - \pi_-\pi_+\pi_- \tag{B.1}$$

where π_- and π_+ are the π-pulses applied at the frequency of the $|0\rangle \rightarrow |-1\rangle$ and $|0\rangle \rightarrow |+1\rangle$ transitions, respectively, and τ denotes an inter-pulse delay. Note that the second triple of π-pulses is different from the first one. The TCPMG protocol is a symmetrized version of TE, and one period of TCPMG has the structure

$$\tau - \pi_+\pi_-\pi_+ - 2\tau - \pi_-\pi_+\pi_- - \tau \tag{B.2}$$

so that the inter-pulse delays are placed symmetrically between the preparation and the readout pulses. The Hahn echo protocol is standard, $\tau - \pi_- - \tau$.

The Hamiltonian describing the NV center spin, placed in a magnetic field B (for simplicity in this discussion we ignore factors of $g\mu_B$), subjected to a random quasi-static field δB, and interacting with the bath of ^{13}C nuclear spins has the form

$$H = DS_z^2 + (B + \delta B)S_z + S_z H_{B1} + H_{B2} \tag{B.3}$$

is the z-component operator of the NV center electronic spin (z-axis is directed along the [111] direction) and $D = 2\pi \cdot 2.87\,\mathrm{GHz}$ is the NV centers zero-field splitting. The third term includes the hyperfine coupling of the NV center spin to the bath of ^{13}C spins; since this coupling is much smaller than D, the value of S_z is a well-conserved quantity, so that the hyperfine coupling Hamiltonian does not include S_x and S_y. For the same reason, we neglected the contribution from the x- and y-components of the random field. The last term describes the internal dynamics of the ^{13}C nuclear spin bath. We assume that the NV center spin is subject to a magnetic field B which has a constant component and a random quasistatic component which causes dephasing. We aim to eliminate this quasistatic component and to minimize the influence of the ^{13}C spin bath. Besides coupling with the ^{13}C spins, the NV center electronic spin is coupled to the intrinsic ^{14}N nuclear spin, and the corresponding hyperfine Hamiltonian has the form AS_zI_z (where I_z is the z-component of the ^{14}N nuclear spin). Since the ^{14}N spin remains static on the timescale of a single experimental run, this hyperfine coupling can be added to the δB field above, and as we will see below, is eliminated by the decoupling sequence.

First, let us consider the spin's evolution under the triples of π-pulses, and remember that the contribution from the bath of ^{13}C spins and from the random field δB can be neglected during short and strong pulses. For instance, let's take the second triple, $\pi_-\pi_+\pi_-$. It involves irradiation of the sample with microwave fields of two different frequencies, and it is more convenient to perform the analysis in the laboratory frame. We first apply a driving field at the frequency $\omega_1 = DB$ of the $|0\rangle \to |-1\rangle$ transition; the action of the driving is

described by the Hamiltonian term

$$H_{R1} = 2h_1 S_x \cos(\omega_1 t + \phi_1) \tag{B.4}$$

and the duration of the microwave pulse (t_{p1}) is adjusted to provide a π-rotation. The evolution can be analyzed in a frame rotating with frequency ω_1 using the standard secular approximation, and then re-cast back to the lab frame. In the rotating frame, defined by the unitary transformation $\exp[it\omega_1 S_z] = \exp[it(DB)S_z]$, we have the evolution operator

$$U_1^{'} = \begin{pmatrix} \exp[-i(D+B+\omega_1)t_{p1}] & 0 & 0 \\ 0 & 0 & -i\exp(i\phi_1) \\ 0 & -i\exp(-i\phi_1) & 0 \end{pmatrix} \tag{B.5}$$

The corresponding evolution operator in the lab frame is

$$U_1 = \begin{pmatrix} \exp[-i(D+B)t_{p1}] & 0 & 0 \\ 0 & 0 & -i\exp(i\phi_1) \\ 0 & -i\exp(-i\phi_1 - i\omega_1 t_{p1}) & 0 \end{pmatrix} \tag{B.6}$$

Similarly, for the second π-pulse applied to the $|0\rangle \rightarrow |+1\rangle$ transition with frequency $\omega_2 = D+B$, with phase ϕ_2, and with the duration t_{p2}, the rotating frame is defined by the unitary transformation $\exp[it\omega_2 S_z] = \exp[it(D+B)S_z]$. The resulting evolution operator in the lab frame is

$$U_2 = \begin{pmatrix} 0 & -i\exp(-i\phi_2 - i\omega_2 t_{p2}) & 0 \\ -i\exp(i\phi_2) & 0 & 0 \\ 0 & 0 & \exp[-i(D-B)t_{p2}] \end{pmatrix} \tag{B.7}$$

The full evolution operator in the lab frame under the triple of π-pulses is $U = U_+ U U_+$, and

has a form:

$$U_{pmp} = \begin{pmatrix} 0 & 0 & -i\exp(-ia_1) \\ 0 & -\exp(-ia_2) & 0 \\ -\exp(-ia_3) & 0 & 0 \end{pmatrix} \tag{B.8}$$

where the phase factors are $a_1 = \phi_2\phi_1 + 2Dt_{p2}$, $a_2 = (D+B)(t_{p2}+t_{p1})$, and $a_3 = \phi_1\phi_2 + (DB)(t_{p1}+t_{p2})$. In a similar way, we can calculate the evolution operator for the other triple of π-pulses, to obtain

$$U_{mpm} = \begin{pmatrix} 0 & 0 & -i\exp(-iq_1) \\ 0 & -\exp(-iq_2) & 0 \\ -\exp(-iq_3) & 0 & 0 \end{pmatrix} \tag{B.9}$$

with $q_1 = \phi_2\phi_1 + (D+B)(t_{p2}+t_{p1})$, $q_2 = (DB)(t_{p1}+t_{p2})$, and $q_3 = \phi_1\phi_2 + 2Dt_{p1}$.

If the TE protocol B.1 is applied to the initial state $|-1\rangle$, then the first inter-pulse delay produces the phase factor $\exp[i\tau(DB\delta B)]$. Moreover, the coupling to the ^{13}C spin bath produces a decoherence factor $V_1 = \exp[i\tau(H_{B1} + H_{B2})]$. Then, the first triple of pulses adds a phase a_3, and changes the state to $|+1\rangle$. The second inter-pulse delay produces the phase factor $\exp[i\tau(D + B + \delta B)]$ and a decoherence factor $V_{+1} = \exp[i\tau(H_{B1} + H_{B2})]$, which corresponds to $S_z = +1$. The final triple of pulses turns the state back to $|-1\rangle$, also adding the phase q_1. Thus, the initial state is transformed by the full protocol as follows:

$$|-1\rangle \rightarrow W_{-1}\,|-1\rangle = \exp[-i(2\tau D + a_3 + q_1)]V_{+1}V_{-1}\,|-1\rangle\,. \tag{B.10}$$

If the initial state is $|0\rangle$, then each inter-pulse delay produces a decoherence factor $V_0 = exp[i\tau H_{B2}]$, and the total phase produced by the two π-pulse triples is $a_2 + q_2$. The total transformation is

$$|0\rangle \rightarrow W_0\,|0\rangle = \exp[-i(a_2 + q_2)]V_0^2\,|0\rangle\,. \tag{B.11}$$

A very useful feature of the protocol is the fact that the total phase $a_2 + q_2$ added by pulses

to the state $|0\rangle$ is the same as the total phase $a_3 + q_1$ added by pulses to the state $|-1\rangle$ (also, the same is true for $|+1\rangle$. Thus, these phase factors do not affect the mutual phase between $|0\rangle$ and $|-1\rangle$, and can be omitted. In other words, the total signal remains independent of the duration of the pulses, independent of short delays between the π-pulses, and independent of the two microwave source phases. In fact, this property of the TE and TCPMG protocols holds for even more general patterns of the phase accumulation.

As a result, the measured signal S is determined only by the phase difference $2D\tau$ accumulated during the inter-pulse delays. The contributions from the external field, as well as from the random field and from the phases of the microwave sources, are cancelled. This ensures an excellent sensitivity of the method as is demonstrated in the main text. The signal $S(2\tau)$ oscillates rapidly with frequency D (close to 3 GHz) in the laboratory frame, and slowly decays on a timescale of tens to hundreds of microseconds due to decoherence from the ^{13}C spin bath.

This decay is the main factor limiting the accurate measurement of D. The envelope amplitude S_e of the measured signal is diminished due to entanglement with the ^{13}C spins, and is given by the expression

$$S_{e1} = \frac{1}{2} + \frac{1}{2}\mathrm{Re}\frac{\mathrm{Tr}[V_0^2(V_{+1}V_{-1})^\dagger]}{\mathrm{Tr}_B \mathbf{1}_B} \tag{B.12}$$

The unitary operators of the bath $V_{0,\pm1}$ are given in Eqs. B.10 and B.11, and are just the conditional evolution operators of the bath corresponding to the NV center spin being in the states $|0\rangle$ and $|\pm1\rangle$, respectively. Tr_B denotes the trace over the bath, and $\mathbf{1}_B$ is the identity operator in the space of the bath, which ensures correct normalization.

A similar analysis can be performed for the TCMPG protocol. Again, it is easy to verify that the phase contributions from the pulses become irrelevant at the end of the protocol period, and the contributions from the external fields B and B are cancelled as well. The signal $S(4\tau)$ also oscillates with frequency D in the laboratory frame. The impact of

decoherence on the envelope S_e can also be calculated, and after a single TCPMG period it has the form

$$S_{e2} = \frac{1}{2} + \frac{1}{2}\mathrm{Re}\frac{\mathrm{Tr}_B[V_0^4(V_{-1}V_{+1}V_{+1}V_{-1})^\dagger]}{\mathrm{Tr}_B\mathbf{1}_B} \tag{B.13}$$

where the decoherence term follows the sequence of the NV center spin states. For comparison, the decay of the spin echo envelope is given by

$$S_{e0} = \frac{1}{2} + \frac{1}{2}\mathrm{Re}\frac{\mathrm{Tr}_B[V_{-1}V_0(V_0V_{-1})^\dagger]}{\mathrm{Tr}_B\mathbf{1}_B} \tag{B.14}$$

At very small magnetic fields, when the $|0\rangle \to |-1\rangle$ and $|0\rangle \to |+1\rangle$ transitions coalesce such that the $|-1\rangle$ and $|+1\rangle$ levels are almost degenerate, the temperature sensing protocols have simpler structures. A single π-pulse produces the simultaneous transformations (up to a common phase factor)

$$|-1\rangle \to |+1\rangle\,,\ |0\rangle \to |0\rangle\,,\ |+1\rangle \to |-1\rangle\,, \tag{B.15}$$

which at larger B requires the above-mentioned triples of π-pulses. Here, for clarity, we omitted the decoherence factors. The decoherence analysis can be performed in analogous manner to the case of the moderate-to-large B, and the conclusions are similar.

B.2 Decoherence from the nuclear spin bath process

For an NV center spin decohered by a dilute nuclear spin bath, the fine quantitative details of the decoherence process are not universal [44, 61, 227, 250]. They are determined by the specific positions of the nuclear spins around the given NV center, and change from one center to another. For instance, the initial shape of the signal decay (quadratic or quartic in time) is universal, but is limited to very short timescales. As we will see below, the long-time evolution is rather different from one NV center to another. Therefore, we aim to understand only the main qualitative features of the decoherence process.

At the relevant timescales, from ten to a hundred microseconds, the coupling between the ^{13}C nuclear spins can be neglected. The decoherence mechanism is the well-known effect of electron spin echo envelope modulation (ESEEM) [44, 171, 240]: each NV center spin state defines a different direction of the quantization axis for the nuclear spin ($\vec{m}_{0,\pm}$), and a different angular frequency for the nuclear spin precession ($\omega_{0,\pm}$). Therefore, the motion of each nuclear spin is conditioned on the electronic spin state, which leads to the entanglement with the ^{13}C spin bath and to the signal decay. In this case, the signal envelope S_e is a product of contributions of different spins, e.g. for TE protocol:

Since the coupling between the 13C nuclear spins is neglected, below we can consider the evolution of each nuclear spin separately, and omit the index k where it does not lead to confusion.

After appropriate rotation of the nuclear spin coordinate frame, the Hamiltonian of a ^{13}C spin can be written in the form

$$H_n = AS_zI_z + BS_zI_x + \omega_L I_z \tag{B.16}$$

where I_z and I_x are the operators of the nuclear spin components, A and B are the hyperfine coupling constants, and ω_L is the nuclear spin Larmor frequency. As Eq. B.12 shows, decoherence is determined by the overlap between two different evolutions of the ^{13}C spin: one, V_0, is the simple rotation under the action of only the external field. The other is the product of two rotations, first by the angle $\alpha_+ = \omega_+\tau$ around the axis $\vec{m}_+$ (which corresponds to $S_z = +1$), and second by the angle $\alpha_- = \omega_-\tau$ around the axis $\vec{m}_-$ (corresponding to $S_z = 1$). The angular frequencies of the ^{13}C spin precessions are $\omega_\pm = \sqrt{(\omega L \pm A)^2 + B^2}$. The resulting contribution to the TE signal is

$$S_{e1}\cos(\phi-\alpha_+-\alpha_-)+(1-m)\cos\phi\sin\alpha_+\sin\alpha_--(1-m_-^z)\sin\alpha_-\cos\alpha_+\sin\phi-(1-m_+^z)\sin\alpha_+\cos\alpha_-\sin\phi, \tag{B.17}$$

where $\phi = 2\omega L\tau$ (total rotation angle during the period when the NV spin is in the state

$|0\rangle$), the factors $m_{\pm}^z = (\omega L \pm A)/\omega_{\pm}$ are the z-components of the conditional quantization axes $\vec{m}_{\pm}$, and the factor $m = \vec{m}_-\vec{m}_+ = (\omega_L^2 B^2 A^2)/(+)$. For comparison, the contribution from the same ^{13}C spin to the Hahn echo signal is

$$S_{e0} = 1 - 2(m_-^z)^2 \sin^2(\phi/2) \sin^2(\alpha_-/2), \tag{B.18}$$

where $m_-^x = b/\omega$ is the x-component of the conditional quantization axis $\vec{m}_-$.

For a typical NV center spin in medium external fields (10100 G), the spread in the parameters A and B for different nuclear spins is large, and the angles for different ^{13}C spins are effectively randomized between 0 and 2π on the timescale of the ^{13}C Larmor period ($t_L = 2\pi/\omega_L$. Thus, different terms in the expression for the TE signal (Eq. B.17) have almost random phases, and the signal becomes completely decohered on the timescale t_L. At the same time, it is well known [44, 171, 240] that the Hahn echo signal becomes refocused at regular intervals, when $\phi/2$ becomes commensurate with π, and $S_{e0} = 1$ becomes independent of the randomized value of α_-. Note however, that the subsequent revivals of the Hahn echo are different from the initial decay. The initial decay corresponds to the short-time limit of Eq. 20, when $\sin(\alpha_-/2) \approx \alpha_-/2$, and has the approximate form $1 - t^4$. The subsequent revivals correspond to the randomized version of Eq. B.18, when $\sin^2(\alpha/2) = 1/2$, and have the approximate form $1 - t^2$, i.e. they are narrower, but not as steep as the initial decay.

Therefore, the decay of the TE signal almost coincides with the initial decay of the Hahn echo only because the short-time limits of both expressions, Eq. B.17 and B.18, are the same (note that we do not assume smallness of A or B, only small τ):

$$S_e = 1 - \frac{1}{8} B^2 \omega_L^4 \tau^4. \tag{B.19}$$

This similarity, however, does not seem to have deeper physical meaning. The next terms in the short-time expansion are very different, $B^2\omega_L^2(A^2 + B^2 + 3\omega L^2)\tau^6/144$ and $B^2\omega_L^2(A^2 +$

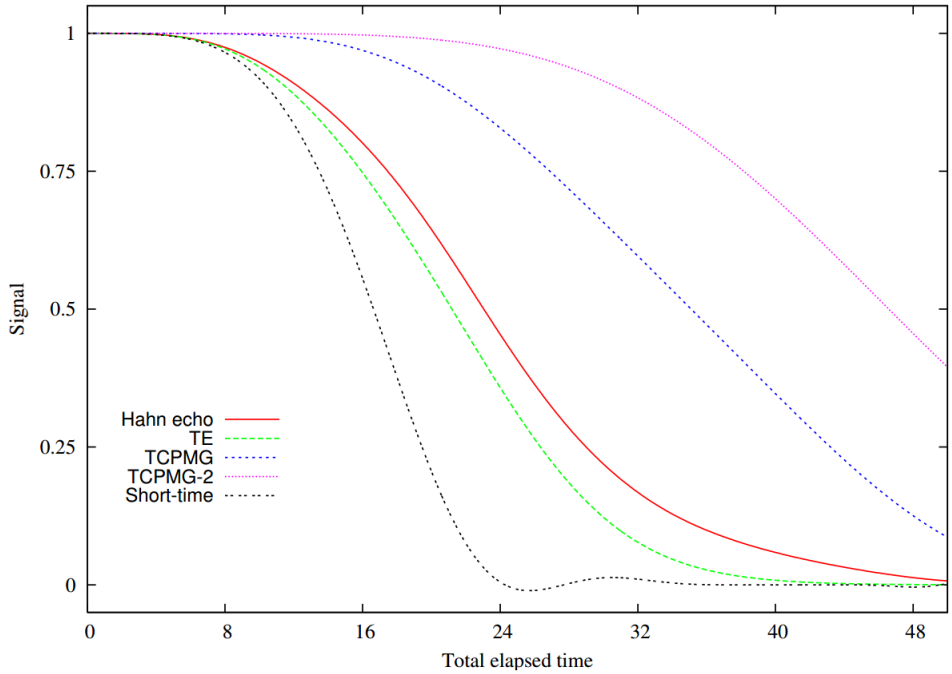

Figure B.1: Simulated decoherence of thermometry protocols at $B = 5\,\mathrm{G}$.

$B^2 2A\omega L + 2\omega L^2)\tau^6/96$. The short-time expression for the symmetrized TCPMG protocol,

$$S_{e2} = 1 - \frac{1}{18} B^2 \omega_L^2 [B^2 + (A + 3\omega_L)^2]\tau^6, \tag{B.20}$$

has a leading order of τ^6, reflecting the better performance expected for symmetrized protocols. These considerations were checked with direct numerical simulations. 1200 ^{13}C spins were randomly placed on a diamond lattice with natural abundance, and the hyperfine coupling constants were calculated assuming only dipole-dipole interactions with the NV center spin. Renormalization of the ^{13}C g-factors [2] was neglected. Fig. B.1 shows the simulated Hahn echo, TE, TCPMG, and TCPMG-2 signal envelopes, and compares them with the short-time approximation for the Hahn Echo and TE. Only small times are shown, since the short-time expression diverges for longer times. Also, at longer times the behavior of the temperature sensing protocols can noticeably vary for different NV centers with different geometrical arrangements of the surrounding ^{13}C nuclei.

B.3 Further considerations for NV center thermometry

B.3.1 Effects of strain, electric fields, and transverse magnetic fields

Our discussion in the main text does not explicitly include the effects of longitudinal or transverse strain on the TE and TCPMG-N sequences. In this work we consider the operation of NV center thermometers in magnetic fields large enough ($B_z \geq 0.5\,\mathrm{G}$) such that transverse strain can be neglected ($|g\mu_B B_z + A_\parallel m_I| >> |\delta|$, where $A_\parallel$ is the parallel hyperfine coefficient, m_I is the spin projection of the nitrogen nuclear spin, and δ is the coupling of the $m_s = +1$ and $m_s = 1$ states induced by transverse strain). Longitudinal strains are more relevant, as they lead to variations in D among NV centers, and should be taken into account by calibrating D for each NV center if absolute thermometry is required. This strain variation is roughly 50 kHz [106], corresponding to a temperature uncertainty on the order of 1 K. For sensing relative temperature shifts, as we focus on here, these strains can be ignored. One alternative possibility for achieving absolute thermometry is through the use of NV center ensembles, such that the response of the ensemble corresponds to the mean value of D. However, in this case the variance of D would limit the achievable coherence times for the ensemble.

Longitudinal and transverse electric fields lead to analogous considerations as longitudinal and transverse strains [64]. Longitudinal electric fields produce relatively small shifts in D of $0.35\,\mathrm{Hz\,cm\,V}^1$[184]. These fields could become important in samples with a large density of optically ionizable impurities, as a fluctuating electric charge located $\approx 20\,\mathrm{nm}$ from an NV center would produce shifts in D relevant for the $\approx 85\,\mu\mathrm{s}$ coherence times observed in the main text. For high purity samples, as considered here, substitutional nitrogen impurities are assumed to be the most common charge traps and are specified to have a concentration less than 5 parts per billion. Similar to transverse strains, transverse electric fields can be neglected for the magnetic fields considered here.

Small magnetic fields transverse to the NV centers symmetry axis (B_T) also produce

apparent shifts in D of magnitude $g\mu_b B_{\mathrm{T}})^2/(2D)$ that must be calibrated for absolute thermometry. For reasonable experimental conditions ($B_{\mathrm{T}} < 5\,\mathrm{G}$) these shifts are smaller than the quoted NV center to NV center variation in D. For sensing relative temperature shifts under such conditions the effects of B_{T} are negligible.

B.3.2 Microwave heating

Another relevant consideration for NV center thermometry is heating caused by absorption of the 2.87 GHz microwaves used for spin manipulation. Although this consideration is particularly relevant for liquid environments given the efficient absorption of microwaves by water, we note that three recent works probing NV center spins in cellular [168] or fluidic [112, 90] environments have provided no mention of heating caused by the CW microwaves utilized for ESR. Thermometry applications will also benefit from the long spin coherence times provided by the TE and TCPMG-N pulse sequences, as in these pulse sequences microwaves are applied for timescales of only $\approx 100\,\mathrm{ns}$ out of $100\,\mu\mathrm{s}$.

B.4 Additional data

As mentioned in the main text, although we observe similar coherence enhancements with the TE and TCPMG-N pulse sequences on different NV centers, we have also observed modulations of the I_{PL} signal as a function of the free evolution time on other NV centers. This variance in response among NV centers is an important consideration for applications and also impacts the use of NV center ensembles for thermometry. Fig. B.2 shows one example for a TE measurement performed on an NV center different from the one discussed in the main text with $B_z \approx 0.5\,\mathrm{G}$. The solid red line is a best fit to the expression

$$I_{\mathrm{PL}}(t) = a \exp\left(-\left(\frac{t}{\tau_{1/e}}\right)^3\right) \cos\left(\omega_1 t + \phi_1\right) \cos\left(\omega_2 t + \phi_2\right) + b, \tag{B.21}$$

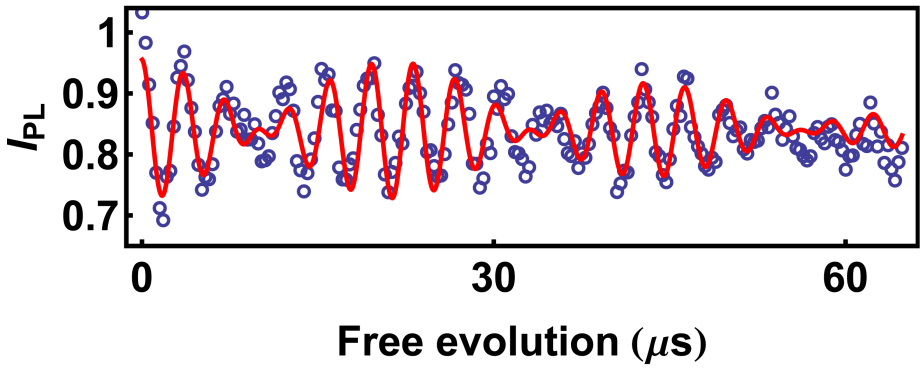

Figure B.2: Thermal echo measurement for an NV center with $B_z \approx 0.5\,\mathrm{G}$. The microwave carrier frequency, Ω_{REF}, was detuned from D by $\approx 0.3\,\mathrm{MHz}$ to induce oscillations in I_{PL} to observe the signal envelope. The solid red line is a best fit to the data with Eq. B.21.

where a, $\tau_{1/e}$, ω_1, ϕ_1, ω_2, ϕ_2, and b are free parameters. For this NV center the inhomogeneous spin lifetime (T_2^*) was $2.4\,\mu\mathrm{s}$. The beating observed in this measurement appears qualitatively similar to features observed in the numerical modeling, suggesting it could be caused by a nearby ^{13}C, however, other possibilities such as the presence of a nearby photoionized impurity must also be considered.

APPENDIX C

ISOLATED ELECTRON SPINS IN SILICON CARBIDE WITH MILLISECOND-COHERENCE TIMES – DETAILS

C.1 Measurements of bulk and single defect photoluminescence

A bulk PL spectrum from the sample irradiated at the highest fluence ($1 \times 10^{15}/\text{cm}^2$) is shown in Fig. C.1. These data were collected using a 14 mm lens instead of an objective, and by focusing the emitted fluorescence into a multimode fiber that is coupled to an InGaAs detector-array spectrometer. Three of the four zero phonon lines associated with neutral divacancies are labeled, but the fourth line from the (hk) defect, which should appear near 1.11 μm, was not observed. Optically detected magnetic resonance measurements in the confocal geometry using the high-NA objective also never showed a luminescent point source having a resonance associated with the (hk) divacancy. The broad PL after the turn-on of our filter, near 1.0 μm, but before the (kh) zero phonon line is not understood, but believed to be a primary component of the background PL observed in our measurements.

To investigate the nature of the background PL as well as to measure the spectrum of a single defect, the same beamsplitter employed for the antibunching measurements is again used to split the PL into separate single mode fibers while the confocal excitation and collection spot is centered on the single (kk) defect presented in the main text. The second fiber is coupled into an InGaAs spectrometer array. The same feedback loop used to maintain the alignment of the apparatus on a single defect for the other measurements in this work is run periodically between 90 s long spectrometer acquisitions. Spectra are repeatedly acquired while on the single (kk) defect with the excitation laser *on*, while on the single (kk) defect with the excitation laser *off*, and while displaced to a dark region containing just background PL approximately 2 μm away with the laser again *on*. These spectra are collected in randomized order to average away any slow fluctuations, and the integrated spectrum collected with the laser off is subtracted from the other two spectra to

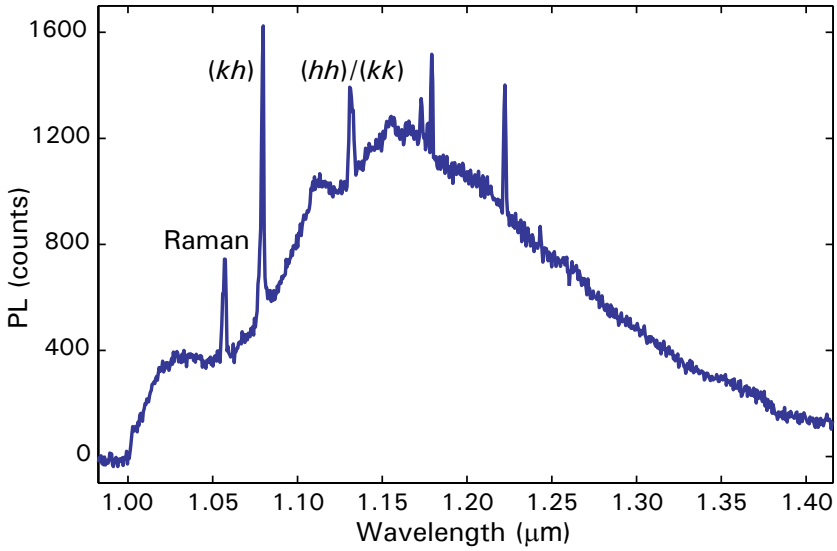

Figure C.1: Bulk photoluminescence spectrum collected on a 4H-SiC sample. PL spectrum collected at $T = 20\,\mathrm{K}$ using a non-confocal geometry from the sample irradiated at the highest fluence of $1 \times 10^{15}/\mathrm{cm}^2$. Zero phonon lines associated with the (hh), (kk), and (kh) defects are labeled. The line labeled "Raman" is the Raman-shifted excitation laser and not a zero phonon line.

remove the detector dark counts, yielding the data plotted in Fig. C.2(a).

The background-only spectrum has a sharp line near 1057 nm that we have confirmed in the past is the Raman-shifted excitation laser, and accounts for about 12% of the total background signal. The broad background above the turn-on edge of the dichroic at 1100 nm (including the small peak near 1079 nm that is a non-ideality of the dichroic filter) has an origin that is less clear. No obvious peaks that might be seen in the phonon sideband of a defect are obvious, but the signal-to-noise ratio is too low to draw a reliable conclusion.

Subtracting the PL of the background from the PL measured on the single defect gives the data plotted in Fig. C.2(b), which shows no Raman peak and no (kh) zero phonon line as expected. These data are corrected using a calibrated white light source to within about 10%. We can calculate a rough approximation of the Debye-Waller factor of $(5.3 \pm 1.1)\%$ by computing the fraction of total PL in the zero phonon line. We also measure time resolved PL from the same single (kk) divacancy acquired by counting the pulses received by the

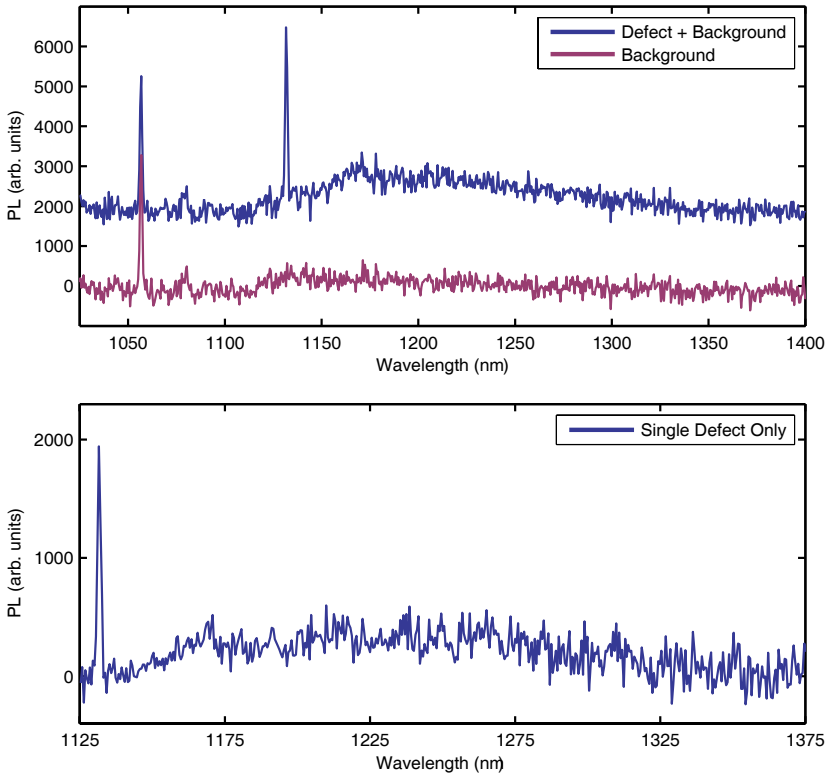

Figure C.2: Confocal photoluminescence spectra. **a**, Spectra collected on and off a single (kk) divacancy. The spectrum collected on the defect is offset by 2000 units for clarity. **b**, Subtracted spectra that show the spectrum of a single (kk) divacancy. The zero-phonon line of the (kk) divacancy PL at 1131 nm is limited by the resolution of our spectrometer.

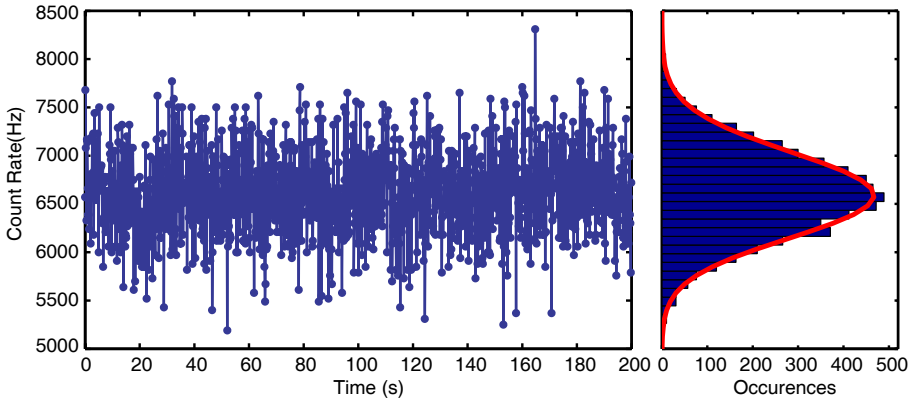

Figure C.3: **Measurement of divacancy photostability.** A time trace of the PL intensity measured by the single photon detector while focused on the single (kk) divacancy. The histogram bins the counts and the maximum likelihood estimate assuming a Poisson distribution is normalized to the histogram height and plotted over it. The single rate parameter Poisson distribution agrees well with the data, further indicating the defect is photostable.

data acquisition card in 30 Hz intervals and scaling these counts by the interval to recover the countrate. The time trace (decimated by a factor of five) along with a histogram of the full dataset acquired over a 200 s period are shown in Fig. C.3. The red curve over the histogram is the maximum likelihood estimate of the density assuming the data follow a Poisson distribution, showing that the defect is photostable. As an additional note, we have never observed any evidence of photoinstability during any measurements of the samples in this work.

C.2 Scaling of Rabi oscillations with applied power

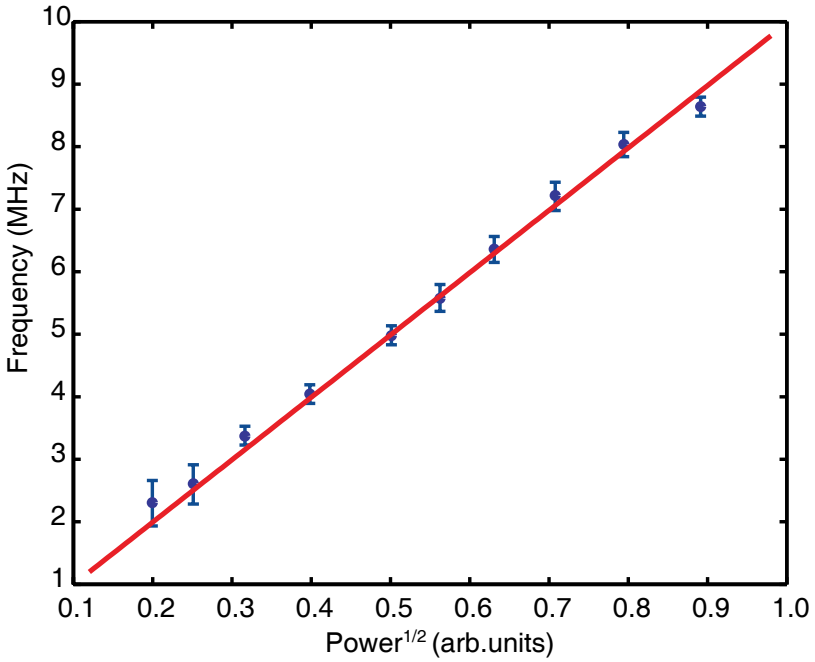

Figure C.4: **Rabi frequency scaling with applied microwave power.** The data are the 95% intervals from fits to separate Rabi oscillation measurements incorporating a 0.26 dB systematic uncertainty in the variable attenuator we use. The red line is a fit to the form $a\sqrt{P}$, where a is a free parameter and P is the applied microwave power in arbitrary units. The nominal powers range from 31.0 dBm to 44.0 dBm at the input of the cryostat. This relationship should be linear and the data agree within the uncertainties.

C.3 Additional data on a single (*kk*) divacancy spin coupled to a nearby nuclear spin

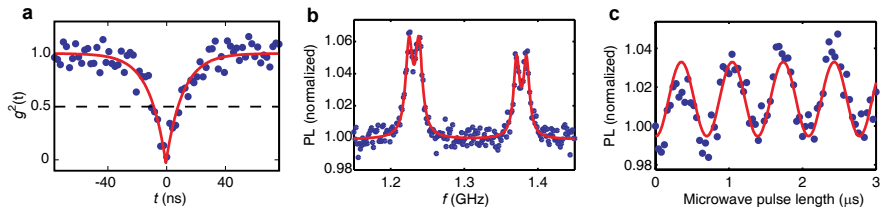

Figure C.5: **Coherent control of a hyperfine-coupled single (*kk*) divacancy spin. a**, Photon antibunching data with $g^2 < 0$, indicating the PL originates from a single defect. **b**, Continuous wave optically detected magnetic resonance near $B = 52\,\mathrm{G}$ showing a 13.4 MHz splitting due to a nearby Si^{29} nuclear spin. **c**, Rabi oscillations from the hyperfine-coupled spin. The oscillations are driven at low power to selectively drive only one of the hyperfine resonances.

C.4 Analysis of photon anti-bunching measurements

Because of surface-related PL, we mostly measured defects that are approximately 20 μm into the sample. At these depths, the background signal was smaller, though still non-negligible at about 40%. The average count rate centered on a defect was measured, as well as the average of the count rate at four points (up, down, left, and right) each displaced approximately 1.2, μm away from the defect but within the same focal plane.

The ideal second order coherence function, $g^2(t)$, is related to the raw counts (including background) from the experiment, $N(t)$, by the relation,

$$g^2(t) = \frac{N(t)/N_{\mathrm{n}} - \left(1-\rho^2\right)}{\rho^2}, \tag{C.1}$$

where N_{n} is a constant that normalizes the raw data to unity at long time delays, and $\rho = S/(S+B)$, where S is the count intensity attributed only to the emitter (signal) and B is the background count intensity[34]. $\rho \approx 0.45$ was typical for the data presented in this work.

The expression for a two-level system, $g^2(t) = 1 - Q \cdot \exp\left(-|t-t_0|/\tau\right)$ was found to have good agreement with our data [25, 24]. Here, t_0 is the "zero delay" time and Q is the depth of the antibunching dip. A value of $Q > 0.5$ means $g^2(t=t_0) < 0.5$, which is indicative of a single emitter. The time constant, τ, is related to the optical lifetime of the defect, τ_0, and the optical pumping rate, r, by $\tau = 1/\left(1/\tau_0 + r\right)$. A more detailed analysis can account for the existence of a third level, similar to the slowly relaxing singlet states in the diamond nitrogen vacancy center, but meaningful inference of those rate parameters requires a more detailed characterization of excitation powers and lifetimes outside the scope of this work.

For small values of ρ like in the present experiments, the background correction defined by Eq. C.1 is very sensitive to the precise value of ρ. For instance, $\rho = 0.4$ will "stretch" the antibunching dip by a factor of about 6.25, while $\rho = 0.5$ will only stretch the dip by about a factor of 4. Small changes, therefore, can produce a dip that goes below zero (non-physical)

or is erroneously above 0.5 when measuring a single defect (a false negative). Moreover, low count rates and high background reduce the signal-to-noise of the measurement, requiring more rebinning of the raw data to make the dip obvious by eye, which distorts the depth of the antibunching dip upward. The re-binned data taken on the isolated divacancies is what is displayed in all figures, but to eliminate the aforementioned issues, we applied a Bayesian approach using Poisson uncertainties on the raw data and normally distributed uncertainties on S and B to infer the parameters Q, τ, t_0, and N_{n}. Using this technique avoids introducing artifacts from rebinning, accurately propagates uncertainties in S and B (which are the components of ρ), and gives consistent point estimates and error bars of Q only in the physical range where $g^2\left(t = t_0\right) \geq 0$. The integrals in Bayesian models are often difficult to calculate analytically and so most practitioners calculate them via a simulation technique called Markov Chain Monte Carlo, which we use here to accomplish this as well[136]. The maximum *a posteriori* probability (MAP) estimate from the simulation was used to generate the fit curves plotted over the data for the three divacancies in the main text and the hyperfine-coupled divacancy in section C.3. The only prior pieces of information incorporated into the model are the values and uncertainties for S and B measured periodically throughout the antibunching measurement, and that Q is bounded between 0 and 1. The highest posterior density (HPD) credible intervals around the MAP value for Q were $Q_{hh} = 0.91^{+0.09}_{-0.10}$, $Q_{kk,\mathrm{hyperfine}} = 0.998^{+0.002}_{-0.21}$, $Q_{kk,\text{no hyperfine}} = 0.92^{+0.08}_{-0.21}$, and $Q_{kh} = 0.99^{+0.01}_{-0.14}$, at the 95% significance level, allowing us to claim with statistical rigor the detection of isolated defects[42].

C.5 Electron spin echo envelope modulation (ESEEM)

The Hahn echo data in Fig. 5.3 are collected using standard two-pulse Hahn-echo sequence readout using optically detected magnetic resonance, namely "`Initialize` - $\pi/2$ - $t_{\mathrm{free}/2}$ - π - $t_{\mathrm{free}/2}$ - `Readout`". For the single-spin Hahn echo measurement in Fig. 5.3b, the initialization and readout steps are a 1.8 μs laser pulse. We collect the first 220 ns of the photons emitted

in the readout pulse. The arbitrary waveform generator used for timing our experiments jumps between sequences where the phase of the final pulse is positive and negative with the same t_{free}, and the measurement software integrates and computes the difference between photons collected in these two sequences.

For the ensemble Hahn-echo measurement in Fig. 5.3c, the initialization step is a 200 μs 975 nm laser pulse, and the readout step consists of a final $\pm\pi/2$-pulse to rotate the spin echo along measurement axis followed by a 50 μs laser pulse for readout. The PL intensity is measured with an InGaAs femtowatt photoreceiver, and a lockin amplifier demodulates the differential signal from the alternating phase of the final $\pi/2$-pulse. The plotted Hahn-echo coherence (C) in both the single-spin and ensemble Hahn-echo measurements is the differential PL intensity normalized such that $C = 1$ at $t = 0$.

The ESEEM data follow the general form,

$$C(t) = e^{-\left(\frac{x}{T_2}\right)^n} \prod_j \left(1 - K_j \sin^2\left(\omega_j t\right)\right)^{N_j},$$

where the ω_j are the relevant ESEEM frequencies, the compressed exponential prefactor represents decoherence, and the K_j and N_j determine the ESEEM shape[184]. For the single-spin data in Fig. 5.3b, two ESEEM frequencies are used: ω_1 and ω_2 are set to be the Larmor precession frequencies of the ^{29}Si and ^{13}C nuclei respectively. The single-spin model fixes $N_1 = N_2 = 1$, and the decoherence term is neglected, since T_2 significantly exceeds the free precession times measured in the single-spin data. For the ensemble Hahn-echo data in Fig. 5.3c, three ESEEM frequencies are used in the fit: ω_1 and ω_2 are set to be the Larmor precession frequencies of the ^{29}Si and ^{13}C nuclei respectively, as before, and ω_3 is left as a fitting parameter that can freely capture more complicated ESEEM dynamics.

This fit yielded $T_2 = (1.2 \pm 0.1)$ ms and $n = (2.0 \pm 0.3)$, as quoted in the main text. The interference term ω_3 is fit to 58.6 kHz, slightly above the ^{29}Si nuclear precession frequency of 58 kHz. Although the origin of this term is not currently understood, it captures the beating

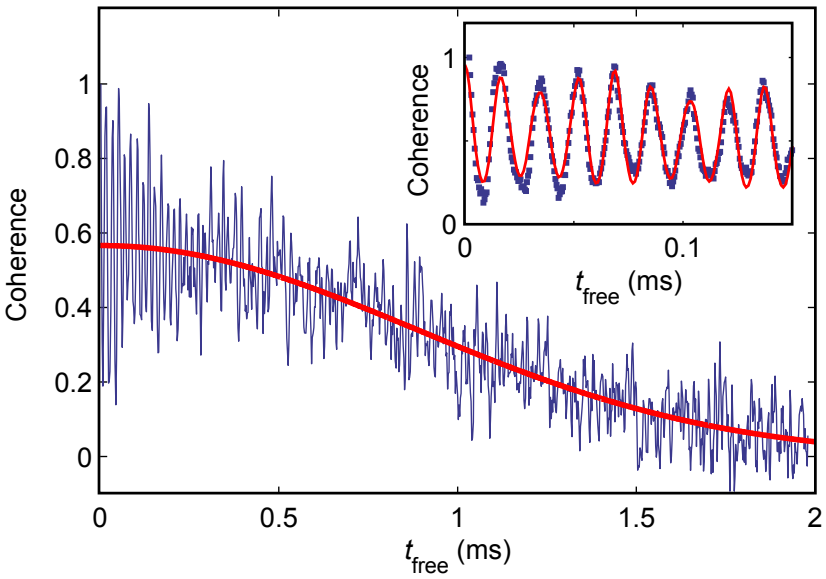

Figure C.6: **Additional ESEEM coherence data on the (*kk*) divacancy ensemble at $T = 20\,\mathrm{K}$ and $B = 116\,\mathrm{G}$.**

effects seen in Fig. 5.3c (i.e. the ESEEM magnitude decaying more quickly than the overall coherence).

In addition to Fig. 5.3c, which presents ensemble Hahn-echo data extending to $t_{\mathrm{free}/2} = 1\,\mathrm{ms}$, we also show Hahn-echo data extending to $t_{\mathrm{free}/2} = 2\,\mathrm{ms}$ in Fig. C.6. For these data, we did not attempt to fit the full ESEEM curve, but rather, we averaged the ESEEM oscillations and simply fit them to a compressed exponentional of the form $e^{-(t_{\mathrm{free}}/T_2)^n}$. In this fit, we find that $T_2 = (1.25 \pm 0.05)\,\mathrm{ms}$, and $n = (2.0 \pm 0.2)$.

BIBLIOGRAPHY

[1] T. A. Abtew, Y. Y. Sun, B.-C. Shih, P. Dev, S. B. Zhang, and P. Zhang. Dynamic jahn-teller effect in the nv^- center in diamond. *Phys. Rev. Lett.*, 107:146403, Sep 2011. doi: 10.1103/PhysRevLett.107.146403.

[2] V. M. Acosta, E. Bauch, A. Jarmola, L. J. Zipp, M. P. Ledbetter, and D. Budker. Broadband magnetometry by infrared-absorption detection of nitrogen-vacancy ensembles in diamond. *Appl. Phys. Lett.*, 97(17):174104, 2010. doi: 10.1063/1.3507884.

[3] V. M. Acosta, E. Bauch, M. P. Ledbetter, A. Waxman, L.-S. Bouchard, and D. Budker. Temperature dependence of the nitrogen-vacancy magnetic resonance in diamond. *Phys. Rev. Lett.*, 104:070801, 2010. doi: 10.1103/PhysRevLett.104.070801.

[4] V. M. Acosta, A. Jarmola, E. Bauch, and D. Budker. Optical properties of the nitrogen-vacancy singlet levels in diamond. *Phys. Rev. B*, 82(20):201202, 2010.

[5] P. Ade, N. Aghanim, C. Armitage-Caplan, M. Arnaud, M. Ashdown, F. Atrio-Barandela, J. Aumont, C. Baccigalupi, A. J. Banday, R. Barreiro, et al. Planck 2013 results. xvi. cosmological parameters. *Astronomy & Astrophysics*, 571:A16, 2014.

[6] H. Aizawa, N. Ohishi, S. Ogawa, E. Watanabe, T. Katsumata, S. Komuro, T. Morikawa, and E. Toba. Characteristics of chromium doped spinel crystals for a fiber-optic thermometer application. *Review of Scientific Instruments*, 73(8):3089–3092, 2002. doi: http://dx.doi.org/10.1063/1.1491998. URL `http://scitation.aip.org/content/aip/journal/rsi/73/8/10.1063/1.1491998`.

[7] P. W. Anderson and J. M. Rowell. Probable observation of the josephson superconducting tunneling effect. *Phys. Rev. Lett.*, 10:230–232, Mar 1963. doi: 10.1103/PhysRevLett.10.230. URL `http://link.aps.org/doi/10.1103/PhysRevLett.10.230`.

[8] M. Ansmann, H. Wang, R. C. Bialczak, M. Hofheinz, E. Lucero, M. Neeley, A. O'Connell, D. Sank, M. Weides, J. Wenner, et al. Violation of bell's inequality in josephson phase qubits. *Nature*, 461(7263):504–506, 2009.

[9] E. J. B. Magnusson. Optical characterization of deep level defects in sic. *Materials Science Forum*, 483-485:341–346, 2005.

[10] T. M. Babinec, B. J. Hausmann, M. Khan, Y. Zhang, J. R. Maze, P. R. Hemmer, and M. Lončar. A diamond nanowire single-photon source. *Nature nanotechnology*, 5(3): 195–199, 2010.

[11] G. Balasubramanian, I. Y. Chan, R. Kolesov, M. Al-Hmoud, J. Tisler, C. Shin, C. Kim, A. Wojcik, P. R. Hemmer, A. Krueger, et al. Nanoscale imaging magnetometry with diamond spins under ambient conditions. *Nature*, 455(7213):648–651, 2008.

[12] G. Balasubramanian, P. Neumann, D. Twitchen, M. Markham, R. Kolesov, N. Mizuochi, J. Isoya, J. Achard, J. Beck, J. Tissler, et al. Ultralong spin coherence time in isotopically engineered diamond. *Nat. Mater.*, 8(5):383–387, 2009.

[13] P. Baranov, I. Ilin, E. Mokhov, M. Muzafarova, S. Orlinskii, and J. Schmidt. Epr identification of the triplet ground state and photoinduced population inversion for a si-c divacancy in silicon carbide. *J. Exper. Theor. Phys. Lett.*, 82(7):441–443, 2005. ISSN 0021-3640. doi: 10.1134/1.2142873. URL `http://dx.doi.org/10.1134/1.2142873`.

[14] P. G. Baranov, A. P. Bundakova, A. A. Soltamova, S. B. Orlinskii, I. V. Borovykh, R. Zondervan, R. Verberk, and J. Schmidt. Silicon vacancy in sic as a promising quantum system for single-defect and single-photon spectroscopy. *Phys. Rev. B*, 83:125203, 2011. doi: 10.1103/PhysRevB.83.125203. URL `http://link.aps.org/doi/10.1103/PhysRevB.83.125203`.

[15] R. Barends, J. Kelly, A. Megrant, A. Veitia, D. Sank, E. Jeffrey, T. White, J. Mutus, A. Fowler, B. Campbell, et al. Superconducting quantum circuits at the surface code threshold for fault tolerance. *Nature*, 508(7497):500–503, 2014.

[16] R. Barends, L. Lamata, J. Kelly, L. García-Álvarez, A. Fowler, A. Megrant, E. Jeffrey, T. White, D. Sank, J. Mutus, et al. Digital quantum simulation of fermionic models with a superconducting circuit. *Nature communications*, 6, 2015.

[17] S. D. Barrett and P. Kok. Efficient high-fidelity quantum computation using matter qubits and linear optics. *Physical Review A*, 71(6):060310, 2005.

[18] A. Batalov, V. Jacques, F. Kaiser, P. Siyushev, P. Neumann, L. Rogers, R. McMurtrie, N. Manson, F. Jelezko, and J. Wrachtrup. Low temperature studies of the excited-state structure of negatively charged nitrogen-vacancy color centers in diamond. *Physical review letters*, 102(19):195506, 2009.

[19] J. S. Bell. On the Problem of Hidden Variables in Quantum Mechanics. *Reviews of Modern Physics*, 38:447–452, July 1966. doi: 10.1103/RevModPhys.38.447.

[20] P. Benioff. Quantum mechanical hamiltonian models of turing machines. *J. Stat. Phys.*, 29(3):515–546, 1982. ISSN 0022-4715. doi: 10.1007/BF01342185. URL `http://dx.doi.org/10.1007/BF01342185`.

[21] C. H. Bennett, G. Brassard, C. Crépeau, R. Jozsa, A. Peres, and W. K. Wootters. Teleporting an unknown quantum state via dual classical and einstein-podolsky-rosen channels. *Phys. Rev. Lett.*, 70:1895–1899, Mar 1993. doi: 10.1103/PhysRevLett.70.1895. URL `http://link.aps.org/doi/10.1103/PhysRevLett.70.1895`.

[22] H. Bernien, L. Childress, L. Robledo, M. Markham, D. Twitchen, and R. Hanson. Two-photon quantum interference from separate nitrogen vacancy centers in diamond. *Physical Review Letters*, 108(4):043604, 2012.

[23] H. Bernien, B. Hensen, W. Pfaff, G. Koolstra, M. S. Blok, L. Robledo, T. H. Taminiau, M. Markham, D. J. Twitchen, L. Childress, and R. Hanson. Heralded entanglement between solid-state qubits separated by three metres. *Nature*, 497:86–90, 2013. doi: 10.1038/nature12016.

[24] A. Beveratos, R. Brouri, T. Gacoin, J.-P. Poizat, and P. Grangier. Nonclassical radiation from diamond nanocrystals. *Physical Review A*, 64(6):061802, 2001.

[25] A. Beveratos, S. Kühn, R. Brouri, T. Gacoin, J.-P. Poizat, and P. Grangier. Room temperature stable single-photon source. *The European Physical Journal D-Atomic, Molecular, Optical and Plasma Physics*, 18(2):191–196, 2002.

[26] M. Bhatnagar and B. J. Baliga. Comparison of 6h-sic, 3c-sic, and si for power devices. *Electron Devices, IEEE Transactions on*, 40(3):645–655, 1993.

[27] A. Bielecki and D. P. Burum. Temperature dependence of 207pb mas spectra of solid lead nitrade. an accurate, sensitive thermometer for variable-temperature mas. *J. Magn. Reson.*, 116(2):215–220, 1995.

[28] R. Blatt and D. Wineland. Entangled states of trapped atomic ions. *Nature*, 453 (7198):1008–1015, 2008.

[29] P. Bloch, W. Brocklesby, R. Harley, and M. Henderson. Effects of microwave excitation on spectral hole-burning in colour centre systems. *Le Journal de Physique Colloques*, 46(C7):C7–527, 1985.

[30] P. E. Blöchl. Projector augmented-wave method. *Phys. Rev. B*, 50:17953–17979, Dec 1994. doi: 10.1103/PhysRevB.50.17953.

[31] V. Y. Bratus, R. Melnik, S. Okulov, V. Rodionov, B. Shanina, and M. Smoliy. A new spin one defect in cubic sic. *Physica B: Condensed Matter*, 404(23):4739–4741, 2009.

[32] G. L. Bretthorst, W. C. Hutton, J. R. Garbow, and J. J. H. Ackerman. Exponential parameter estimation (in nmr) using bayesian probability theory. *Concept. Magn. Reson. A*, 27(2):55–63, 2005.

[33] C. D. Brites, P. P. Lima, N. J. Silva, A. Millán, V. S. Amaral, F. Palacio, and L. D. Carlos. Thermometry at the nanoscale. *Nanoscale*, 4(16):4799–4829, 2012.

[34] R. Brouri, A. Beveratos, J.-P. Poizat, and P. Grangier. Photon antibunching in the fluorescence of individual color centers in diamond. *Optics letters*, 25(17):1294–1296, 2000.

[35] B. B. Buckley, G. D. Fuchs, L. C. Bassett, and D. D. Awschalom. Spin-light coherence for single-spin measurement and control in diamond. *Science*, 330(6008):1212, 2010.

[36] G. Calusine, A. Politi, and D. D. Awschalom. Silicon carbide photonic crystal cavities with integrated color centers. *Applied Physics Letters*, 105(1):011123, 2014.

[37] G. Calusine, A. Politi, and D. D. Awschalom. Cavity-enhanced measurements of defect spins in silicon carbide. *arXiv preprint arXiv:1510.02202*, 2015.

[38] J. Cardenas, M. Zhang, C. T. Phare, S. Y. Shah, C. B. Poitras, B. Guha, and M. Lipson. High q sic microresonators. *Optics express*, 21(14):16882–16887, 2013.

[39] W. Carlos, E. Glaser, and B. Shanabrook. Optical and magnetic resonance signatures of deep levels in semi-insulating 4h sic. *Physica B: Condensed Matter*, 340342:151 – 155, 2003. ISSN 0921-4526. doi: http://dx.doi.org/10.1016/j.physb.2003.09.048. Proceedings of the 22nd International Conference on Defects in Semiconductors.

[40] W. E. Carlos, N. Y. Garces, E. R. Glaser, and M. A. Fanton. Annealing of multivacancy defects in 4h-sic. *Phys. Rev. B*, 74:235201, 2006. doi: 10.1103/PhysRevB.74.235201. URL `http://link.aps.org/doi/10.1103/PhysRevB.74.235201`.

[41] S. Castelletto, B. C. Johnson, V. Ivady, N. Stavrias, T. Umeda, A. Gali, and T. Ohshima. A silicon carbide room-temperature single-photon source. *Nat. Mater.*, 13:151–156, 2014. doi: 10.1038/nmat3806.

[42] M. H. Chen and Q. M. Shao. Monte carlo estimation of bayesian credible and hpd intervals. *J. Comput. Graph. Stat.*, pages 69–92, 1999.

[43] X.-D. Chen, C.-H. Dong, F.-W. Sun, C.-L. Zou, J.-M. Cui, Z.-F. Han, and G.-C. Guo. Temperature dependent energy level shifts of nitrogen-vacancy centers in diamond. *Appl. Phys. Lett.*, 99(16):161903, 2011. doi: 10.1063/1.3652910.

[44] L. Childress, M. G. Dutt, J. Taylor, A. Zibrov, F. Jelezko, J. Wrachtrup, P. Hemmer, and M. Lukin. Coherent dynamics of coupled electron and nuclear spin qubits in diamond. *Science*, 314(5797):281–285, 2006.

[45] I. Chiorescu, P. Bertet, K. Semba, Y. Nakamura, C. Harmans, and J. Mooij. Coherent dynamics of a flux qubit coupled to a harmonic oscillator. *Nature*, 431(7005):159–162, 2004.

[46] D. J. Christle, A. L. Falk, P. Andrich, P. V. Klimov, J. U. Hasan, N. T. Son, E. Janzén, T. Ohshima, , and D. D. Awschalom. Isolated electron spins in silicon carbide with millisecond coherence times. *Nat. Mater.*, 14:160–163, 2015. doi: 10.1038/nmat4144.

[47] Y. Chu, N. De Leon, B. Shields, B. Hausmann, R. Evans, E. Togan, M. Burek, M. Markham, A. Stacey, A. Zibrov, et al. Coherent optical transitions in implanted nitrogen vacancy centers. *Nano letters*, 14(4):1982–1986, 2014.

[48] C. Clark and C. Norris. Photoluminescence associated with the 1.673, 1.944 and 2.498 ev centres in diamond. *Journal of Physics C: Solid State Physics*, 4(14):2223, 1971.

[49] A. T. Collins, M. F. Thomaz, and M. I. B. Jorge. Luminescence decay time of the 1.945 ev centre in type ib diamond. *J. Phys. C.*, 16:2177, 1983.

[50] A. Córcoles, E. Magesan, S. J. Srinivasan, A. W. Cross, M. Steffen, J. M. Gambetta, and J. M. Chow. Demonstration of a quantum error detection code using a square lattice of four superconducting qubits. *Nature communications*, 6, 2015.

[51] D. G. Cory, A. F. Fahmy, and T. F. Havel. Ensemble quantum computing by nmr spectroscopy. *Proceedings of the National Academy of Sciences*, 94(5):1634–1639, 1997.

[52] G. Davies and M. F. Hamer. Optical studies of the 1.945 ev vibronic band in diamond. *Proc. Roy. Soc. Lond. A Math. Phys. Sci.*, 348(1653):pp. 285–298, 1976. ISSN 00804630. URL http://www.jstor.org/stable/79142.

[53] G. De Lange, Z. Wang, D. Riste, V. Dobrovitski, and R. Hanson. Universal dynamical decoupling of a single solid-state spin from a spin bath. *Science*, 330(6000):60–63, 2010.

[54] D. Deutsch. Quantum theory, the church-turing principle and the universal quantum computer. *Proc. Roy. Soc. Lond. A*, 400(1818):97–117, 1985. ISSN 0080-4630. doi: 10.1098/rspa.1985.0070.

[55] D. Deutsch and R. Jozsa. Rapid Solution of Problems by Quantum Computation. *Proceedings of the Royal Society of London Series A*, 439:553–558, Dec. 1992. doi: 10.1098/rspa.1992.0167.

[56] M. H. Devoret, A. Wallraff, and J. M. Martinis. Superconducting qubits: A short review. *arXiv preprint cond-mat/0411174*, 2004.

[57] B. Di Bartolo and X. Chen. *Advances in nonradiative processes in solids*, volume 249. Plenum Publishing Corporation, 1991.

[58] L. DiCarlo, J. Chow, J. Gambetta, L. S. Bishop, B. Johnson, D. Schuster, J. Majer, A. Blais, L. Frunzio, S. Girvin, et al. Demonstration of two-qubit algorithms with a superconducting quantum processor. *Nature*, 460(7252):240–244, 2009.

[59] W. Diffie and M. E. Hellman. New directions in cryptography. *Information Theory, IEEE Transactions on*, 22(6):644–654, 1976.

[60] D. P. DiVincenzo et al. The physical implementation of quantum computation. *arXiv preprint quant-ph/0002077*, 2000.

[61] V. V. Dobrovitski, A. E. Feiguin, D. D. Awschalom, and R. Hanson. Decoherence dynamics of a single spin versus spin ensemble. *Phys. Rev. B*, 77:245212, 2008. doi: 10.1103/PhysRevB.77.245212. URL http://link.aps.org/doi/10.1103/PhysRevB.77.245212.

[62] M. W. Doherty, N. B. Manson, P. Delaney, and L. C. L. Hollenberg. The negatively charged nitrogen-vacancy centre in diamond: the electronic solution. *New J. Phys.*, 13 (2):025019, 2011. URL http://stacks.iop.org/1367-2630/13/i=2/a=025019.

[63] M. W. Doherty, N. B. Manson, P. Delaney, F. Jelezko, J. Wrachtrup, and L. C. Hollenberg. The nitrogen-vacancy colour centre in diamond. *Physics Reports*, 528(1):1–45, 2013.

[64] F. Dolde, H. Fedder, M. Doherty, T. Nobauer, F. Rempp, G. Balasubramanian, T. Wolf, F. Reinhard, L. Hollenberg, F. Jelezko, , and J. Wrachtrup. A silicon carbide room-temperature single-photon source. *Nat. Phys.*, 7:459–463, 2011. doi: 10.1038/nphys1969.

[65] F. Dolde, H. Fedder, M. W. Doherty, T. Nöbauer, F. Rempp, G. Balasubramanian, T. Wolf, F. Reinhard, L. Hollenberg, F. Jelezko, et al. Electric-field sensing using single diamond spins. *Nat. Phys.*, 7(6):459–463, 2011.

[66] F. Dolde, I. Jakobi, B. Naydenov, N. Zhao, S. Pezzagna, C. Trautmann, J. Meijer, P. Neumann, F. Jelezko, and J. Wrachtrup. Room-temperature entanglement between single defect spins in diamond. *Nat. Phys.*, 9:193–143, 2013. doi: 10.1038/nphys2545.

[67] J. S. Donner, S. A. Thompson, M. P. Kreuzer, G. Baffou, and R. Quidant. Mapping intracellular temperature using green fluorescent protein. *Nano letters*, 12(4):2107–2111, 2012.

[68] A. Dréau, M. Lesik, L. Rondin, P. Spinicelli, O. Arcizet, J.-F. Roch, and V. Jacques. Avoiding power broadening in optically detected magnetic resonance of single nv defects for enhanced dc magnetic field sensitivity. *Phys. Rev. B*, 84:195204, Nov 2011. doi: 10.1103/PhysRevB.84.195204.

[69] L. DuPreez. *Electron paramagnetic resonance and optical investigations of defect centres in diamond*. PhD thesis, University of the Witwatersrand, Johannesburg, 1965.

[70] M. V. Dutt, L. Childress, L. Jiang, E. Togan, J. Maze, F. Jelezko, A. S. Zibrov, P. R. Hemmer, and M. D. Lukin. Quantum register based on individual electronic and nuclear spin qubits in diamond. *Science*, 316(5829):1312, 2007.

[71] R. J. Epstein, F. M. Mendoza, Y. K. Kato, and D. D. Awschalom. Anisotropic interactions of a single spin and dark-spin spectroscopy in diamond. *Nat. Phys.*, 1(2): 94–98, 2005.

[72] A. L. Falk, B. B. Buckley, G. Calusine, W. F. Koehl, V. V. Dobrovitski, A. Politi, C. A. Zorman, P. X.-L. Feng, and D. D. Awschalom. Polytype control of spin qubits in silicon carbide. *Nature Comm.*, 4(1819), 2013. doi: 10.1038/nature10562.

[73] A. L. Falk, P. V. Klimov, B. B. Buckley, V. Ivády, I. A. Abrikosov, G. Calusine, W. F. Koehl, A. Gali, and D. D. Awschalom. Electrically and mechanically tunable electron spins in silicon carbide color centers. *Phys. Rev. Lett.*, 112:187601, 2014. doi: 10.1103/PhysRevLett.112.187601. URL `http://link.aps.org/doi/10.1103/PhysRevLett.112.187601`.

[74] A. L. Falk, P. V. Klimov, V. Ivády, K. Szász, D. J. Christle, W. F. Koehl, A. Gali, and D. D. Awschalom. Optical polarization of nuclear spins in silicon carbide. *Phys. Rev. Lett.*, 114:247603, 2015. doi: 10.1103/PhysRevLett.114.247603. URL `http://link.aps.org/doi/10.1103/PhysRevLett.114.247603`.

[75] K. Fang, V. M. Acosta, C. Santori, Z. Huang, K. M. Itoh, H. Watanabe, S. Shikata, and R. G. Beausoleil. High-sensitivity magnetometry based on quantum beats in diamond nitrogen-vacancy centers. *Physical review letters*, 110(13):130802, 2013.

[76] A. Faraon, P. E. Barclay, C. Santori, K.-M. C. Fu, and R. G. Beausoleil. Resonant enhancement of the zero-phonon emission from a colour centre in a diamond cavity. *Nature Photonics*, 5(5):301–305, 2011.

[77] A. Faraon, C. Santori, Z. Huang, V. M. Acosta, and R. G. Beausoleil. Coupling of nitrogen-vacancy centers to photonic crystal cavities in monocrystalline diamond. *Physical review letters*, 109(3):033604, 2012.

[78] R. Feynman. Simulating physics with computers. *Inter. J. Theor. Phys.*, 21(6-7):467–488, 1982. ISSN 0020-7748. doi: 10.1007/BF02650179. URL `http://dx.doi.org/10.1007/BF02650179`.

[79] S. L. Firebaugh, K. F. Jensen, and M. A. Schmidt. Investigation of high-temperature degradation of platinum thin films with an in situ resistance measurement apparatus. *J. Microelectromech. S.*, 7(1):128–135, 1998.

[80] A. G. Fowler, A. M. Stephens, and P. Groszkowski. High-threshold universal quantum computation on the surface code. *Phys. Rev. A*, 80:052312, Nov 2009. doi: 10.1103/PhysRevA.80.052312. URL `http://link.aps.org/doi/10.1103/PhysRevA.80.052312`.

[81] A. G. Fowler, M. Mariantoni, J. M. Martinis, and A. N. Cleland. Surface codes: Towards practical large-scale quantum computation. *Phys. Rev. A*, 86:032324, Sep 2012. doi: 10.1103/PhysRevA.86.032324.

[82] K.-M. C. Fu, C. Santori, P. E. Barclay, L. J. Rogers, N. B. Manson, and R. G. Beausoleil. Observation of the dynamic jahn-teller effect in the excited states of nitrogen-vacancy centers in diamond. *Proc. SPIE*, 7611:761108, 2010. doi: 10.1117/12.843827.

[83] G. D. Fuchs, V. V. Dobrovitski, D. M. Toyli, F. J. Heremans, and D. D. Awschalom. Gigahertz dynamics of a strongly driven single quantum spin. *Science*, 326(5959):1520, 2009.

[84] G. D. Fuchs, G. Burkard, P. V. Klimov, and D. D. Awschalom. A quantum memory intrinsic to single nitrogen-vacancy centres in diamond. *Nature Physics*, 7(10):789–793, 2011.

[85] G. D. Fuchs, A. L. Falk, V. V. Dobrovitski, and D. D. Awschalom. Spin coherence during optical excitation of a single nitrogen-vacancy center in diamond. *Phys. Rev. Lett.*, 108:157602, 2012. doi: 10.1103/PhysRevLett.108.157602. URL `http://link.aps.org/doi/10.1103/PhysRevLett.108.157602`.

[86] A. Gali. Time-dependent density functional study on the excitation spectrum of point defects in semiconductors. *Phys. Stat. Solid. B*, 248(6): 1337–1346, 2011. ISSN 1521-3951. doi: 10.1002/pssb.201046254. URL `http://dx.doi.org/10.1002/pssb.201046254`.

[87] A. Gali, M. Fyta, and E. Kaxiras. Ab initio supercell calculations on nitrogen-vacancy center in diamond: Electronic structure and hyperfine tensors. *Phys. Rev. B*, 77:155206, 2008. doi: 10.1103/PhysRevB.77.155206. URL `http://link.aps.org/doi/10.1103/PhysRevB.77.155206`.

[88] A. Gali, E. Janzén, P. Deák, G. Kresse, and E. Kaxiras. Theory of spin-conserving excitation of the $n - V^-$ center in diamond. *Phys. Rev. Lett.*, 103:186404, Oct 2009. doi: 10.1103/PhysRevLett.103.186404.

[89] A. Gali, A. Gällström, N. T. Son, and E. Janzén. Theory of neutral divacancy in sic: a defect for spintronics. In *Materials Science Forum*, volume 645, pages 395–397, 2010.

[90] M. Geiselmann, M. L. Juan, J. Renger, J. M. Say, L. J. Brown, F. J. G. De Abajo, F. Koppens, and R. Quidant. Three-dimensional optical manipulation of a single electron spin. *Nature nanotechnology*, 8(3):175–179, 2013.

[91] A. Gelman and D. B. Rubin. Inference from iterative simulation using multiple sequences. *Stat. Sci.*, 7(4):457–472, 1992.

[92] J. P. Goss, R. Jones, S. J. Breuer, P. R. Briddon, and S. Öberg. The twelve-line 1.682 ev luminescence center in diamond and the vacancy-silicon complex. *Phys. Rev. Lett.*, 77:3041–3044, Sep 1996. doi: 10.1103/PhysRevLett.77.3041.

[93] C. Gota, K. Okabe, T. Funatsu, Y. Harada, and S. Uchiyama. Hydrophilic fluorescent nanogel thermometer for intracellular thermometry. *Journal of the American Chemical Society*, 131(8):2766–2767, 2009.

[94] K. T. Grattan and Z. Y. Zhang. *Fiber optic fluorescence thermometry*, volume 2. Springer Science & Business Media, 1995.

[95] M. S. Grinolds, S. Hong, P. Maletinsky, L. Luan, M. D. Lukin, R. L. Walsworth, and A. Yacoby. Nanoscale magnetic imaging of a single electron spin under ambient conditions. *Nature Physics*, 9(4):215–219, 2013.

[96] L. K. Grover. A fast quantum mechanical algorithm for database search. In *Proceedings of the Twenty-eighth Annual ACM Symposium on Theory of Computing*, STOC '96, pages 212–219, 1996. ISBN 0-89791-785-5. doi: 10.1145/237814.237866.

[97] A. Gruber, A. Dräbenstedt, C. Tietz, L. Fleury, J. Wrachtrup, and C. Borczyskowski. Scanning confocal optical microscopy and magnetic resonance on single defect centers. *Science*, 276(5321):2012, 1997.

[98] J. P. Hadden, J. P. Harrison, A. C. Stanley-Clarke, L. Marseglia, Y. L. D. Ho, B. R. Patton, J. L. OBrien, and J. G. Rarity. Strongly enhanced photon collection from diamond defect centers under microfabricated integrated solid immersion lenses. *Appl. Phys. Lett.*, 97:241901, 2010.

[99] U. Haeberlen. *Advances in magnetic resonance*. Academic Press, New York, 1976.

[100] R. Harley, M. Henderson, and R. Macfarlane. Persistent spectral hole burning of colour centres in diamond. *Journal of Physics C: Solid State Physics*, 17(8):L233, 1984.

[101] J. Harrison, M. Sellars, and N. Manson. Measurement of the optically induced spin polarisation of nv centres in diamond. *Diam. Relat. Mater.*, 15(48):586 – 588, 2006. ISSN 0925-9635.

[102] T. P. Harty, D. T. C. Allcock, C. J. Ballance, L. Guidoni, H. A. Janacek, N. M. Linke, D. N. Stacey, and D. M. Lucas. High-fidelity preparation, gates, memory, and readout of a trapped-ion quantum bit. *Phys. Rev. Lett.*, 113:220501, Nov 2014. doi: 10.1103/PhysRevLett.113.220501. URL `http://link.aps.org/doi/10.1103/PhysRevLett.113.220501`.

[103] J. Hassan, J. Bergman, A. Henry, and E. Janzén. On-axis homoepitaxial growth on si-face 4h–sic substrates. *Journal of Crystal Growth*, 310(20):4424–4429, 2008.

[104] B. Hensen, H. Bernien, A. Dréau, A. Reiserer, N. Kalb, M. Blok, J. Ruitenberg, R. Vermeulen, R. Schouten, C. Abellán, et al. Loophole-free bell inequality violation using electron spins separated by 1.3 kilometres. *Nature*, 526(7575):682–686, 2015.

[105] J. Heyd, G. E. Scuseria, and M. Ernzerhof. Hybrid functionals based on a screened coulomb potential. *The Journal of Chemical Physics*, 118(18):8207–8215, 2003.

[106] J. S. Hodges, N. Yao, D. Maclaurin, C. Rastogi, M. Lukin, and D. Englund. Timekeeping with electron spin states in diamond. *Physical Review A*, 87(3):032118, 2013.

[107] K. Holliday, X.-F. He, P. T. Fisk, and N. B. Manson. Raman heterodyne detection of electron paramagnetic resonance. *Optics letters*, 15(17):983–985, 1990.

[108] K. Holmström and J. Petersson. A review of the parameter estimation problem of fitting positive exponential sums to empirical data. *Appl. Math. Comput.*, 126(1): 31–61, 2002.

[109] C. K. Hong, Z. Y. Ou, and L. Mandel. Measurement of subpicosecond time intervals between two photons by interference. *Phys. Rev. Lett.*, 59:2044–2046, Nov 1987. doi: 10.1103/PhysRevLett.59.2044. URL `http://link.aps.org/doi/10.1103/PhysRevLett.59.2044`.

[110] S. Hong, M. S. Grinolds, L. M. Pham, D. Le Sage, L. Luan, R. L. Walsworth, and A. Yacoby. Nanoscale magnetometry with nv centers in diamond. *MRS bulletin*, 38 (02):155–161, 2013.

[111] M. Horodecki, P. Horodecki, and R. Horodecki. Separability of mixed states: necessary and sufficient conditions. *Phys. Lett. A*, 223(12):1 – 8, 1996. ISSN 0375-9601. doi: http://dx.doi.org/10.1016/S0375-9601(96)00706-2. URL `http://www.sciencedirect.com/science/article/pii/S0375960196007062`.

[112] V. R. Horowitz, B. J. Alemán, D. J. Christle, A. N. Cleland, and D. D. Awschalom. Electron spin resonance of nitrogen-vacancy centers in optically trapped nanodiamonds. *Proceedings of the National Academy of Sciences*, 109(34):13493–13497, 2012.

[113] V. Jacques, P. Neumann, J. Beck, M. Markham, D. Twitchen, J. Meijer, F. Kaiser, G. Balasubramanian, F. Jelezko, and J. Wrachtrup. Dynamic polarization of single nuclear spins by optical pumping of nitrogen-vacancy color centers in diamond at room temperature. *Phys. Rev. Lett.*, 102(5):57403, 2009.

[114] K. Jahnke, B. Naydenov, T. Teraji, S. Koizumi, T. Umeda, J. Isoya, and F. Jelezko. Long coherence time of spin qubits in 12c enriched polycrystalline chemical vapor deposition diamond. *Applied physics letters*, 101(1):012405, 2012.

[115] D. Jaque and F. Vetrone. Luminescence nanothermometry. *Nanoscale*, 4(15):4301–4326, 2012.

[116] F. Jelezko and J. Wrachtrup, 2012. private communication.

[117] F. Jelezko, I. Popa, A. Gruber, C. Tietz, J. Wrachtrup, A. Nizovtsev, and S. Kilin. Single spin states in a defect center resolved by optical spectroscopy. *Applied physics letters*, 81(12):2160–2162, 2002.

[118] F. Jelezko, T. Gaebel, I. Popa, A. Gruber, and J. Wrachtrup. Observation of coherent oscillations in a single electron spin. *Phys. Rev. Lett.*, 92(7):76401, 2004.

[119] V. Jokubavicius, G. R. Yazdi, R. Liljedahl, I. G. Ivanov, J. Sun, X. Liu, P. Schuh, M. Wilhelm, P. Wellmann, R. Yakimova, et al. Single domain 3c-sic growth on off-oriented 4h-sic substrates. *Crystal Growth & Design*, 15(6):2940–2947, 2015.

[120] B. D. Josephson. Possible new effects in superconductive tunnelling. *Physics letters*, 1(7):251–253, 1962.

[121] H. Kato, M. Wolfer, C. Schreyvogel, M. Kunzer, W. Müller-Sebert, H. Obloh, S. Yamasaki, and C. Nebel. Tunable light emission from nitrogen-vacancy centers in single crystal diamond pin diodes. *Applied Physics Letters*, 102(15):151101, 2013.

[122] G. Keiser. *Optical fiber communications*. Wiley Online Library, 2003.

[123] J. Kelly, R. Barends, A. G. Fowler, A. Megrant, E. Jeffrey, T. C. White, D. Sank, J. Y. Mutus, B. Campbell, Y. Chen, Z. Chen, B. Chiaro, A. Dunsworth, I.-C. Hoi, C. Neill, P. J. J. O/'Malley, C. Quintana, P. Roushan, A. Vainsencher, J. Wenner, A. N. Cleland, and J. M. Martinis. State preservation by repetitive error detection in a superconducting quantum circuit. *Nature*, 519(7541):66–69, Mar 2015. ISSN 0028-0836. Letter.

[124] P. V. Klimov. *Quantum information processing with electronic and nuclear spins in semiconductors*. PhD thesis, THE UNIVERSITY OF CHICAGO, 2016.

[125] P. V. Klimov, A. L. Falk, B. B. Buckley, and D. D. Awschalom. Electrically driven spin resonance in silicon carbide color centers. *Phys. Rev. Lett.*, 112:087601, 2014. doi: 10.1103/PhysRevLett.112.087601. URL http://link.aps.org/doi/10.1103/PhysRevLett.112.087601.

[126] P. V. Klimov, A. L. Falk, D. J. Christle, V. V. Dobrovitski, and D. D. Awschalom. Quantum entanglement at ambient conditions in a macroscopic solid-state spin ensemble. *Science advances*, 1(10):e1501015, 2015.

[127] E. Knill, R. Laflamme, and G. J. Milburn. A scheme for efficient quantum computation with linear optics. *nature*, 409(6816):46–52, 2001.

[128] J. Koch, T. M. Yu, J. Gambetta, A. A. Houck, D. I. Schuster, J. Majer, A. Blais, M. H. Devoret, S. M. Girvin, and R. J. Schoelkopf. Charge-insensitive qubit design derived from the cooper pair box. *Phys. Rev. A*, 76:042319, Oct 2007. doi: 10.1103/PhysRevA.76.042319. URL http://link.aps.org/doi/10.1103/PhysRevA.76.042319.

[129] W. F. Koehl, B. B. Buckley, F. J. Heremans, G. Calusine, and D. D. Awschalom. Room temperature coherent control of defect spin qubits in silicon carbide. *Nature*, 477:84–87, 2011. doi: 10.1038/nature10562.

[130] P. Kok, W. J. Munro, K. Nemoto, T. C. Ralph, J. P. Dowling, and G. J. Milburn. Linear optical quantum computing with photonic qubits. *Rev. Mod. Phys.*, 79:135–174, Jan 2007. doi: 10.1103/RevModPhys.79.135. URL http://link.aps.org/doi/10.1103/RevModPhys.79.135.

[131] A. Kossakowski. On quantum statistical mechanics of non-hamiltonian systems. *Rep. Math. Phys.*, 3(4):247–274, 1972.

[132] H. Kraus, V. Soltamov, D. Riedel, S. Väth, F. Fuchs, A. Sperlich, P. Baranov, V. Dyakonov, and G. Astakhov. Room-temperature quantum microwave emitters based on spin defects in silicon carbide. *Nature Physics*, 10(2):157–162, 2014.

[133] G. Kresse and J. Furthmüller. Efficient iterative schemes for ab initio total-energy calculations using a plane-wave basis set. *Phys. Rev. B*, 54:11169–11186, 1996. doi: 10.1103/PhysRevB.54.11169. URL http://link.aps.org/doi/10.1103/PhysRevB.54.11169.

[134] G. Kresse and D. Joubert. From ultrasoft pseudopotentials to the projector augmented-wave method. *Phys. Rev. B*, 59:1758–1775, Jan 1999. doi: 10.1103/PhysRevB.59.1758. URL http://link.aps.org/doi/10.1103/PhysRevB.59.1758.

[135] G. Kucsko, P. C. Maurer, N. Y. Yao, M. Kubo, H. J. Noh, P. K. Lo, H. Park, and M. D. Lukin. Nanometre scale thermometry in a living cell. *Nature*, 500:54–58, 2013. doi: 10.1038/nature12373.

[136] E. Laloy and J. A. Vrugt. High-dimensional posterior exploration of hydrologic models using multiple-try dream(zs) and high-performance computing. *Wat. Resour. Res.*, 48(1), 2012. ISSN 1944-7973. doi: 10.1029/2011WR010608. URL `http://dx.doi.org/10.1029/2011WR010608`.

[137] B. Lanyon, M. Barbieri, M. Almeida, and A. White. Experimental quantum computing without entanglement. *Physical review letters*, 101(20):200501, 2008.

[138] J. Y. Lee, X. Lu, Q. Lin, et al. High-q silicon carbide photonic-crystal cavities. *Applied Physics Letters*, 106(4), 2015.

[139] A. Lenef and S. Rand. Electronic structure of the n-v center in diamond: Theory. *Physical Review B*, 53(20):13441, 1996.

[140] A. Lenef and S. Rand. Reply to comment on electronic structure of the n-v center in diamond: Theory. *Physical Review B*, 56(24):16033, 1997.

[141] A. Lenef, S. Brown, D. Redman, S. Rand, J. Shigley, and E. Fritsch. Electronic structure of the n-v center in diamond: Experiments. *Physical Review B*, 53(20): 13427, 1996.

[142] I. N. Levine. *Quantum Chemistry*. Prentice Hall, New Jersey, 1991.

[143] D. A. Lidar and T. A. Brun. *Quantum error correction*. Cambridge University Press, 2013.

[144] C.-M. Lin, Y.-Y. Chen, V. V. Felmetsger, D. G. Senesky, and A. P. Pisano. Aln/3c–sic composite plate enabling high-frequency and high-q micromechanical resonators. *Advanced Materials*, 24(20):2722–2727, 2012.

[145] G. Lindblad. On the generators of quantum dynamical semigroups. *Commun. Math. Phys.*, 48(2):119–130, 1976.

[146] S. Lloyd. Almost any quantum logic gate is universal. *Phys. Rev. Lett.*, 75:346–349, Jul 1995. doi: 10.1103/PhysRevLett.75.346. URL `http://link.aps.org/doi/10.1103/PhysRevLett.75.346`.

[147] S. Lloyd, M. Mohseni, and P. Rebentrost. Quantum algorithms for supervised and unsupervised machine learning. *arXiv preprint arXiv:1307.0411*, 2013.

[148] S. Lloyd, M. Mohseni, and P. Rebentrost. Quantum principal component analysis. *Nature Physics*, 10(9):631–633, 2014.

[149] J. H. N. Loubser and J. A. Van Wyk. Optical spin-polarisation in a triplet state in irrdiated and annealed type 1b diamonds. *Diamond Res.*, 1:11–5, 1977.

[150] J. H. N. Loubser and J. A. Wyk. Electron spin resonance in the study of diamond. *Rep. Prog. Phys.*, 41:1201, 1978.

[151] X. Lu, J. Y. Lee, P. X.-L. Feng, and Q. Lin. High q silicon carbide microdisk resonator. *Applied Physics Letters*, 104(18):181103, 2014.

[152] X. Lu, J. Y. Lee, and Q. Lin. High-frequency and high-quality silicon carbide optomechanical microresonators. *Scientific reports*, 5, 2015.

[153] Y. Ma, M. Rohlfing, and A. Gali. Excited states of the negatively charged nitrogen-vacancy color center in diamond. *Phys. Rev. B*, 81(4):041204, 2010.

[154] E. R. MacQuarrie, T. A. Gosavi, N. R. Jungwirth, S. A. Bhave, and G. D. Fuchs. Mechanical spin control of nitrogen-vacancy centers in diamond. *Phys. Rev. Lett.*, 111:227602, Nov 2013. doi: 10.1103/PhysRevLett.111.227602. URL `http://link.aps.org/doi/10.1103/PhysRevLett.111.227602`.

[155] O. Madelung. *Semiconductors: data handbook*. Springer Science & Business Media, 2012.

[156] H. J. Mamin, M. Kim, M. H. Sherwood, C. T. Rettner, K. Ohno, D. D. Awschalom, and D. Rugar. Nanoscale nuclear magnetic resonance with a nitrogen-vacancy spin sensor. *Science*, 339(6119):557–560, 2013. doi: 10.1126/science.1231540.

[157] N. Manson and C. Wei. Transient hole burning in nv centre in diamond. *Journal of luminescence*, 58(1):158–160, 1994.

[158] N. Manson, L. Rogers, M. Doherty, and L. Hollenberg. Optically induced spin polarisation of the nv-centre in diamond: role of electron-vibration interaction. *Arxiv preprint arXiv:1011.2840*, 2010.

[159] N. B. Manson, X.-F. He, and P. T. Fisk. Raman heterodyne detected electron-nuclear-double-resonance measurements of the nitrogen-vacancy center in diamond. *Optics letters*, 15(19):1094–1096, 1990.

[160] N. B. Manson, X.-F. He, and P. T. Fisk. Raman heterodyne studies of the nitrogen-vacancy centre in diamond. *Journal of luminescence*, 53(1):49–54, 1992.

[161] N. B. Manson, J. P. Harrison, and M. J. Sellars. Nitrogen-vacancy center in diamond: Model of the electronic structure and associated dynamics. *Phys. Rev. B*, 74:104303, Sep 2006. doi: 10.1103/PhysRevB.74.104303. URL `http://link.aps.org/doi/10.1103/PhysRevB.74.104303`.

[162] L. Marseglia, J. P. Hadden, A. C. Stanley-Clarke, J. P. Harrison, B. Patton, Y. L. D. Ho, B. Naydenov, F. Jelezko, J. Meijer, P. R. Dolan, et al. Nanofabricated solid immersion lenses registered to single emitters in diamond. *Appl. Phys. Lett.*, 98:133107, 2011.

[163] J. Martin. Fine structure of excited 3e state in nitrogen-vacancy centre of diamond. *Journal of luminescence*, 81(4):237–247, 1999.

[164] J. M. Martinis, S. Nam, J. Aumentado, and C. Urbina. Rabi oscillations in a large josephson-junction qubit. *Phys. Rev. Lett.*, 89: 117901, Aug 2002. doi: 10.1103/PhysRevLett.89.117901. URL http://link.aps.org/doi/10.1103/PhysRevLett.89.117901.

[165] P. C. Maurer, G. Kucsko, C. Latta, L. Jiang, N. Y. Yao, S. D. Bennett, F. Pastawski, D. Hunger, N. Chisholm, M. Markham, et al. Room-temperature quantum bit memory exceeding one second. *Science*, 336(6086):1283–1286, 2012.

[166] J. Maze, P. Stanwix, J. Hodges, S. Hong, J. Taylor, P. Cappellaro, L. Jiang, M. G. Dutt, E. Togan, A. Zibrov, et al. Nanoscale magnetic sensing with an individual electronic spin in diamond. *Nature*, 455(7213):644–647, 2008.

[167] J. R. Maze, A. Gali, E. Togan, Y. Chu, A. Trifonov, E. Kaxiras, and M. D. Lukin. Properties of nitrogen-vacancy centers in diamond: the group theoretic approach. *New J. Phys.*, 13:025025, 2011.

[168] L. McGuinness, Y. Yan, A. Stacey, D. Simpson, L. Hall, D. Maclaurin, S. Prawer, P. Mulvaney, J. Wrachtrup, F. Caruso, et al. Quantum measurement and orientation tracking of fluorescent nanodiamonds inside living cells. *Nature nanotechnology*, 6(6): 358–363, 2011.

[169] D. M. Meekhof, C. Monroe, B. E. King, W. M. Itano, and D. J. Wineland. Generation of nonclassical motional states of a trapped atom. *Phys. Rev. Lett.*, 76:1796–1799, Mar 1996. doi: 10.1103/PhysRevLett.76.1796. URL http://link.aps.org/doi/10.1103/PhysRevLett.76.1796.

[170] D. J. Meyer, P. M. Lenahan, and A. J. Lelis. Observation of trapping defects in 4h-silicon carbide metal-oxide-semiconductor field-effect transistors by spin-dependent recombination. *Applied Physics Letters*, 86(2), 2005.

[171] W. Mims. Envelope modulation in spin-echo experiments. *Physical Review B*, 5(7): 2409, 1972.

[172] Y. Mita. Change of absorption spectra in type-ib diamond with heavy neutron irradiation. *Physical Review B*, 53(17):11360, 1996.

[173] C. Monroe, D. M. Meekhof, B. E. King, W. M. Itano, and D. J. Wineland. Demonstration of a fundamental quantum logic gate. *Phys. Rev. Lett.*, 75:4714–4717, Dec 1995. doi: 10.1103/PhysRevLett.75.4714. URL http://link.aps.org/doi/10.1103/PhysRevLett.75.4714.

[174] T. Monz, P. Schindler, J. T. Barreiro, M. Chwalla, D. Nigg, W. A. Coish, M. Harlander, W. Hänsel, M. Hennrich, and R. Blatt. 14-qubit entanglement: Creation and coherence. *Phys. Rev. Lett.*, 106:130506, Mar 2011. doi: 10.1103/PhysRevLett.106.130506. URL http://link.aps.org/doi/10.1103/PhysRevLett.106.130506.

[175] J. Mooij, T. Orlando, L. Levitov, L. Tian, C. H. Van der Wal, and S. Lloyd. Josephson persistent-current qubit. *Science*, 285(5430):1036–1039, 1999.

[176] A. Myerson, D. Szwer, S. Webster, D. Allcock, M. Curtis, G. Imreh, J. Sherman, D. Stacey, A. Steane, and D. Lucas. High-fidelity readout of trapped-ion qubits. *Physical Review Letters*, 100(20):200502, 2008.

[177] H. Nagasawa, K. Yagi, T. Kawahara, N. Hatta, G. Pensl, W. Choyke, T. Yamada, H. Itoh, and A. Schöner. Low-defect 3c-sic grown on undulant-si (001) substrates. In *Silicon Carbide*, pages 207–228. Springer, 2004.

[178] Y. Nakamura, Y. A. Pashkin, and J. Tsai. Coherent control of macroscopic quantum states in a single-cooper-pair box. *Nature*, 398(6730):786–788, 1999.

[179] B. Naydenov, F. Dolde, L. T. Hall, C. Shin, H. Fedder, L. C. Hollenberg, F. Jelezko, and J. Wrachtrup. Dynamical decoupling of a single-electron spin at room temperature. *Physical Review B*, 83(8):081201, 2011.

[180] E. Neu, D. Steinmetz, J. Riedrich-Möller, S. Gsell, M. Fischer, M. Schreck, and C. Becher. Single photon emission from silicon-vacancy colour centres in chemical vapour deposition nano-diamonds on iridium. *New Journal of Physics*, 13(2):025012, 2011.

[181] P. Neumann, J. Beck, M. Steiner, F. Rempp, H. Fedder, P. R. Hemmer, J. Wrachtrup, and F. Jelezko. Single-shot readout of a single nuclear spin. *Science*, 329(5991):542, 2010.

[182] A. D. OConnell, M. Hofheinz, M. Ansmann, R. C. Bialczak, M. Lenander, E. Lucero, M. Neeley, D. Sank, H. Wang, M. Weides, et al. Quantum ground state and single-phonon control of a mechanical resonator. *Nature*, 464(7289):697–703, 2010.

[183] K. Okabe, N. Inada, C. Gota, Y. Harada, T. Funatsu, and S. Uchiyama. Intracellular temperature mapping with a fluorescent polymeric thermometer and fluorescence lifetime imaging microscopy. *Nature communications*, 3:705, 2012.

[184] E. V. Oort and M. Glasbeek. Electric-field-induced modulation of spin echoes of n-v centers in diamond. *Chem. Phys. Lett.*, 168(6):529 – 532, 1990. ISSN 0009-2614. doi: http://dx.doi.org/10.1016/0009-2614(90)85665-Y. URL `http://www.sciencedirect.com/science/article/pii/000926149085665Y`.

[185] W. Paul. Electromagnetic traps for charged and neutral particles. *Rev. Mod. Phys.*, 62:531–540, Jul 1990. doi: 10.1103/RevModPhys.62.531. URL `http://link.aps.org/doi/10.1103/RevModPhys.62.531`.

[186] A. Peres. Separability criterion for density matrices. *Phys. Rev. Lett.*, 77:1413–1415, 1996. doi: 10.1103/PhysRevLett.77.1413. URL `http://link.aps.org/doi/10.1103/PhysRevLett.77.1413`.

[187] W. Pfaff, B. Hensen, H. Bernien, S. B. van Dam, M. S. Blok, T. H. Taminiau, M. J. Tiggelman, R. N., Schouten, M. Markham, D. J. Twitchen, and R. Hanson. Unconditional quantum teleportation between distant solid-state qubits. *Science*, 345:532–535, 2014. doi: 10.1126/science.1253512.

[188] T. B. Pittman, B. C. Jacobs, and J. D. Franson. Probabilistic quantum logic operations using polarizing beam splitters. *Phys. Rev. A*, 64:062311, Nov 2001. doi: 10.1103/PhysRevA.64.062311. URL http://link.aps.org/doi/10.1103/PhysRevA.64.062311.

[189] T. Plakhotnik and D. Gruber. Luminescence of nitrogen-vacancy centers in nanodiamonds at temperatures between 300 and 700 k: perspectives on nanothermometry. *Phys. Chem. Chem. Phys.*, 12(33):9751–9756, 2010.

[190] M. Radulaski, T. M. Babinec, S. Buckley, A. Rundquist, J. Provine, K. Alassaad, G. Ferro, and J. Vučković. Photonic crystal cavities in cubic (3c) polytype silicon carbide films. *Optics express*, 21(26):32623–32629, 2013.

[191] M. Radulaski, T. M. Babinec, K. Muller, K. G. Lagoudakis, J. L. Zhang, S. Buckley, Y. A. Kelaita, K. Alassaad, G. Ferro, and J. Vuckovic. Visible photoluminescence from cubic (3c) silicon carbide microdisks coupled to high quality whispering gallery modes. *ACS Photonics*, 2(1):14–19, 2014.

[192] S. C. Rand. *Lectures on Light: Nonlinear and Quantum Optics using the Density Matrix*. Oxford University Press, USA, 2010.

[193] S. C. Rand. *Lectures on Light: Nonlinear and Quantum Optics using the Density Matrix*. Oxford University Press, USA, 2010.

[194] A. Ranjbar, M. Babamoradi, M. Heidari Saani, M. A. Vesaghi, K. Esfarjani, and Y. Kawazoe. Many-electron states of nitrogen-vacancy centers in diamond and spin density calculations. *Phys. Rev. B*, 84:165212, Oct 2011. doi: 10.1103/PhysRevB.84.165212. URL http://link.aps.org/doi/10.1103/PhysRevB.84.165212.

[195] P. Rebentrost, M. Mohseni, and S. Lloyd. Quantum support vector machine for big data classification. *Phys. Rev. Lett.*, 113: 130503, Sep 2014. doi: 10.1103/PhysRevLett.113.130503. URL http://link.aps.org/doi/10.1103/PhysRevLett.113.130503.

[196] N. Reddy, N. Manson, and E. Krausz. Two-laser spectral hole burning in a colour centre in diamond. *Journal of Luminescence*, 38(1-6):46–47, 1987.

[197] D. A. Redman, S. Brown, R. H. Sands, and S. C. Rand. Spin dynamics and electronic states of nv centers in diamond by epr and four-wave-mixing spectroscopy. *Phys. Rev. Lett.*, 67(24):3420–3423, 1991.

[198] M. Reed, L. DiCarlo, S. Nigg, L. Sun, L. Frunzio, S. Girvin, and R. Schoelkopf. Realization of three-qubit quantum error correction with superconducting circuits. *Nature*, 482(7385):382–385, 2012.

[199] F. Reinhard, F. Shi, N. Zhao, F. Rempp, B. Naydenov, J. Meijer, L. T. Hall, L. Hollenberg, J. Du, R.-B. Liu, et al. Tuning a spin bath through the quantum-classical transition. *Physical review letters*, 108(20):200402, 2012.

[200] Riedel, D. Fuchs, F. Kraus, H. Väth, S. Sperlich, A. Dyakonov, V. Soltamova, A. A. Baranov, P. G. Ilyin, V. A. Astakhov, and G. V. Resonant addressing and manipulation of silicon vacancy qubits in silicon carbide. *Phys. Rev. Lett.*, 109:226402, 2012. doi: 10.1103/PhysRevLett.109.226402. URL `http://link.aps.org/doi/10.1103/PhysRevLett.109.226402`.

[201] C. Rigetti, J. M. Gambetta, S. Poletto, B. L. T. Plourde, J. M. Chow, A. D. Córcoles, J. A. Smolin, S. T. Merkel, J. R. Rozen, G. A. Keefe, M. B. Rothwell, M. B. Ketchen, and M. Steffen. Superconducting qubit in a waveguide cavity with a coherence time approaching 0.1 ms. *Phys. Rev. B*, 86:100506, Sep 2012. doi: 10.1103/PhysRevB.86.100506. URL `http://link.aps.org/doi/10.1103/PhysRevB.86.100506`.

[202] R. L. Rivest, A. Shamir, and L. Adleman. A method for obtaining digital signatures and public-key cryptosystems. *Commun. ACM*, 21(2):120–126, 1978. ISSN 0001-0782. doi: 10.1145/359340.359342. URL `http://doi.acm.org/10.1145/359340.359342`.

[203] L. Robledo, H. Bernien, T. van der Sar, and R. Hanson. Spin dynamics in the optical cycle of single nitrogen-vacancy centres in diamond. *New J. Phys.*, 13:025013, 2011.

[204] L. Robledo, L. Childress, H. Bernien, B. Hensen, P. F. A. Alkemade, and R. Hanson. High-fidelity projective read-out of a solid-state spin quantum register. *Nature*, 477: 574–578, 2011.

[205] L. J. Rogers, S. Armstrong, M. J. Sellars, and N. B. Manson. Infrared emission of the nv centre in diamond: Zeeman and uniaxial stress studies. *New J. Phys.*, 10:103024, 2008.

[206] P. Roushan, C. Neill, Y. Chen, M. Kolodrubetz, C. Quintana, N. Leung, M. Fang, R. Barends, B. Campbell, Z. Chen, et al. Observation of topological transitions in interacting quantum circuits. *Nature*, 515(7526):241–244, 2014.

[207] C. Ryan, J. Hodges, and D. Cory. Robust decoupling techniques to extend quantum coherence in diamond. *Physical Review Letters*, 105(20):200402, 2010.

[208] S. E. Saddow and A. K. Agarwal. *Advances in Silicon Carbide Processing and Applications*. Artech House, 1st edition, 2004. ISBN 000-1580537405.

[209] S. E. Saddow, C. L. Frewin, C. Coletti, N. Schettini, E. Weeber, A. Oliveros, and M. Jarosezski. Single-crystal silicon carbide: A biocompatible and hemocompatible semiconductor for advanced biomedical applications. In *Materials Science Forum*, volume 679, pages 824–830. Trans Tech Publ, 2011.

[210] T. Sato, K. Ohashi, T. Sudoh, K. Haruna, and H. Maeta. Thermal expansion of a high purity synthetic diamond single crystal at low temperatures. *Phys. Rev. B*, 65 (9):092102, 2002.

[211] R. S. Schoenfeld and W. Harneit. Real time magnetic field sensing and imaging using a single spin in diamond. *Phys. Rev. Lett.*, 106(3):30802, 2011.

[212] D. Schuster, A. Houck, J. Schreier, A. Wallraff, J. Gambetta, A. Blais, L. Frunzio, J. Majer, B. Johnson, M. Devoret, et al. Resolving photon number states in a superconducting circuit. *Nature*, 445(7127):515–518, 2007.

[213] C. E. Shannon. A mathematical theory of communication. *Bell System Technical Journal*, 27(3):379–423, 1948.

[214] L. Shi, D. Li, C. Yu, W. Jang, D. Kim, Z. Yao, P. Kim, and A. Majumdar. Measuring thermal and thermoelectric properties of one-dimensional nanostructures using a microfabricated device. *J. Heat Transf.*, 125(5):881–888, 2003. doi: 10.1115/1.1597619.

[215] P. W. Shor. Polynomial-time algorithms for prime factorization and discrete logarithms on a quantum computer. *SIAM J. Comp.*, 26(5):1484–1509, 1997. doi: 10.1137/S0097539795293172.

[216] D. Simon. On the power of quantum computation. In *Proceedings of the 35th Annual Symposium on Foundations of Computer Science*, pages 116–123. IEEE Computer Society, 1994.

[217] C. P. Slichter. *Principles of magnetic resonance*. Springer, New York, 1990.

[218] B. Smeltzer, L. Childress, and A. Gali. ^{13}c hyperfine interactions in the nitrogen-vacancy centre in diamond. *New J. Phys.*, 13:025021, 2011.

[219] M. Soini, I. Zardo, E. Uccelli, S. Funk, G. Koblmüller, A. F. i Morral, and G. Abstreiter. Thermal conductivity of gaas nanowires studied by micro-raman spectroscopy combined with laser heating. *Appl. Phys. Lett.*, 97(26):263107, 2010. doi: 10.1063/1.3532848.

[220] V. A. Soltamov, A. A. Soltamova, P. G. Baranov, and I. I. Proskuryakov. Room temperature coherent spin alignment of silicon vacancies in 4h- and 6h-sic. *Phys. Rev. Lett.*, 108:226402, 2012. doi: 10.1103/PhysRevLett.108.226402. URL `http://link.aps.org/doi/10.1103/PhysRevLett.108.226402`.

[221] N. Son, E. Sörman, W. Chen, M. Singh, C. Hallin, O. Kordina, B. Monemar, E. Janzén, and J. Lindström. Dominant recombination center in electron-irradiated 3c-sic. *Journal of applied physics*, 79(7):3784–3786, 1996.

[222] N. Son, E. Sörman, W. Chen, C. Hallin, O. Kordina, B. Monemar, and E. Janzén. Optically detected magnetic resonance studies of defects in 3c-sic epitaxial layers. *Diam. Relat. Mater.*, 6(10):1381 – 1384, 1997. ISSN 0925-9635. Proceeding of the 1st European Conference on Silicon Carbide and Related Materials (ECSCRM 1996).

[223] N. T. Son, P. N. Hai, M. Wagner, W. M. Chen, A. Ellison, C. Hallin, B. Monemar, and E. Janzén. Optically detected magnetic resonance studies of intrinsic defects in 6h-sic. *Semic. Sci. Tech.*, 14(12):1141, 1999. URL `http://stacks.iop.org/0268-1242/14/i=12/a=323`.

[224] N. T. Son, P. Carlsson, J. ul Hassan, E. Janzén, T. Umeda, J. Isoya, A. Gali, M. Bockstedte, N. Morishita, T. Ohshima, and H. Itoh. Divacancy in 4h-sic. *Phys. Rev. Lett.*, 96:055501, 2006. doi: 10.1103/PhysRevLett.96.055501. URL `http://link.aps.org/doi/10.1103/PhysRevLett.96.055501`.

[225] N. T. Son, T. Umeda, J. Isoya, A. Gali, M. Bockstedte, B. Magnusson, A. Ellison, N. Morishita, T. Ohshima, H. Itoh, et al. Divacancy model for p6/p7 centers in 4h- and 6h-sic. In *Materials science forum*, volume 527, pages 527–530. Trans Tech Publ, 2006.

[226] B.-S. Song, S. Yamada, T. Asano, and S. Noda. Demonstration of two-dimensional photonic crystals based on silicon carbide. *Optics express*, 19(12):11084–11089, 2011.

[227] P. L. Stanwix, L. M. Pham, J. R. Maze, D. Le Sage, T. K. Yeung, P. Cappellaro, P. R. Hemmer, A. Yacoby, M. D. Lukin, and R. L. Walsworth. Coherence of nitrogen-vacancy electronic spin ensembles in diamond. *Physical Review B*, 82(20):201201, 2010.

[228] T. Staudacher, F. Shi, S. Pezzagna, J. Meijer, J. Du, C. A. Meriles, F. Reinhard, and J. Wrachtrup. Nuclear magnetic resonance spectroscopy on a (5-nanometer)3 sample volume. *Science*, 339(6119):561–563, 2013. doi: 10.1126/science.1231675.

[229] D. Stucki, N. Gisin, O. Guinnard, G. Ribordy, and H. Zbinden. Quantum key distribution over 67 km with a plug&play system. *New Journal of Physics*, 4(1):41, 2002.

[230] K. Szász, T. Hornos, M. Marsman, and A. Gali. Hyperfine coupling of point defects in semiconductors by hybrid density functional calculations: The role of core spin polarization. *Phys. Rev. B*, 88:075202, Aug 2013. doi: 10.1103/PhysRevB.88.075202. URL `http://link.aps.org/doi/10.1103/PhysRevB.88.075202`.

[231] S. Takahashi, R. Hanson, J. van Tol, M. S. Sherwin, and D. D. Awschalom. Quenching spin decoherence in diamond through spin bath polarization. *Phys. Rev. Lett.*, 101: 047601, 2008.

[232] P. Tamarat, T. Gaebel, J. R. Rabeau, M. Khan, A. D. Greentree, H. Wilson, L. C. L. Hollenberg, S. Prawer, P. Hemmer, F. Jelezko, and J. Wrachtrup. Stark shift control of single optical centers in diamond. *Phys. Rev. Lett.*, 97:083002, Aug 2006. doi: 10.1103/PhysRevLett.97.083002. URL `http://link.aps.org/doi/10.1103/PhysRevLett.97.083002`.

[233] P. Tamarat, N. Manson, J. Harrison, R. McMurtrie, A. Nizovtsev, C. Santori, R. Beausoleil, P. Neumann, T. Gaebel, F. Jelezko, et al. Spin-flip and spin-conserving optical transitions of the nitrogen-vacancy centre in diamond. *New Journal of Physics*, 10(4): 045004, 2008.

[234] J. Taylor, P. Cappellaro, L. Childress, L. Jiang, D. Budker, P. Hemmer, A. Yacoby, W. Walsworth, , and M. Lukin. High-sensitivity diamond magnetometer with nanoscale resolution. *Nat. Phys.*, 4:810–816, 2008. doi: 10.1038/nphys1075.

[235] E. Togan, Y. Chu, A. S. Trifonov, L. Jiang, J. Maze, L. Childress, M. V. G. Dutt, A. S. Sorensen, P. R. Hemmer, A. S. Zibrov, and M. D. Lukin. Quantum entanglement between an optical photon and a solid-state spin qubit. *Nature*, 466(7307):730–734, 2010. ISSN 0028-0836. doi: 10.1038/nature09256. URL `http://dx.doi.org/10.1038/nature09256`.

[236] D. M. Toyli, D. J. Christle, A. Alkauskas, B. B. Buckley, C. G. Van de Walle, and D. D. Awschalom. Measurement and control of single nitrogen-vacancy center spins above 600 k. *Phys. Rev. X*, 2:031001, 2012. doi: 10.1103/PhysRevX.2.031001. URL `http://link.aps.org/doi/10.1103/PhysRevX.2.031001`.

[237] D. M. Toyli, C. F. de las Casas, D. J. Christle, V. V. Dobrovitski, and D. D. Awschalom. Fluorescence thermometry enhanced by the quantum coherence of single spins in diamond. *Proc. Nat. Acad. Sci.*, 110(21):8417–8421, 2013. doi: 10.1073/pnas.1306825110.

[238] V. Vainer and V. Ilin. Electron spin resonance of exchange-coupled vacancy pairs in hexagonal silicon carbide. *Sov. Phys. Solid State*, 23:2126–2133, 1981.

[239] C. H. Van der Wal, A. Ter Haar, F. Wilhelm, R. Schouten, C. Harmans, T. Orlando, S. Lloyd, and J. Mooij. Quantum superposition of macroscopic persistent-current states. *Science*, 290(5492):773–777, 2000.

[240] E. Van Oort and M. Glasbeek. Optically detected low field electron spin echo envelope modulations of fluorescent nv centers in diamond. *Chemical Physics*, 143(1):131–140, 1990.

[241] E. Van Oort, N. Manson, and M. Glasbeek. Optically detected spin coherence of the diamond nv centre in its triplet ground state. *Journal of Physics C: Solid State Physics*, 21(23):4385, 1988.

[242] J. van Tol, G. Morley, S. Takahashi, D. McCamey, C. Boehme, and M. Zvanut. High-field phenomena of qubits. *Applied magnetic resonance*, 36(2-4):259–268, 2009.

[243] F. Vetrone, R. Naccache, A. Zamarron, A. Juarranz de la Fuente, F. Sanz-Rodriguez, L. Martinez Maestro, E. Martin Rodriguez, D. Jaque, J. Garcia Sole, and J. A. Capobianco. Temperature sensing using fluorescent nanothermometers. *ACS nano*, 4(6): 3254–3258, 2010.

[244] J. A. Vrugt, E. Laloy, C. J. F. ter Braak, and J. M. Hyman. Posterior exploration using differential evolution adaptive metropolis with sampling from past states. *to be submitted to SIAM Optimization*, 2011.

[245] G. W. Walker, V. C. Sundar, C. M. Rudzinski, A. W. Wun, M. G. Bawendi, and D. G. Nocera. Quantum-dot optical temperature probes. *Applied Physics Letters*, 83(17): 3555–3557, 2003.

[246] A. Wallraff, D. I. Schuster, A. Blais, L. Frunzio, R.-S. Huang, J. Majer, S. Kumar, S. M. Girvin, and R. J. Schoelkopf. Strong coupling of a single photon to a superconducting qubit using circuit quantum electrodynamics. *Nature*, 431(7005):162–167, 2004.

[247] J. R. Weber, W. F. Koehl, J. B. Varley, A. Janotti, B. B. Buckley, C. G. Van de Walle, and D. D. Awschalom. Quantum computing with defects. *P. Natl. Acad. Sci. USA*, 107(19):8513, 2010.

[248] M. Widmann, S. Lee, T. Rendler, N. Son, H. Fedder, S. Paik, L. Yang, N. Zhao, S. Yang, I. Booker, A. Denisenko, M. Jamali, S. Momenzadeh, I. Gerhardt, T. Ohshima, A. Gali, E. Janzén, and J. Wrachtrup. Coherent control of single spins in silicon carbide at room temperature. *Nat. Mater.*, 14:164–168, 2015. doi: 10.1038/nmat4145.

[249] D. J. Wineland, J. J. Bollinger, W. M. Itano, F. L. Moore, and D. J. Heinzen. Spin squeezing and reduced quantum noise in spectroscopy. *Phys. Rev. A*, 46(11):6797–6800, 1992.

[250] W. M. Witzel, M. S. Carroll, Ł. Cywiński, and S. D. Sarma. Quantum decoherence of the central spin in a sparse system of dipolar coupled spins. *Physical Review B*, 86(3): 035452, 2012.

[251] J. Wrachtrup, C. Von Borczyskowski, J. Bernard, M. Orritt, and R. Brown. Optical detection of magnetic resonance in a single molecule. *Nature*, 1993.

[252] J. M. Yang, H. Yang, and L. Lin. Quantum dot nano thermometers reveal heterogeneous local thermogenesis in living cells. *ACS Nano*, 5(6):5067–5071, 2011. doi: 10.1021/nn201142f.

[253] S. Yang, Y. Wang, D. B. Rao, T. H. Tran, A. S. Momenzadeh, M. Markham, D. Twitchen, P. Wang, W. Yang, R. Stöhr, et al. High-fidelity transfer and storage of photon states in a single nuclear spin. *Nature Photonics*, 2016.

[254] Y. Yang, K. Ekinci, X. Huang, L. Schiavone, M. Roukes, C. Zorman, and M. Mehregany. Monocrystalline silicon carbide nanoelectromechanical systems. *Applied Physics Letters*, 78(2):162–164, 2001.